Magnetism in delta Scuti stars

Keegan Thomson-Paressant

PSL UNIVERSITÉ PARIS

THÈSE DE DOCTORAT

DE L'UNIVERSITÉ PSL

Préparée à l'Observatoire de Paris, Meudon

Magnetism in δ Scuti stars

Soutenue par/Defended by

Keegan Thomson-Paressant

Le 10 Septembre 2024

ED n°127

Astronomie et Astrophysique d'Ile de France

Spécialité/Specialisation

Astrophysique

Préparée au/Prepared at

Observatoire de Paris, Meudon

Composition du jury/Jury composition :

Prof. Christophe LE PONCIN-LAFITTE SYRTE, Observatoire de Paris	*Président du jury*
Dr. Claire MOUTOU IRAP, Toulouse	*Rapporteure*
Prof. Georges MEYNET Université de Genève	*Rapporteur*
Dr. Victoria ANTOCI Danmarks Tekniske Universitet, Copenhagen	*Examinatrice*
Dr. Dominic BOWMAN Newcastle University	*Examinateur*
Dr. Coralie NEINER LESIA, Observatoire de Paris	*Directrice de thèse*

l'Observatoire de Paris | PSL

Acknowledgements

Everyone that knows me, or has come to know me over the course of my PhD, are all well aware that the road that has led me to this significant achievement hasn't exactly been the smoothest. Nevertheless, I have certainly learned a lot over this period, both academically and about myself, and I wouldn't be where I am today without the support of a number of groups of people.

Without a doubt, the first person to whom I owe thanks is Coralie Neiner, who has continuously gone above and beyond the call of duty of a mere supervisor. Without her support and guidance, I can safely say I wouldn't be where I am today. Between proofreading my publications and thesis, supervising the multiple telescope proposals I submitted per semester (which would always take longer than planned), assisting me with my (likely too many) postdoc applications, or just being available for a chat at almost any time, she's the best supervisor I could have ever asked for. Most importantly she supported me at a time when others wouldn't, and for that I owe her a lot. Working with her has been an absolute pleasure, and I really hope to be able to continue collaborating with her in the future.

By extension, I have come to really value and respect the numerous members of the Pôle étoile team in Meudon. Having lunch together as a group day-to-day really helped to get to know everyone on a more personal level, from the greenest intern to the most grizzled of researchers, and to form an ensemble. Not to mention the semi-regular aperitifs that would be organised, which were always a success. Additionally, while I elected to revitalise the Journal Club, I was very pleased to see how supportive and "on-board" the team was of the idea, and am glad to see its success continue following my departure from the team. They are truly a great group of individuals, one that I will surely miss as I move to the next stages of my career.

Another group of individuals that absolutely deserve a mention are the wonderful guys and gals that I met during my time at ESO Garching. Despite (or perhaps rather in light of) coming out of a global pandemic, I could not have met a more welcoming and incredible group of people. Regular hikes to the nearby mountains and lakes, playing volleyball (both beach and the ESO team), classic Steiningerweg parties, Beer Friday celebrations, and of course Oktoberfest every year with everyone dressed in their finest Lederhosen and Dirndl ; truly a year of unforgettable memories. While the list of individuals that deserve recognition and thanks would fill two whole pages, I need to give special thanks to three specific groups. First, the Nuremberg Gang (Anita, Elena, Jules, Simon, Stephen, and Tuts), always available for a laugh or a cry, thanks for being amazing people. Second, the members of the ESO Student Reps (Alice, Gemma, Josh, and Samuel), we couldn't have picked a better group of people to look after the best interests of the students at ESO, you're all incredible. Finally, to Samuel in particular, thanks for being the best

officemate one could ever ask for and a truly unbelievable friend. My time at ESO wouldn't have been the same without you, and you have in me a friend for life. While I had to eventually leave ESO, many have also recently completed their own PhD's, and are now spread far and wide. As a result, I know that wherever I travel in the world, at least one of them isn't far away. I look forward to following their careers long into the future, as I'm sure they are doing mine. Until we meet again (very soon) !

On a more personal note, few individuals deserve more recognition than my family, without whose unwavering support I couldn't ever dream of getting to where I am today. I know that my academic career has been anything but smooth sailing, but I never gave up on my dream, and am so proud to be standing where I am today. While I'm sure it wasn't easy for you to have to watch from a distance, and experience second-hand both my successes and failures, I hope I did you proud too. Hopefully the hardest is behind me, and things can only go up from here.

Last but absolutely not least, Sara, the love of my life. While I think the last stages of my PhD were more straightforward and less stressful than when you went through it, I don't think that's true for my PhD as a whole. It was especially difficult going from the comfort of living together for several years, to chasing each other around Europe in the following ones as we each pursued our respective careers. Regardless, you have stuck with me, through thick and thin, and there's nobody I'd rather have by my side. The promise I gave you remains true : it doesn't matter where you are, or where I am, my heart is yours.

And to everyone else in my life that has supported me and stuck with me over the years, which are far too many to include in these paltry few pages, I want to say thank you ! I am truly humbled by the number of people I can consider good friends and colleagues, and the support you provide me with cannot be understated.

Résumé

Les variables δ Scuti (δ Sct) sont des étoiles présentant des variations de luminosité entre les modes de pression d'ordre radial faible et les modes mixtes, et ces pulsations durent généralement de quelques minutes à plusieurs heures. Ces étoiles couvrent la gamme spectrale A à F et sont des étoiles de masse intermédiaire, affichant des masses comprises entre 1,5 et 2,5 $M_{\odot}$. En conséquence, elles se situent dans un régime où la structure interne peut varier considérablement entre les étoiles, et par conséquent leur champ magnétique aussi, si elles en ont un. Les étoiles de petite masse (type FGK) ont des champs magnétiques dynamo produits dans leur enveloppe convective et souvent de structure complexe, tandis que les étoiles de grande masse (de type OBA) ont des champs fossiles et stables, issus du nuage moléculaire à partir duquel l'étoile s'est formée, et typiquement dipolaire.

Jusqu'à présent, l'analyse générale du magnétisme des étoiles suggère qu'environ 10% des étoiles de grande masse affichent des champs magnétiques fossiles et cette fréquence augmente pour les champs dynamos des étoiles de plus petites masses. Cependant, à ce jour, seules 3 étoiles δ Sct présentant des signatures de champ magnétique ont été découvertes : HD 188774, HD 67523, et β Cas. De plus, il existe des preuves suggérant que les modes de pulsation à l'intérieur de l'étoile interagissent avec le champ magnétique, ce dernier supprimant et déformant les pulsations.

Au cours de cette thèse, j'ai développé ce domaine dans 2 directions clés. Tout d'abord, j'ai effectué des travaux statistiques sur des candidats magnétiques δ Sct sélectionnés comme cibles idéales à partir d'un sondage plus large d'étoiles Kepler et TESS, affichant des indices spécifiques suggérant l'existence d'un champ magnétique. Ceci m'a permis d'obtenir une meilleure image de la prévalence, de la structure et de l'origine des champs magnétiques pour ce type d'étoiles. Deuxièmement, j'ai effectué une analyse plus approfondie sur quelques étoiles magnétiques δ Sct confirmées, notamment HD 41641. Cette analyse comprend des observations spectropolarimétriques réparties sur toute la rotation de l'étoile, afin de visualiser la structure du champ magnétique à la surface de l'étoile, ainsi que l'analyse des modes de pulsations en anticipation d'études astérosismiques, qui apporteront des nouvelles perspectives sur la structure interne de l'étoile.

Suite à ces travaux, je fournis la liste de 13 étoiles magnétiques δ Sct confirmées à ce jour, multipliant ainsi par 4 l'échantillon connu de ces étoiles et je propose des premiers éléments statistiques de cet échantillon.

Mots clés : Spectropolarimétrie, Etoiles delta Scuti, Champs magnétiques, Observations

Abstract

δ Scuti (δ Sct) variables are stars exhibiting variations in their luminosity from low radial order pressure modes and mixed modes, and these pulsations typically last anywhere from a few minutes to several hours. These stars span the spectral range A through to F and are typically intermediate mass stars, displaying masses between 1.5-2.5 $M_\odot$. Due to the latter, they fall in a regime where the internal structure can vary significantly between stars, and as a result so too can their magnetic field, should they have one. Typically, small mass stars (FGK) have dynamo magnetic fields produced in their convective envelope and often complex in structure, whereas large mass stars (OBA) have fossil fields, i.e. remnants from the molecular cloud from which the star formed, and typically dipolar.

So far, general analysis in the magnetism of hot (OBA) stars suggests that about 10% of intermediate mass (non-variable) stars display magnetic fields, and the field occurrence increases for dynamo fields in lower mass stars. However, at the start of this thesis work, only 3 δ Sct stars had been found to exhibit magnetic field signatures: HD 188774, HD 67523, and β Cas. Additionally, there is evidence to suggest that the pulsation modes within the star interact with the magnetic field, with the latter suppressing and potentially warping the former.

Over the course of this PhD, I expanded on this domain in two key areas. First, I performed a statistical study of magnetic δ Sct candidates, selected as ideal targets from wider surveys of Kepler and TESS targets, displaying specific features that hint at the existence of a magnetic field. This allows us to get a better picture of the occurrence, structure and origin of magnetic fields for this type of star. Second, I performed more in-depth analysis on a couple of established magnetic δ Sct stars, in particular HD 41641. This analysis includes spectropolarimetric observations spread over the full rotation of the star, in order to map the magnetic field structure at the surface, and pulsational analysis to prepare for future asteroseismic modelling, which will provide insight into the internal structure of the star.

Thanks to this work, I can list 13 magnetic δ Sct stars confirmed to date, which increases the sample of such stars by a factor 4, and I suggest first statistical properties of this sample.

Keywords : Spectropolarimetry, delta Scuti stars, Magnetic fields, Observations

Table of Contents

Figures List

Tables List

Acronyms

CoRoT *Convection, Rotation and planetary Transits satellite*
PLATO *PLAnetary Transits and Oscillations of stars*
TESS *Transiting Exoplanet Survey Satellite*
DRS *Data Reduction Software*
ESPaDOnS *Echelle SpectroPolarimetric Device for the Observation of Stars*
FAP *False Alarm Probability*
FFI *Full Frame Image*
LAMOST *Large Sky Area Multi-Object Fibre Spectroscopic Telescope*
LSD *Least Squares Deconvolution*
MAST *Mikulski Archive for Space Telescopes*
SNR *Signal-to-Noise Ratio*
SpeNT *SPEctral Normalization Tool*
TAMS *Terminal Age Main Sequence*
VALD *Vienna Atomic Line Database*
ZAMS *Zero Age Main Sequence*
ZDI *Zeeman Doppler Imaging*

Chapter 1

Introduction

1 Stellar internal physics and evolution

Stars play an essential role in the cosmic engine. Their hearts forge the building blocks from which new stars, planets and even life itself was formed. The physical processes occurring within stars also have significant impacts on the structure, evolution and dynamics of the universe. Stellar winds push around clouds of gas and dust, and can ionise the material therein, while the cataclysmic supernova explosions that occur at the end of the lifetime of some stars can equally quench or drive the formation of new stars in their cosmic neighbourhood.

Generally, astronomers consider three regimes of stellar evolution : the low-mass ($M \lesssim 2\ M_{\odot}$), intermediate-mass ($2 \lesssim M \lesssim 8\ M_{\odot}$), and high-mass stars ($M \gtrsim 8\ M_{\odot}$). This distinction implies not only the initial mass of the star, but also refers to its internal structure and which evolutionary stages it passes through over the course of its lifetime. For example, low-mass stars present convective envelopes and radiative cores, and since their mass is insufficient to burn elements heavier than helium in their cores, they will inevitably end their lives as white dwarfs - low luminosity objects that will continue to emit light for tens or even hundreds of billions of years, until the last of their fuel is eventually consumed. In comparison, high-mass stars can fuse heavier elements up to iron in their cores, resulting in an ever-increasing density until eventually the star's own gravity becomes too strong to be resisted by radiation pressure, and it collapses in on itself. This results in a blinding supernova explosion, spreading its enriched contents into the surrounding space, and leaving behind a super-dense core remnant, such as a black hole or neutron star.

Depending on the mass and evolutionary stage of a given star, the methods of characterisation and physical processes occurring within the star that need to be taken into account can vary significantly. In order to visualise the diversity of stars and how they relate to one-another, astronomers often refer to the Hertzsprung-Russell (H-R) diagram (see Fig. 1.1). The H-R diagram is a representation of the various families of stars, where the relationship between a star's luminosity (or magnitude) and its effective temperature (or spectral class) provides insight into a number of its other stellar parameters. Based on a star's position in the diagram, astronomers

can infer information such as its evolutionary stage and mass. This is a powerful tool, because a larger number of stellar parameters can be approximated as a result of only a couple of known ones.

Guided and calibrated by observations such as high-resolution spectroscopy, asteroseismology, astrometry, interferometry, etc., theoretical models continuously help us improve and fine-tune the relationships between these stellar parameters. There remains, however, a number of physical processes that are yet to be well constrained which limit the true accuracy of these models. Indeed, two of such mechanisms are pulsations and magnetic fields, both of which have important impacts on how stars are structured and evolve over the course of their lifetimes. To better constrain how these aspects come into play, we require high-precision observational datasets that allow for the identification and characterisation of these mechanisms across a wide variety of stars and parameter combinations.

Over the coming sections, I will describe the current state-of-the-art in the field of magnetism in variable stars, combining both of these aspects together into a single focus. This will include context on why variable stars in particular can provide valuable contributions in the study of stellar magnetism, as well as descriptions on the techniques utilised for studying these objects and extracting the desired information.

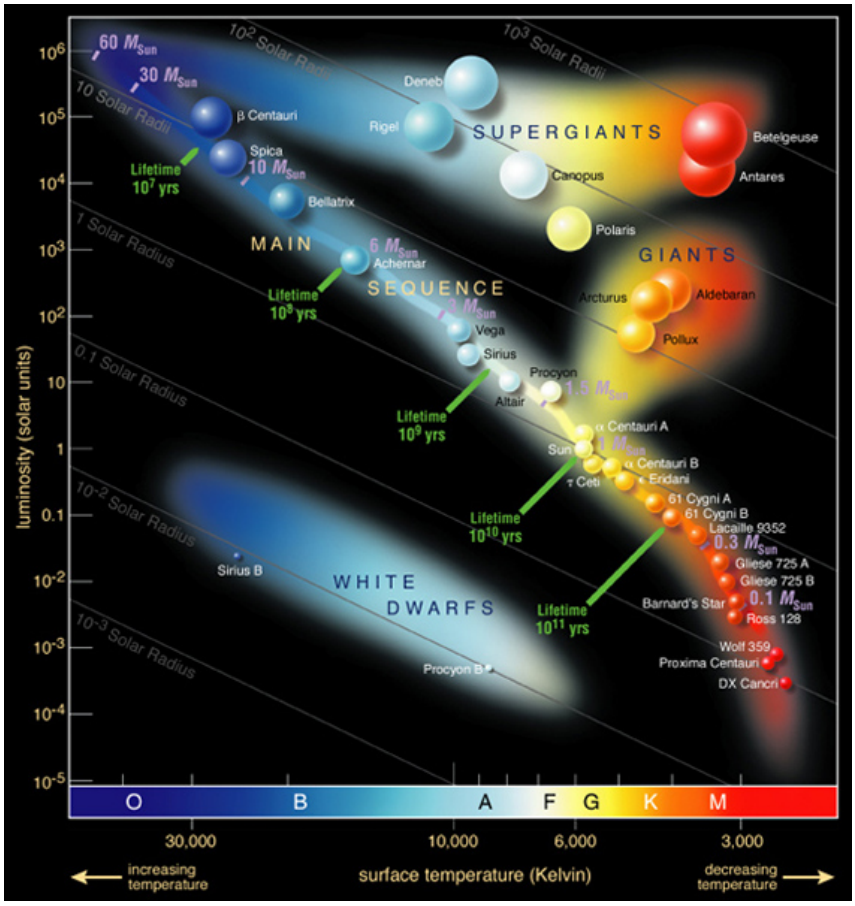

FIGURE 1.1 – Example of a Hertzsprung-Russell diagram. Image credit : European Southern Observatory [1].

2 Studying stellar pulsations and magnetism in hot stars

2.1 Stellar pulsation modes

Within stellar populations, of particular note are a number of families of pulsating variable stars, whose brightness varies over time. This variability is intrinsic, that is to say that it originates from physical processes occurring inside the star, and not due to extrinsic factors such as eclipses from a companion. Depending on where in the star it occurs and what mechanisms are at play, these instabilities express themselves in different ways. There are two main processes at the origin of these instabilities, each of which drives a different type of observable mode. First are pressure modes (p-modes), typically generated as a result of changes in opacity such as the κ-mechanism, and, as the mode name suggests, equilibrium is restored by the force of pressure pushing outwards. Second are gravity modes (g-modes), which form at the boundary between layers, such as the one between the convective core and radiative envelope in high-mass stars, and where in this case the restoring force of the pulsation is gravity/buoyancy. Mixed modes do exist, where for some frequency ranges the mode acts both as a p-mode near the surface and as a g-mode deeper within the star [1]. These pulsation modes can be radial, where the whole star expands and contracts as a whole, or non-radial modes, where one region of the star can expand while another shrinks.

Generally these pulsation modes occur at regular, periodic patterns, making them easily recoverable through photometric observations either from space or from the ground, though the frequency ranges where we observe these modes depend on the mechanism and the type of pulsator. For example, in the cooler regime ($6000 < T_{\rm eff} \lesssim 10,000$ K) we observe the δ Scuti and the γ Doradus stars, which pulsate in high-frequency p-modes ($\gtrsim 5$ d^{-1}) and low-frequency g-modes ($\lesssim 5$ d^{-1}) respectively. In the hotter regime ($T_{\rm eff} \gtrsim 10,000$ K), we identify the β Cephei and Slowly Pulsating B-type (SPB) stars, which present a similar pulsational dichotomy to their cooler counterparts. Some authors claim the existence of an additional class of pulsator, named Maia variables, that present similar high-frequency variability to δ Sct and β Cep stars but fall between the typical temperature ranges of these two [2, 3], though this remains a point of contention amongst astronomers.

By studying these pulsating variable stars, astronomers have identified regions of the H-R diagram where specific combinations of temperature and luminosity lead to instabilities within the star and result in the pulsation modes we observe for these stars. There is some disagreement in the definitions of these 'instability strips' when comparing the predictions from models with observations, which proves that there are mechanisms involved that we are yet to fully understand, and therefore there is still work to do to uncover the underlying physics at play.

A recent publication by Balona [4] debates the classification of these pulsating stars, suggesting that the characteristics commonly utilised to distinguish between one type of pulsator and another (e.g. effective temperature and frequency patterns) are too arbitrary, and that perhaps the same fundamental mechanism is responsible for the existence of all these pulsators. This is justified by a number of factors, a few of which I will detail here.

1. https://www.eso.org

Some broad photometric surveys suggest that at least 25% of δ Scuti (δ Sct) stars are hybrids [e.g. 5, 6], presenting γ Doradus (γ Dor) low frequency signatures on top of their typical frequency pattern, and a similar number of β Cephei (β Cep) have also been similarly categorised, showing SPB-type pulsation frequencies in their lightcurves. In many cases, these lower frequency signals have only been detected recently, by virtue of the advent of space telescope photometry (e.g. *Kepler* and the *Transiting Exoplanet Survey Satellite* (*TESS*)), and had otherwise passed undetected by ground-based instruments. This could suggest that rather than four distinct pulsator types, there would be a cool pulsator regime (δ Sct–γ Dor) and hot pulsator regime (β Cep–SPB), with Maia variables being merely poorly defined δ Sct. This latter argument is also reflected in other studies [7], where misclassification has been shown to be common, and that these stars belong to the instability strips of other well-known pulsators. This is more or less put in evidence in the left plot of Fig. 1.2, where we observe an overlap in the temperature ranges of these two 'pairs' of pulsators, and a somewhat smooth transition from one to the other. Similarly, as seen in the right-hand plot of the same figure, stellar models are unable to reproduce the populations of Maia variables that are seen from observations, suggesting a disagreement between observation and theory.

A degree of scepticism should be maintained when considering the results from the Balona [4] study however, as there are a number of assumptions made therein that should be verified before being taken as gospel. For example, the stellar parameters (e.g. luminosity, effective temperature, etc.) for the 125,000 stars in the sample were determined via *Kepler* and *TESS* datasets, neither of which are known to be particularly reliable in this regard. The results should not necessarily be disregarded outright, however, as it comprises nonetheless a rather significant sample size and it is not necessarily evident to analyse the data of such a large number of stars. That said, until a more reliable analysis of a sufficiently large dataset can be performed and used as comparison, it is difficult to conclude much from this study.

One additional degree of complexity is the fact the region of the H-R diagram that is occupied by δ Sct and γ Dor stars is also shared by a large population of non-pulsating stars, which suggests that the specific combination of effective temperature and luminosity does not necessarily imply the presence of pulsations. This is further accentuated by the fact that δ Sct stars with very similar stellar parameters can present widely different frequency patterns.

What is clear, however, is that our understanding of stellar internal processes is not yet sufficient to precisely determine the areas of the H-R diagram in which these instability regions appear, and identify what other factors come into play to determine why pulsations are observed in one star and not in its apparent twin. More work is required, and this starts by the construction and development of a database of well-studied (ideally magnetic) pulsators which span the parameter space, and give us a perspective into the bigger picture that is the role of pulsations and magnetism in the formation and evolution of stars.

2.2 Magnetism

Over the last couple of decades, great progress has been made in the detection and characterisation of magnetic fields in hot stars, particularly those with radiative envelopes. Spectropola-

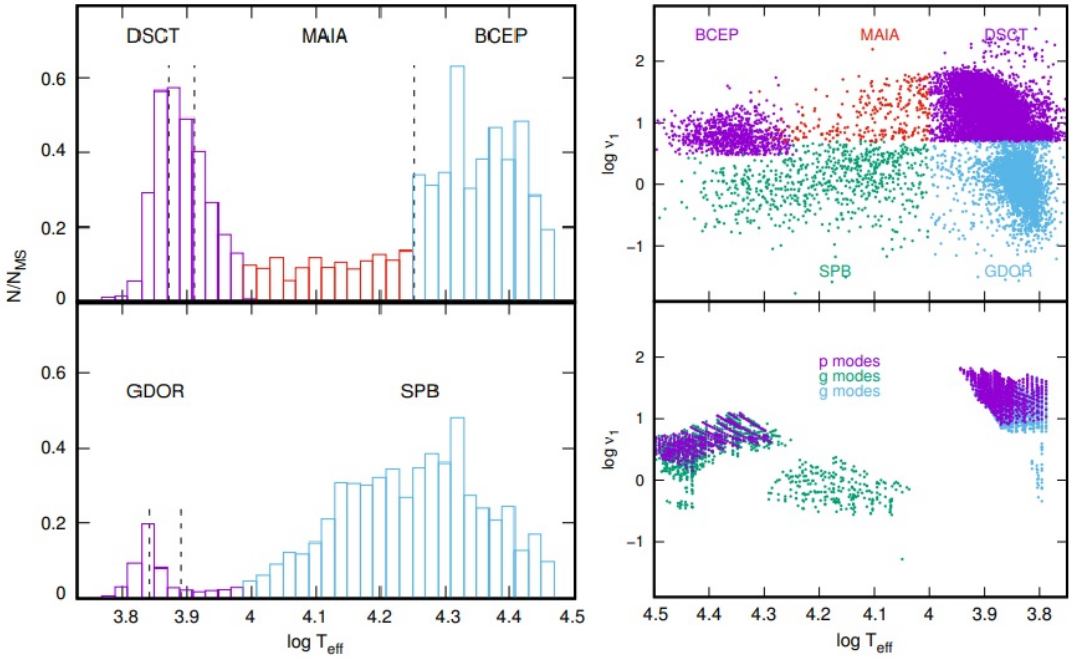

FIGURE 1.2 – **Left :** Ratio N/N_{MS} of pulsator type with respect to number of main sequence stars within a particular effective temperature bin. Dashed lines correspond to the minimum and maximum of the hot temperature edge of δ Sct and γ Dor stars predicted by models, as well as the cool edge of the β Cep instability region. **Right :** Largest amplitude frequency with respect to effective temperature from *TESS* pulsating stars, compared with frequencies of unstable modes with $l \leq 2$ in non-rotating models. Images taken from BALONA [4].

rimetric surveys have established a ∼10% incidence rate of magnetic fields amongst these stars (e.g. MiMeS [8], BOB [9], LIFE [10]), with strengths typically of the order of 300 G to 30 kG [11]. These magnetic hot stars are typically main sequence objects, with only a few intermediate-mass pre-main sequence stars and post-main sequence candidates. Typically, these more evolved stars present significantly weaker surface fields than their main sequence brethren, which is to be expected because of conservation of magnetic flux. As a star evolves along the red giant branch, its envelope cools and expands, and as such the magnetic field we can observe at the surface is significantly reduced, while the core magnetic field remains mostly the same [12-14]. In comparison with cooler stars, these hot stars present magnetic fields that are globally strong, organised, and stable over human timescales.

Thanks to these efforts, we are beginning to achieve an understanding as to the origin of magnetism and how it affects stellar evolution. There is strong evidence to suggest that in many cases a star's magnetic field is a fossil remnant, dating back to when the star was formed or resulting from its early evolution [15]. These fields have impacts on a variety of stellar mechanisms including mass-loss rates [16], angular momentum transport and loss [17], chemical mixing, and even the chemical evolution of the local neighbourhood through external processes such as supernova feedback [18].

Previous studies have established a so-called 'magnetic desert', where magnetic hot stars with field strengths lower than ∼300 G appear to be extremely rare [9, 19, 20]. However, some

stars on the cooler edge of this grouping (typically A- and F-types) have been shown to present ultra-weak fields, with polar field strengths of the order of 1 G [21-23], as well as fields originating from dynamo mechanisms, which are less stable and less structured compared to their fossil field counterparts. Indeed, ultra-weak fields have been detected in many A-type stars that did not present strong fields in initial polarimetric observations. It is possible that such ultra-weak fields could exist in hotter stars as well, provided we can achieve sufficiently high-quality spectropolarimetric datasets. This could suggest that these ultra-weak fields may be ubiquitous in stars that do not present a strong field, and reveals the possible existence of multiple regimes of magnetism in hot stars, the origins and implications of which are as of yet unknown.

In addition to magnetic fields detected at the stellar surface by spectropolarimetry, magnetic fields that are more confined to internal regions can be generated by a dynamo in the convective core in some stars, with strengths that range from 100 kG up to 1 MG [24]. The timescale for such core-dynamo fields to reach the surface is longer than the lifetime of the star, therefore they cannot be observed with spectropolarimetry. However, these strong core fields can be enhanced when combined with a strong large-scale fossil field in the radiative envelope, but this depends on the relative rotation rates of both the core and the surface [25]. It is therefore clear that magnetic fields have an impact on different layers of hot stars, both near the surface and deep in their interiors. They are also efficient mechanisms for angular momentum transport [e.g. 26, 27] and convective-boundary mixing suppression [28], which are directly related to how long a star remains on the main-sequence [29, 30]. In the case of hot, magnetic, chemically peculiar (CP) stars, we typically observe slower rotation rates than in their non-magnetic counterparts, though some fast rotating hot magnetic CP stars are known to exist (e.g. HR 7355 [31], HR 5907 [32]). While this feature does not necessarily apply to all hot stars, coupling the impacts of magnetism on stellar winds and on angular momentum transport results in what appears to be an effective braking mechanism. In current evolutionary models, stellar magnetism and its impacts on the evolution of stars are not well constrained, and as a result the accuracy of such models is significantly hampered [29, 33].

Conclusively, by increasing our sample size of well-studied magnetic hot stars we can increase the accuracy and performance of stellar evolution and stellar internal structure models, and in turn, achieve a greater understanding of stellar physics across the H-R diagram.

2.3 δ Scuti stars

δ Scuti variables are stars exhibiting variations in their luminosity from low radial order p-modes and mixed modes, which are themselves driven by a combination of the κ-mechanism operating within the He II ionisation zone [34] coupled with turbulent pressure in the hydrogen ionisation layer [35, 36]. These pulsations typically have periods that fall in the range between 15 min up to 8 h. δ Sct stars span the spectral range A through F, with masses generally of the order of 1.5-2.5 $M_\odot$ [37] and effective temperatures typically between ∼6700 and 8000 K.

Studies have shown that, in many cases, δ Sct stars can present long-term variability of their pulsation amplitudes and frequencies [38, 39], and some also show pulsations at high frequencies ($\nu > 40$ d^{-1}) that are similar to those found in roAp stars [40], which typically present strong

well-structured magnetic fields. If such high radial-order magneto-acoustic modes are also excited in stars presenting δ Sct pulsations (i.e. roAp-δ Sct hybrids), we might expect them to possess an equally significant large-scale magnetic field.

Prior to the start of my thesis work, only a handful of δ Sct variables had been found to exhibit magnetic fields : HD 188774 [41], ρ Pup [42], and β Cas [43, 44], all of which have been discovered in the last decade. Several others have been proposed (e.g. HD 21190 [45, 46] and HD 35929 [47]) but due to limited data or conflicting results they are yet to be confirmed.

It is with this in mind that over the course of my studies I have sought to expand on this limited sample size, by identifying and characterising the magnetic fields of new magnetic δ Sct stars. As a result, I seek to achieve a greater understanding of the origin and nature of magnetism in this family of stars (and perhaps by correlation others as well), as well as the interplay between magnetism and oscillation modes in pulsating stars.

3 Spectropolarimetry

For the purpose of studying stellar magnetism, astronomers have access to two key observable features, both based on variations in the spectra of stars and requiring high resolution spectra in order to observe.

The first of these features is known as Zeeman splitting, and corresponds to certain spectral lines being split into 'multiplets' whose separation depends on field strength, as well as the Landé factor and wavelength of the spectral line in question [48]. When an atom is placed in an external magnetic field, its spectral lines split into several components, in a phenomenon known as Zeeman splitting. The wavelength of the central π component is the same as the original wavelength of the line without magnetic field. In the case of three total components, the other two components have equal displacement from the original wavelength and are shifted to higher (red-shifted, σ_-) and lower (blue-shifted, σ_+) wavelengths. The splitting of spectral lines into multiple components according to the normal Zeeman effect occurs only for singlet states, that is when the spin is zero.

The magnetic splitting of spectral lines in the linear (weak field) Zeeman regime is symmetric with respect to the unperturbed wavelength λ_0. Using the example of a three-component splitting, the wavelength displacement of the red-shifted component σ_- is given by :

$$\Delta\lambda_B = g_{\text{eff}} \frac{eB\lambda_0^2}{4\pi mc^2} \tag{1.1}$$

where g_{eff} is the effective Landé factor, the field strength B is in G, and wavelengths are in Å. By rearranging this equation to solve for B and measuring the wavelength offset in high *Signal-to-Noise Ratio* (SNR) spectroscopic datasets, one can infer the mean surface magnetic field strength $\langle B \rangle$ over the visible stellar hemisphere. While Zeeman splitting can give an indication of the presence of magnetism in stars, it is not as reliable nor as precise as spectropolarimetry, as it is strongly impacted by the rotational profile of the star. Only in particularly slow rotators (of the order of a few km s^{-1}), is it still possible to measure $\langle B \rangle$ directly from observed Zeeman

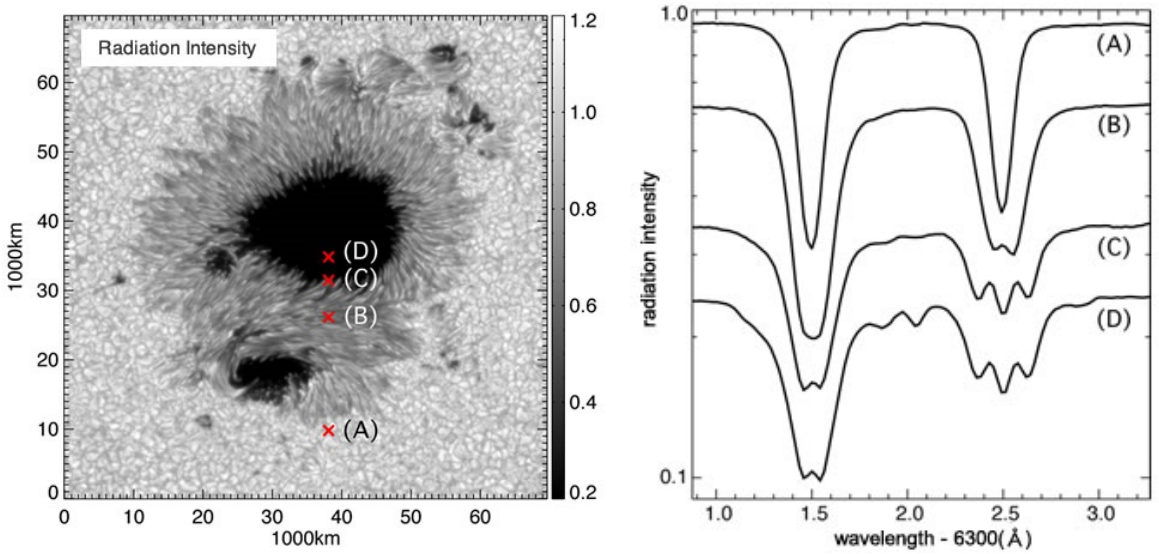

(a) (b)

FIGURE 1.3 – Sunspot observed by Hinode's Solar Optical Telescope [2] in December 2006 (a), with spectra taken at four different locations (b), demonstrating the splitting of absorption lines due to the Zeeman effect induced by the local magnetic field.

patterns in a stellar spectrum, though this understandably severely limits the applications of this technique.

The second technique, and the one exploited during this thesis work, is spectropolarimetry. It uses the fact that, in addition to being split in wavelength, the Zeeman components are polarised : π components are linearly polarised, while σ components are both circularly and linearly polarised. In a spectropolarimeter, the incoming stellar flux passes through a combination of wave plates, splitters, and other optical devices, resulting in two beams of orthogonally polarised starlight. The difference between the two beams provides us with information on the expression of the magnetic field (should one exist) along the line of sight for circular polarisation and perpendicular to the line of sight for linear polarisation.

For the purpose of quantifying the different polarisations of light, it is common to represent it as one (or several) of the four Stokes parameters, defined as follows. The I parameter results from the sum of any two perpendicular polarisations, and corresponds simply to the total intensity. Inversely the Q, U, and V parameters are instead the difference between perpendicular polarisations, such as horizontal and vertical for Q, the two diagonals for U (combining both horizontal and vertical components), and finally clockwise and counter-clockwise circular for V.

To date, there are three high-resolution spectropolarimeters operating in the visible on 2m-class and larger telescopes : ESPaDOnS [49] operating at the Canada-France-Hawaii Telescope on Mauna Kea, Hawaii ; NeoNarval [50-52] at the Télescope Bernard Lyot on Pic du Midi, France ; and HARPSpol [53] on the ESO-3.6m telescope at La Silla, Chile.

Using the case of ESPaDOnS as an example, for a given Stokes parameter, a spectropolarimetric observation consists of four sub-exposures taken at different orientations of the half-wave

2. https://prc.nao.ac.jp/extra/uos/en/no06/

or quarter-wave plate. Each sub-exposure corresponds to a different position of the wave plate relative to the optical axis of the beam splitter. For Stokes Q and U the exposures are taken at four positions of the half-wave plate with 45° increments of rotation, with a 22.5° offset between Q and U. For Stokes V a quarter-wave plate is used instead, with rotations at 90° increments and an initial offset of 45°.

While the individual instrument profiles and data reduction processes vary somewhat between the aforementioned instruments, the resulting reduced data is in a form suitable for the standard exploitation routines regardless of the instrument of origin. This is extremely beneficial, as we can potentially submit proposals for all three instruments each semester, providing a continuous influx of new data that is directly comparable, as well as in some cases sequential observations of the same target, giving us greater coverage of the different phases of a star's rotation.

Ideally, combining these two techniques provides the fullest image of the magnetic field expression for a given star, however due to the constraints in rotational velocity demanded by Zeeman splitting analysis this often proves difficult to achieve.

In 2019, the Narval instrument was given a hardware upgrade with the intention of increasing stability in radial velocity measurements (< 3 m s^{-1} goal), at the cost of reduced instrumental resolution (68,000 $\rightarrow$ 53,000), and becoming NeoNarval. With this instrumental upgrade came a brand new data reduction pipeline, entitled the *Data Reduction Software* (DRS), which included a super-resolution algorithm that was intended to recover the lost instrumental resolution, and ensure that the addition of velocimetry would not negatively impact the spectropolarimetry it was already doing.

However, since the upgrade there have been a number of issues reported with regards to the quality of the results in polarimetry as well as the precision in velocimetry. While issues related to the hardware must be solved by on-site engineers and technicians, we can try to diagnose these issues and mitigate their effects in post-processing, while simultaneously developing software to improve the data reduction aspect. It is with this in mind that my colleague C. Gutteridge and I have taken the initiative to develop a novel data reduction pipeline, entitled PyReduce, to investigate these issues and eventually offer to the wider community an alternative to the DRS. My contributions to this effort are presented in Appendix A, with the full depth of the project described in Thomson-Paressant et al. [54] and Gutteridge et al. (in prep.).

4 (Magneto-)Asteroseismology

Asteroseismology is the study of the internal structure of stars via the study of internal modes. The characteristics of these oscillations are determined by the layout of the stellar interior, being impacted by factors such as density and chemical composition, and thus through this technique we can infer the internal structure as a result.

Stellar oscillations can be represented by a sum of modes, each characterised through several parameters, including its frequency, lifetime (also known as coherence time), amplitude and geometry. The geometry of each mode is characterised by its radial order (n), indicating the

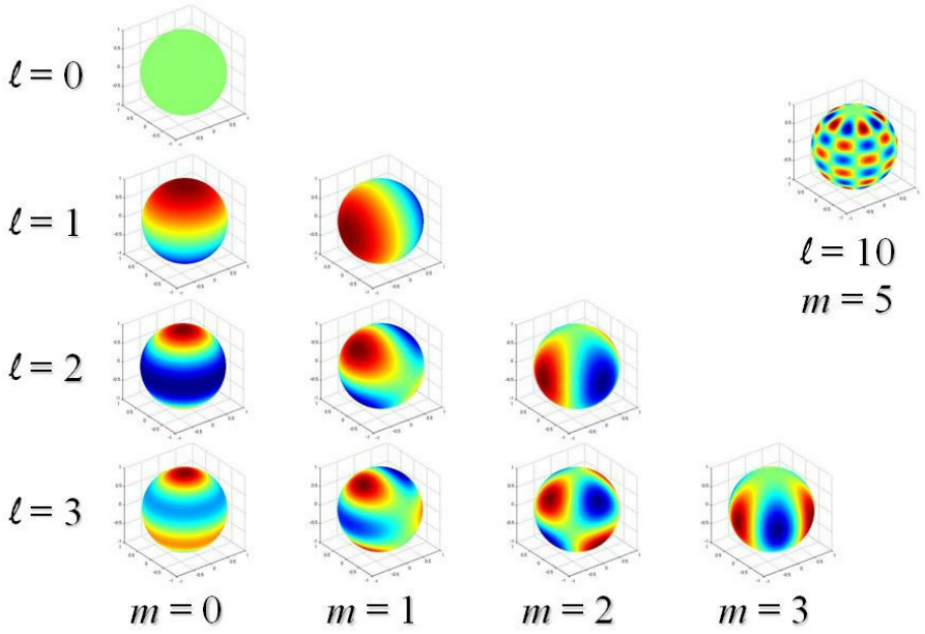

FIGURE 1.4 – Spherical harmonic functions for $m = (0, 1, 2, 3)$ and $l = (0, 1, 2, 3)$. An example of what the $(l, m) = (10, 5)$ case looks like is shown in the top right corner. Image taken from SAHOO, GUINNESS & REICH [55].

number of nodes in the radial direction, the spherical degree (l), specifying the number of nodal lines on the surface, and the azimuthal order (m), which designates the number of nodal lines that pass through the rotation axis. An example of how some of these mode parameters express themselves is visible in Fig. 1.4.

Provided at least two stellar pulsation modes can be identified and characterised (mode order and degree), then asteroseismic studies can provide information on the density and composition of the star [e.g. 56]. This, however, requires a theoretical prescription to be generated beforehand, which is the basis upon which we expect the internal structure to be organised. The more well-studied modes we can contribute, the tighter the constraints are on the stellar internal structure and therefore the more accurate the model becomes.

When combined with the information gathered from spectropolarimetric observations of magnetic stars, which provides insight into the expression of the magnetic field at the surface of the star, this provides additional constraint for models that describe how the magnetic field must be distributed in the stellar interior. These interior fields are predicted to have important impacts on the structure and evolution of the star, and currently spectropolarimetry is the best way to observationally constrain these parameters, by providing reliably determined surface boundary conditions for the models of internal magnetic fields.

The study of magnetism in combination with stellar pulsations gives rise to magneto-asteroseismology, which is currently our best tool for imposing strong constraints on stellar internal structure models, resulting in a significant improvement to our understanding of stellar evolution theory [57, 58].

Pulsating stars, such as δ Sct and β Cep variables, are particularly important stars in the field of asteroseismology as their population sizes are broad, the regions corresponding to their pulsation modes are well-defined, and allow for the study of different regimes of stellar interiors. The presence of magnetic fields within these stars allow us to place additional constraints on the modelling of this internal structure [e.g. 59-61]. For example, even a relatively weak field is enough to inhibit mixing inside the star and suggests convective overshooting to be negligible [56].

Magneto-asteroseismology has been accomplished so far for only three hot stars, but several promising candidates are currently being investigated. One of these well-studied examples is the β Cep pulsator V2052 Oph, where convective core overshooting was shown to be negligible following asteroseismic modelling [56]. This outcome is significant, as overshooting is generally a prerequisite for reproducing the observed pulsation frequencies in non-magnetic hot stars [e.g. 62, 63]. V2052 Oph's inferred magnetic field strength ($B_{\rm pol} \sim 400$ G)[64] is above the theoretical critical field limit [65] needed to inhibit non-standard mixing processes inside this star, but in order to test the veracity of this hypothesis a larger sample of pulsating magnetic stars either side of this limit is needed.

It is therefore essential to develop a statistically significant baseline of well-studied magnetic pulsating stars, which would allow us to perform magneto-asteroseismic studies of stars across the full spectral type range attributed to hot stars. By identifying additional magnetic variable stars and performing in-depth spectropolarimetric and pulsational studies on them, preferably with a wide variety of natures to fill out the parameter space, we will be able to make significant advances in this area.

It is with exactly this in mind that my thesis work has focused almost exclusively : studying the magnetic fields and pulsation modes of δ Sct stars with the goal of expanding what is currently a very limited sample. Once a sufficiently large database has been developed, we can be picky as to which targets we select – taking into account factors such as brightness, magnetic field strength, and pulsation mode frequencies – to perform in-depth magneto-asteroseismic modelling of key stars. By combining these results with those of my colleagues studying other pulsators, we will be able to achieve a full picture of the interactions between pulsation modes and magnetic field, and consequentially a greater understanding of the interior structure of stars across the H-R diagram.

5 Standard procedural routine

5.1 Least Squares Deconvolution (LSD)

In order to study stellar magnetism, we use the circular polarisation mode of spectropolarimetric instruments to measure the Stokes V spectrum along with the intensity spectrum Stokes I. The four sub-exposures taken as part of a single observation are also destructively combined to produce a null polarisation spectrum, labelled N, to check for pollution by factors such as variable observing conditions, instrumental effects, or non-magnetic stellar effects such as pulsations. In addition, successive Stokes V sequences can be acquired to increase the overall SNR

of a potential magnetic measurement.

We then utilise the *Least Squares Deconvolution* (LSD) method [66] to calculate the average spectral line profile and Stokes V profile of each measurement. This technique works by combining all available lines in the spectrum, with a weight that depends on the Landé factor g_L of the line, i.e. its sensitivity to the presence of a magnetic field, and the depth of the line. This improves the SNR of the combined line compared to a single line. LSD assumes the weak field hypothesis and that all lines used in the combination have the same local profile.

To compute the necessary line mask, lines are usually selected from the VALD3 database [*Vienna Atomic Line Database*, 67-69], which provides atomic data for stellar atmospheres. We select a line mask based on the surface gravity $\log g$ and effective temperature $T_{\rm eff}$ of the star we seek to study. From this template mask, we then remove all hydrogen lines and any lines blended with either telluric lines or hydrogen lines, as well as lines present in the original VALD line list that do not appear in the observed spectrum for the star in question. Finally, the depths of individual spectral lines are adjusted, either by hand or using an automated system, in order to make the template mask more closely match the stellar spectrum, following the procedure described in Grunhut et al. [70]. Due to variations in metallicity and possible chemical peculiarities, the stellar spectra acquired from observations will inevitably differ from synthetic ones generated from atmospheric model codes, which only take into account effective temperature and surface gravity as mentioned previously, making this an important step for accurately and reliably retrieving the spectral information from spectropolarimetric observations. This results in an improvement in SNR of the output LSD profiles of a factor 2 or more.

Once all these steps have been completed, the end result is a fine-tuned line mask that is specific to that particular star's spectrum, and can be utilised for analysing all current and future spectra for the given target. It is from this point that measurements of the magnetic field can be performed, via variation in the LSD Stokes V profile.

5.2 Determining longitudinal magnetic field B_l values

Using the LSD Stokes profiles generated in the previous step, we can calculate the longitudinal field values B_l for each target in a given sample [71, 72]. To this end, we define a region around the centroid of the line such that it includes the full line profile, while limiting the contribution of the continuum, and calculate the integral of the Stokes V profile, normalised by the Stokes I profile, as follows :

$$B_l = \frac{1}{C\,\overline{g}\,\overline{\lambda}} \frac{\int \nu V(\nu) d\nu}{\int (1 - I(\nu)) d\nu} \tag{1.2}$$

where $\overline{g}$ and $\overline{\lambda}$ are the mean Landé factor and mean wavelength respectively, and $I(\nu))$ and $V(\nu))$ correspond to the LSD Stokes I and V profiles.

It is important to define an appropriate region about the line profile, as selecting one that is too large or too small can cause erroneous results. For stars for which multiple epochs of observation have been acquired, a B_l value is calculated for each, typically phased with respect to the rotation period if known *a priori*. Here, space telescope photometry from *Kepler* and

TESS has been invaluable for accurately determining the rotation periods of the various stars studied as part of this thesis.

In addition to calculating the B_l and N_l values, we apply a *False Alarm Probability* (FAP) algorithm to each observation to verify our results, which determines the probability that there is a signal in Stokes V and not in the N profile in the same velocity region as used for the B_l calculations above, and similarly for the regions *outside* the profile region. The FAP algorithm follows the detection criteria described in Donati et al. [73], such that a definite detection requires FAP $\lesssim 10^{-5}$, a marginal detection corresponds to $10^{-5} \lesssim$ FAP $\lesssim 10^{-3}$, and a non-detection is determined to apply for values FAP $\gtrsim 10^{-3}$.

5.3 Polar magnetic field $B_{\rm pol}$ calculation

Once B_l values have been determined for a given target, ideally phased with respect to the rotation period, we can attempt to infer the polar field strength $B_{\rm pol}$ of the star. To this end we typically assume a dipolar field structure, which is a safe assumption as dipolar fields are the most common type of field that we can observe, and indeed in many cases it is the best fitting model to the magnetic measurements. Calculating $B_{\rm pol}$ involves several successive steps, including the determination of a few stellar parameters such as inclination i between the rotation axis and the line of sight and magnetic field obliquity β, which corresponds to the angle between the magnetic axis and the rotation axis of the star.

Ideally, a value for i has been determined from previous spectroscopic studies of the target [e.g. 74, 75], but failing that it can be calculated using a combination of stellar parameters. In the latter case, using the values from *Gaia* [76] for effective temperature $T_{\rm eff}$ and absolute magnitude M_v, the value from *TESS* for rotation period $P_{\rm rot}$, inferring the rotational velocity $v \sin i$ using the Fourier method on the LSD Stokes I profile, as well as the radius-luminosity-temperature relation, we can calculate a value for the inclination using an Oblique Rotator Model first defined by Stibbs [77] :

$$\frac{L}{L_\odot} = 10^{0.4(4.85-M_v)} \qquad \frac{R}{R_\odot} = \left(\frac{T}{T_\odot}\right)^{-2}\left(\frac{L}{L_\odot}\right)^{1/2} \qquad i = \sin^{-1}\left(\frac{v \sin i\, P_{\rm rot}}{2\pi R}\right) \tag{1.3}$$

Using this determined value for i, in combination with the ratio between the minimum $B_{l,min}$ and maximum $B_{l,max}$ longitudinal field values, we can then determine a value for β with respect to the inclination [78] by solving the left-hand equation below and finally, putting all this together, a value for $B_{\rm pol}$:

$$\frac{B_{l,min}}{B_{l,max}} = \frac{\cos(i+\beta)}{\cos(i-\beta)} \qquad B_{\rm pol} = \frac{4(15-5u)}{15+u}\frac{B_{l,\pm}}{\cos(i \mp \beta)} \tag{1.4}$$

The right-hand equation has been taken from Schwarzschild [79], and u corresponds to the limb-darkening coefficient for the target, determined from the tables calculated by Claret [80] and based on the surface gravity $\log g$ and effective temperature $T_{\rm eff}$ of the star in question.

5.4 Upper limit estimation

In the event of a lack of magnetic field detection for a given star, we can perform simple modelling to determine the maximum dipolar field strength of a magnetic field that might have remained hidden in the noise of the data. This allows us to provide an upper limit to $B_{\rm pol}$ for each target, and perhaps conclude whether these stars are worthy magnetic candidates. This algorithm calculates 1000 oblique dipole models for each of the LSD Stokes V profiles using random values for inclination angle i, obliquity angle β, rotational phase, and a white Gaussian noise with a null average and a variance corresponding to the SNR of each Stokes profile. For a more detailed description of the process, we refer the reader to Neiner et al. [81]. We can then calculate the rate of detections from these 1000 models.

Thanks to the fact that in many cases we have multiple observations available for a given target, we can combine the calculated upper limit statistics in order to extract a more strict value, taking into account that a magnetic field has not been detected in any of the observations. We can achieve this using the following equation :

$$P_{\rm comb} = 100 \left[1 - \prod_{i=1}^{n} \frac{(100 - P_i)}{100} \right] \tag{1.5}$$

where P_i is the detection probability for the ith observation and P$_{\rm comb}$ is the detection probability for n observations combined. All probabilities are expressed as a percentage.

As an example, if for a particular target we have three observations available with probabilities of 70, 80, and 90 per cent respectively that no field stronger than 1000 G was detected, the combined probability with the same condition is 99.4 per cent.

5.5 Zeeman Doppler Imaging (ZDI)

Zeeman Doppler Imaging (ZDI) is a modelling technique used to reconstruct the expression of the magnetic field at the surface of stars [82, 83]. It uses the Stokes profiles generated from the LSD method applied to spectropolarimetric datasets, and represents the magnetic field as a combination of spherical harmonics while also using a maximum entropy regularisation procedure [84].

The code operates by fitting a synthetic line profile to each of the Stokes V profiles provided from observations, where the spherical harmonic coefficients that describe the expression of the magnetic field are initially set as free parameters. The classic input parameters for generating the model line profiles are a mean Landé factor and mean wavelength (both of which are provided by performing LSD), as well as the amplitude and width parameters from a Gaussian fit to the Stokes I profiles. The line profiles are then weighted by the projected area and surface brightness for a given observation and 'slice' of the stellar surface, and then Doppler shifted by the rotational velocity. Typically, brightness variations due to surface spots are neglected, as they are assumed to contribute only minor variations (∼1-5%). Conversely, there is a strong dependence on both $v \sin i$, which impacts the resolution of the resulting magnetic maps, and the inclination, where for some values of i there can be cross-talk between the radial and azimuthal magnetic fields.

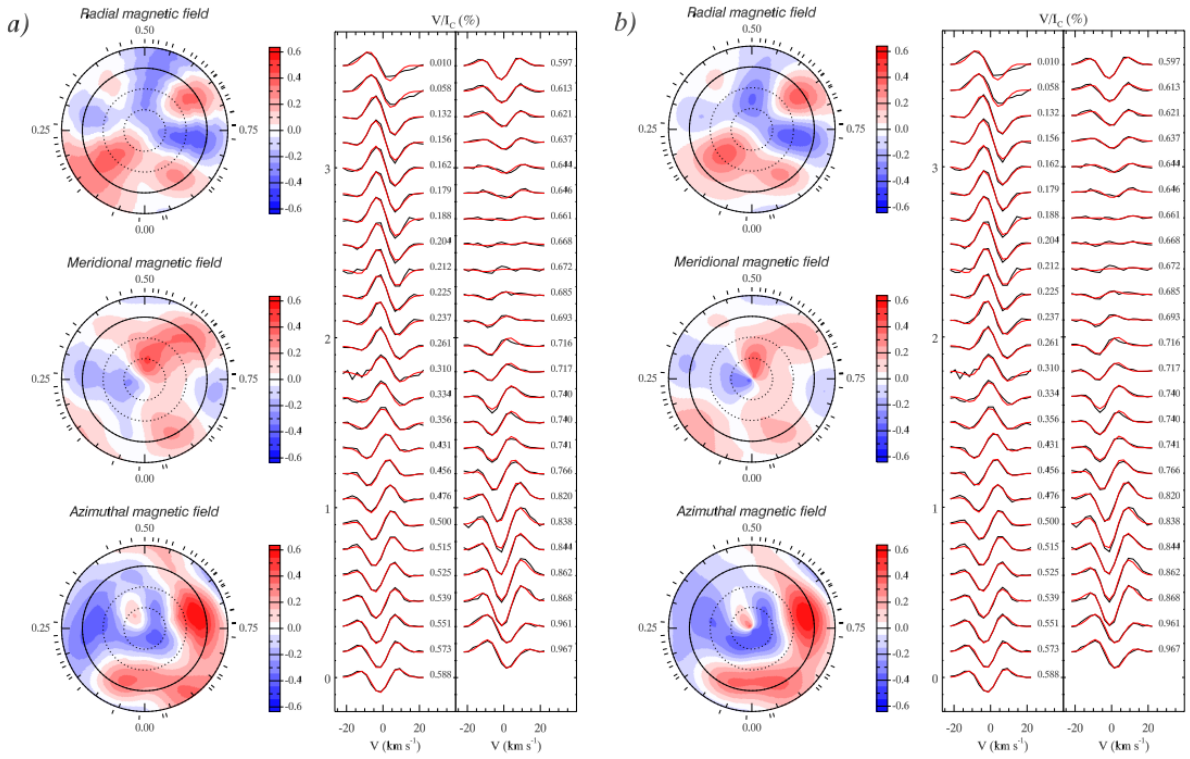

FIGURE 1.5 – Global magnetic field topology of τ Sco derived with ZDI inversions for two different parametrisations. In both cases, the left panel shows the flattened polar projection of the radial, meridional, and azimuthal field components, with the corresponding colourbar indicating the field strength in kG. The observed (black) and computed (red) LSD Stokes V profiles are shown on the right-hand side, and offset with respect to rotational phase. Image taken from KOCHUKHOV & WADE [85].

An example of ZDI is provided for the magnetic OB star τ Scorpii in Fig. 1.5.

ZDI requires good phase coverage and high SNR in order to accurately reconstruct the small-scale variations of the magnetic field over the full rotation period of the star. Recent developments in the coding of ZDI methods now allow for the characterisation of pulsation modes *in addition* to the standard magnetic mapping (Gutteridge et al., in prep.), which is a great boon for the study of pulsating variable stars such as the δ Sct.

Chapter 2

A search for magnetic δ Scuti stars in Kepler hybrid candidates

Objectives

Numerous candidate hybrid stars of type δ Scuti - γ Doradus have been identified with the *Kepler* satellite. However, many of them lie outside the theoretically expected instability strip for hybrid pulsation, where δ Sct and γ Dor pulsations can be simultaneously excited. We postulate that some of these pulsating stars may not be genuine hybrid pulsators but rather magnetic δ Sct stars, for which the rotational modulation from spots on the surface associated to the magnetic field produces frequencies in the same domain as γ Dor pulsations. We search for the presence of a magnetic field in a small sample of selected hybrid δ Sct - γ Dor stars using spectropolarimetry. At the time of observations, the only δ Sct star known to have a magnetic field was HD 188774 with a field strength of a few hundred Gauss. Our observations were thus tailored to detect fields of this typical strength. We find no magnetic field in the hybrid candidate stars we observed. However, two of the three other magnetic δ Sct stars discovered since these observations have much weaker fields than HD 188774, and are of dynamo origin rather than fossil fields. It is likely that our observations are not sensitive enough to detect such dynamo magnetic fields in the cooler stars of our sample if they are present. This work nevertheless provides reliable upper limits on possible fossil fields in the hotter stars, pointing towards typically weaker fields in δ Sct stars than in OBA stars in general.

Work based on Thomson-Paressant et al., MNRAS, **526**, 2, p1728-1741 (2023) [86]

Contents

1 Introduction

Prior to the first high-precision photometric satellite observations, such as those from the *Convection, Rotation and planetary Transits satellite* (*CoRoT*) satellite [87], the *Kepler* satellite [88], and *TESS* [89], very few hybrid δ Sct-γ Dor pulsators were known [e.g. 90]. Thanks to the space-based large scale surveys and the precision of their results, hundreds of potential hybrid candidates have since been identified. In particular, data collected by the *Kepler* mission [91, 92] suggest that the number of hybrid candidates is much higher than expected. If these candidates were indeed confirmed to be true hybrids, current theory would need to be seriously revised [see 91, 93], and thus it is very important to assess whether they are indeed genuine hybrid pulsators.

If we assume these candidates are *not* δ Sct-γ Dor hybrids, two alternative explanations for the presence of low frequency variability within these stars can be put forward :

- either the δ Sct star is a member of a binary (or multiple star) system, in which case the low order frequencies could originate from the orbital period of an eclipsing or ellipsoidal system. Additionally, the δ Sct star could host tidally-excited g-modes pulsations or could be distorted by tidal interactions with its companion(s). There is also the possibility of the companion being an unresolved γ Dor variable while the δ Sct frequencies would appear to originate from the target star.
- or, due to the presence of a magnetic field, the δ Sct star could display some surface inhomogeneity. In this case the low frequencies would be attributed to rotational modulation rather than g-modes.

Magnetism invariably leads to a photometric signal at the stellar rotation period due to surface inhomogeneities, both for large-scale fossil fields [e.g. 96] and for smaller-scale dynamo fields [e.g. 97, 98]. Thus, rotational variable stars are prime candidates for magnetic measurements. However, rotation periods may be long (up to years or decades in extreme cases), and/or photometric amplitudes may be low so that not all magnetic stars will exhibit a detectable photometric rotational signal over a given time baseline.

In a study of the candidate hybrid star HD 188774, Lampens et al. [99] determined that the low frequencies in the variations of the light and radial velocity were related to each other : one harmonic and its parent frequency, but the phased curves were not corresponding to those of

Target	Mass ($M_\odot$)	$T_{\rm eff}$ (K)	$v \sin i$ (km s^{-1})	B_l (G)	$B_{\rm pol}$ (G)	Spectral type	Magnetic characterisation
HD 188774	2.61 ± 0.1	7600 ± 30	52 ± 1.5	[23 : 76]	~ 250	A7.5IV-III	Dipole fossil field
ρ Pup	1.85 ± 0.2	6675 ± 175	8 ± 0.4	[-0.29 : -0.05]	$\sim$1	F2IIm	Ultra-weak fossil field
β Cas	1.91 ± 0.02	7080 ± 20	70 ± 1	[-6 : 4]	$\sim$20	F2III	Dynamo field
HD 41641	2.3 ± 0.6	7200 ± 80	30 ± 2	[-178 : 182]	1055	A5III	Complex fossil field

Table 2.1 – Table of information regarding the four confirmed magnetic δ Sct stars discovered at time of publication, with values being retrieved from their respective papers [42, 44, 94, 95]. Columns 2, 3 and 4 detail the stellar parameters namely stellar mass, effective temperature, and rotational velocity respectively. Column 5 provides the range of observed longitudinal field values, while column 6 gives an estimate of the polar field strength assuming a dipolar field.

a binary system. As a result, they excluded binarity as a source of the low frequencies present. Therefore, Neiner & Lampens [41] tested the latter of the two above hypotheses for the same star and found that this star possesses a weak magnetic field. The rotation period inferred from subsequent magnetic field measurements (Neiner et al., in prep.) corresponds to the lowest frequency which, together with the first harmonic, was initially attributed to γ Dor pulsations [92]. Thus, HD 188774 is not a genuine hybrid pulsator but a magnetic δ Sct star. The relatively simple observed Zeeman signatures point to a fossil origin (as for OB and Ap stars) of the 258 ± 63 G field, rather than to a dynamo field. This is also consistent with the long-term stability of the spots at the surface of HD 188774, verified in the *Kepler* lightcurve [94]. Since then however, a few other magnetic δ Sct stars have been discovered, with a more complex fossil field [HD 41641, 95], a dynamo field [β Cas, 44], or an ultra-weak field [ρ Pup, 42]. Magnetism in δ Sct stars thus seems rather diverse. The properties of these four confirmed magnetic δ Sct stars are summarised in Table 2.1. Note that all but HD 41641 are somewhat evolved stars.

There have been several other claims of magnetism found in δ Sct stars. For example, HD 21190 was found to be a magnetic δ Sct star by Kurtz et al. [45] and Hubrig & Scholler [100] but, while the δ Sct status was confirmed by Barac et al. [101], Bagnulo et al. [102] showed that the magnetic detection was spurious. HD 35929 is another potential candidate found by Alecian et al. [47], but their magnetic detection was only tentative and this star is a pre-main sequence Herbig star. Other magnetic δ Sct targets suggested in the literature are assumed to be magnetic stars due to their Ap nature or spectral properties but had no spectropolarimetric measurements performed yet [e.g. 103] or have a detected magnetic field but are not confirmed δ Sct stars so far [e.g. 104]. These stars are very good magnetic δ Sct candidates but since they are not confirmed yet they are not included in Table 2.1. Indeed, for a few such candidates a spectropolarimetric study was performed and did not detect the presence of a magnetic field [e.g. β Pic, 105]. It is thus necessary to remain conservative before listing stars as bona fide magnetic δ Sct stars.

2 Target selection

2.1 Sample

Following the detection of a magnetic field in HD 188774 [41], we decided to search for magnetic fields in several other δ Sct - γ Dor hybrid candidate stars from the *Kepler* mission. An initial sample of about 50 bright A/F-type hybrid candidates were proposed by Uytterhoeven et al. [92], using complementary, follow-up spectroscopic data collected with the HERMES spectrograph [106] attached to the Mercator telescope [107]. We then selected targets from this sample that either are hotter than the [6900 - 7400] K temperature range where hybrid pulsations are predicted by theoretical models [108] – this concerns BD+41°3389, HD 175841, HD 175939, HD 181206, HD 181569, HD 183280, and HD 226284 –, or show apparently complex low frequency variability which could include signals related to rotation – e.g. BD+42°3370 and HD 185115. In addition, BD+40°3786 and two stars without δ Sct pulsations – HD 187254 and HD 178874 (see Fig. 2.1) –, were chosen based on a preliminary classification as candidates for stellar acti-

vity/rotational modulation [92, cf. their figs. 7 b and c]. In this way, we pre-selected a set of 12 targets of *Kepler* magnitude (Kp) between 6.9 and 9.9 mag.

The spectral types of the selected targets range from A5 to F3 while the $v \sin i$ values go from 15 to 240 km s^{-1}. The Lomb-Scargle periodograms of various candidates display low-frequency peaks with the ratio (3 :)2 :1, which might indicate that rotation is a key player. This was indeed the explanation for the two most dominant low frequencies detected in the light and radial velocity curves of the first detected magnetic δ Sct star, HD 188774 [41].

While there was no direct evidence of binarity based on the multi-epoch HERMES spectra for all our targets, this was later on invalidated for three of them. Indeed, HD 175939, HD 185115, and BD+42°3370 were all previously classified as 'P+VAR' with 'VAR' meaning 'low-amplitude RV variability for a yet unknown reason' in Lampens et al. [107], but they meanwhile turned out to be long-period spectroscopic binaries [109].

2.2 *Kepler* frequency analysis

The Period04 package [110] was used to generate periodograms from the *Kepler* photometry to measure periodic signals in the standard way, using photometric amplitudes rather than unitless power. There are generally three types of signals of interest to this study : high-frequency δ Sct pulsation [usually $\gtrsim 5$ d^{-1}, but can also be found at lower frequencies, 111], low-frequency γ Dor pulsation (usually $\lesssim 5$ d^{-1}), and rotational modulation. Rotational frequencies of our targets must be below $\sim$4 d^{-1}, which is the critical rotation frequency for an A/F type main sequence star (the critical rotation frequency only decreases for more evolved stars). Besides the expected frequency range of these signals, other patterns in the periodograms can aid in the interpretation of the detected signals. Rotational modulation is generally non-sinusoidal in its photometric signature, and thus harmonics of the rotational frequency are expected [e.g. 59]. γ Dor pulsation is usually characterised by groups of closely spaced frequencies [112, 113], and δ Sct pulsators exhibit multiple pulsation modes which may span a wide range of frequencies or may be more clustered in groups [but usually at significantly higher frequencies than the γ Dor modes ; 113, 114].

All of our targets were observed by *Kepler* in long cadence (LC) mode (30-minute cadence), and all but one (KIC 9775454 = HD 185115) were also observed in short cadence (SC) mode (1-minute cadence). Both the LC and SC data have benefits and limitations. The LC photometry tends to have (often significantly) longer observational baselines and thus provides a higher frequency resolution. However, with a Nyquist frequency of 24 d^{-1}, there are challenges in measuring high frequency signals (including, in principle, δ Sct pulsation). A further complication is that any signals above the Nyquist frequency will be reflected to lower frequencies, potentially causing aliased peaks even in the low frequency regime [115]. SC data, with a Nyquist frequency of 720 d^{-1} excels at detecting high frequency signals and does not suffer from this 'alias reflection' problem, but with shorter time baselines (typically 10 to 30 d for our sample) the frequency resolution is poor. We considered both the LC and SC data for our sample (barring HD 185115 with only LC data) to i) obtain high frequency resolution, ii) ensure that the (especially lower frequency) peaks are genuine and not aliases, and iii) probe out to higher frequencies. For

stars where the periodograms generated from the SC data are not shown, they do not add any information not already communicated by the LC data (due to a higher noise floor and lower frequency resolution in the SC data and a lack of significant signals beyond 24 d^{-1}).

The main results of our frequency analysis are shown in Fig. 2.1. The periodograms for each star are separated into two regimes, up to 5 d^{-1} (where rotation and γ Dor pulsation are most prominent), and up to 24 d^{-1} (or to 40 d^{-1} for the four stars with higher frequencies in the SC data). For all the stars in the sample, none of the low frequencies (< 5 d^{-1}) are 'Nyquist reflections' of higher frequencies. However, we caution that in some cases there are relatively low amplitude signals higher than 24 d^{-1} so that any quantitative analysis of the δ Sct pulsations should consider the SC data. Candidate rotational frequencies (identified as such by the presence of one or more harmonics) are seen in all but three of the targets. In some cases a second harmonic series is detected, so that the candidate rotational frequency of the star is ambiguous with photometry alone. However, for this study the important characteristic is the (likely) presence of rotational modulation even if the 'true' stellar rotational frequency cannot be determined with the available data.

The three stars without any clear harmonics in the low-frequency regime (HD 175841, BD+40° 3786, HD 185115) probably owe their low frequency signals to pulsation. In the case of BD+40° 3786, the non-detection of rotational modulation in our study contradicts the indications shown by Uytterhoeven et al. [92]. It and the two other previously mentioned stars were nevertheless kept in the sample for confirmation and comparison. γ Dor pulsation typically follows a pattern where signals are found in densely-packed 'frequency groups', the strongest located near the stellar rotational frequency, the next strongest at twice the stellar rotational frequency, and so on [116]. HD 175841 and BD +40°3786, however, do not follow this pattern and thus their frequency spectra are more ambiguous. In addition, HD 185115 is a long-period binary and this system could contain a δ Sct component and a γ Dor component.

Even among those with candidate rotational modulation, there are often additional signals in the low-frequency regime which are unrelated to the harmonic structures and could better be explained by pulsation. Stars with low-frequency signals that do not correspond to rotation may be genuine hybrid pulsators, could be cases where δ Sct pulsations extend into the lower frequency regime, or an undetected binary with a δ Sct component and a γ Dor component.

In some δ Sct stars, low- and high-frequency pulsation modes can couple [e.g. 117]. While a comprehensive analysis of all detected frequencies in our sample is beyond the scope of this work, there are four stars where such a coupling seems evident. These are indicated in Fig. 2.1, where the spacing between the two higher-frequency signals marked with open and filled circles is equal to the low-frequency signal marked by a filled square. HD 183280 has two pairs of high frequency signals with the same spacing. BD+42°3370 has two low frequency signals which both seem to couple to the same high frequency signal. For a detailed analysis of its pulsations, we refer to the study by Samadi-Ghadim, Lampens & Gizon [118]. The authors discovered many multiplets of rotationally split g- and p-modes as well as the candidate rotation frequency with two harmonics in the low region of the Fourier spectrum. Such coupling may be of asteroseismic interest, especially if rapid rotation is somehow related [as hypothesized in 117]

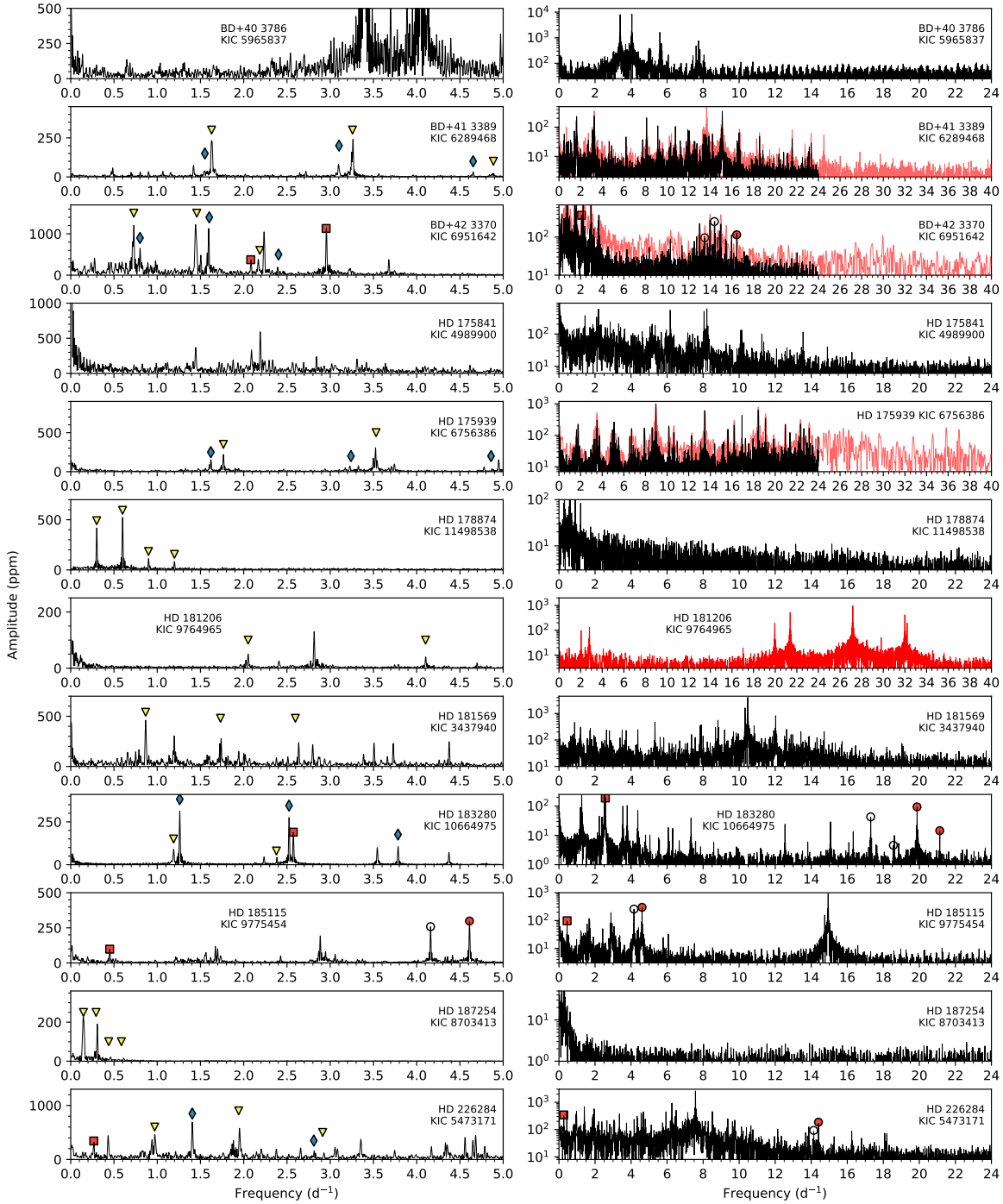

FIGURE 2.1 – Frequency spectra (periodograms) from *Kepler* photometry for the sample, from Cycle 6 (black), and in some cases from short cadence data (red). The left column shows the low frequency regime (<5 d^{-1}), and the right column goes out to 24 d^{-1}, or 40 d^{-1} for the four stars with frequencies above 24 d^{-1} (detected in the short cadence data, which has a higher noise floor due to shorter observing baselines). A linear scale is used in the left column, and a log scale on the right (to make low amplitude signals more visible). Triangle and diamond symbols mark harmonic series. Red squares mark low frequencies equal to the difference between two higher frequency signals (indicated by filled and open circles). For HD 183280, both pairs of filled and open circles correspond to the same difference frequency.

The candidate rotational signals identified in the *Kepler* data of our sample are similar to those found in the two known magnetic δ Sct pulsators with relatively strong fossil fields, listed in Table 2.1. In HD 41641, which hosts a complex fossil field, there is a rotational signal at 2.8077 d (0.3562 d^{-1}) with two clear harmonics seen in the *TESS* space photometry [extracted and analysed by us, and in agreement with *CoRoT* observations by 119]. HD 188774, with a dipole fossil field, also has a rotational signal (with harmonics) in *Kepler* data with P = 2.90711 d (0.3440 d^{-1}). In β Cas, with a weak dynamo field, *TESS* could not detect a rotational frequency [44], perhaps due to a low photometric amplitude, even though with $P_{\rm rot} \approx 0.868$ d, about 57 rotation cycles were covered by the analysed *TESS* data. *TESS*, however, has lower photometric precision compared to *Kepler* (and *Kepler* did not observe this star). Another potential rotation period value has recently been put forward for β Cas at 1.518 d (V. Antoci, private communication). This period is visible with very low amplitude in the *TESS* data, as well as a potential first harmonic. Rotational modulation is not seen in the *TESS* photometry of ρ Pup (with an ultra-weak fossil field). ρ Pup is a very slow rotator ($v \sin i = 8 \pm 0.4$ km s^{-1} [120]), which makes rotation more difficult to detect in the relatively short duration *TESS* lightcurves.

3 Spectropolarimetric observations

The targets were observed with ESPaDOnS [49], operating on the Canada France Hawaii Telescope (CFHT) at the Mauna Kea Observatory, Hawaii. The observations were taken over a period of three months, between 2016 April 17 and 2016 June 24. The list of targets and their respective observations are available in Table 2.2. The exposure time used for each target was defined by considering the stellar properties (in particular temperature and $v \sin i$) and assuming that the field possibly present in the targets is of the same order of magnitude (∼250 G) as the one already detected in HD 188774 (which was the only magnetic δ Sct known at the time of observations). In practice this threshold also depends on weather conditions during observations, as the SNR we can achieve for a given observation can vary. Successive Stokes sequences were taken for most targets, in order to reach the overall SNR required for that theoretical magnetic field threshold (see Table 2.2).

A near identical process as the one described in Chap. 1 Sec.5.1 was followed for these targets, with one key difference. Prior to running the LSD method [66], we performed continuum normalisation using the *SPEctral Normalization Tool* (SpeNT) [10] for all the spectra of each target, as we noticed the automated normalisation done by LibreEsprit did a poor job of fitting the blue region of the spectra. Additionally, we calculated synthetic spectra with the SYNSPEC49 code [121] - combined with the ATLAS9 [122] and ATLAS12 [123, 124] codes for atmospheric and chemical abundance modelling - and utilised them to ensure what we were fitting was indeed the continuum and not a "pseudo-continuum" due to the blending of many lines in the blue part of the spectrum. Synthetic spectra were generated using the stellar parameters of the stars (notably $T_{\rm eff}$, log g, and $v \sin i$, cf. Tables 2.2 & 2.3) as a closest approximation, and provided both normalised and unnormalised versions of the spectrum to use as reference.

Target	KIC	Date	Mid-HJD +2457000	T_{exp} (s)	Mean λ (nm)	Mean Landé	SNR	FAP	$B_l \pm \sigma B$ (G)	$N_l \pm \sigma N$ (G)
BD +40°3786	5965837	17-Apr-16	496.1275	1x4x637	534.2117	1.190	1898	ND	10.7 ± 5.4	-3.6 ± 5.4
BD +41°3389	6289468	15-May-16	524.0308	2x4x1318	519.4100	1.196	6715	ND	0.75 ± 116.95	131.65 ± 117.05
		17-May-16	525.9622	2x4x1318	520.5958	1.196	6857	ND	23.75 ± 125.1	-43.85 ± 125.2
BD +42°3370	6951642	19-Apr-16	498.0733	2x4x1498	531.7979	1.191	7106	ND	-23.25 ± 57.1	52.4 ± 57
		22-Apr-16	501.1040	1x4x1498	532.0277	1.191	5010	ND	-9.8 ± 59.4	-61.3 ± 59.6
		14-May-16	523.0732	1x4x1498	529.9560	1.191	4844	ND	-77.6 ± 65.2	-115.7 ± 65.3
HD 175841	4989900	17-Apr-16	496.0864	1x4x987	519.3916	1.202	4885	ND	-42.3 ± 74.6	-74.8 ± 74.5
		19-Apr-16	497.9762	1x4x987	520.4548	1.202	3801	ND	21.7 ± 70.3	70.4 ± 70.6
HD 175939	6756386	19-Apr-16	498.9897	1x4x1231	541.8455	1.196	5798	ND	-77.9 ± 89.6	-68.0 ± 89.8
		20-Apr-16	500.0299	2x4x1231	540.0611	1.196	8209	ND	28.3 ± 83.8	68.3 ± 83.7
		21-Apr-16	500.9817	1x4x1231	542.1242	1.196	5768	ND	82.4 ± 94.8	60.9 ± 94.4
HD 178874	11498538	18-May-16	527.0393	1x4x698	532.8074	1.192	2617	ND	8.4 ± 13.5	7.2 ± 13.6
		19-May-16	527.9048	1x4x698	537.8895	1.192	2678	ND	0.7 ± 10.1	-8.2 ± 10.0
		10-Aug-16	611.4466	4x4x593	523.0904	1.194	3468	ND	-2.43 ± 16.4	-0.025 ± 16.4
HD 181206	9764965	22-Apr-16	501.0394	10x4x79	545.7981	1.204	6699	ND	14.12 ± 161.95	-21.76 ± 162.19
		19-May-16	527.9511	10x4x79	544.3413	1.205	7011	ND	13.27 ± 158.54	-3 ± 158.34
HD 181569	3437940	17-Jun-16	557.1169	4x4x206	528.8988	1.194	6036	ND	-28.0 ± 338.38	0.73 ± 338.77
		24-Jun-16	564.0810	8x4x206	522.6965	1.195	11972	ND	-3.56 ± 124.79	-0.24 ± 124.94
HD 183280	10664975	11-Jun-16	551.0712	1x4x1728	526.2097	1.199	5597	ND	-65.0 ± 120.8	-67.1 ± 120.4
		19-Jun-16	558.9841	1x4x1728	524.8147	1.199	5170	ND	228.1 ± 113.9	-86.8 ± 113.8
HD 185115	9775454	14-May-16	523.1233	1x4x519	523.6516	1.195	3671	ND	-15.5 ± 24.7	26.7 ± 24.8
		17-May-16	526.1238	1x4x519	523.1970	1.195	3676	ND	0.1 ± 20.4	10.4 ± 20.4
		18-Jun-16	558.1102	1x4x519	523.1141	1.195	3601	ND	-18.6 ± 22.5	25.4 ± 22.4
HD 187254	8703413	19-Jun-16	559.0547	1x4x1145	531.3430	1.196	1968	ND	0.8 ± 6.3	-4.6 ± 6.3
HD 226284	5473171	9-Jun-16	549.0866	5x4x285	520.7524	1.191	11400	ND	110.14 ± 244.56	170.04 ± 244.96
		16-Jun-16	556.0860	5x4x285	522.4294	1.190	9702	ND	-184.28 ± 355.0	75.38 ± 355.22
		18-Jun-16	558.0266	9x4x285	522.4064	1.190	12722	ND	-53.37 ± 412.01	-133.76 ± 412.01

TABLE 2.2 – Table of key parameter values for the averaged nightly profiles for each of the 12 targets considered in this study. Columns 3 and 4 display the dates the observations were taken, in Gregorian and Mid-Heliocentric Julian Dates respectively. Column 5 shows the exposure time and observing strategy utilised for each target, while columns 6 and 7 provide the mean wavelength and mean Landé factor respectively for each observation. Column 8 provides the mean SNR for the LSD I profiles. The results of the FAP algorithm are shown in column 9, and the longitudinal field measurements taken from the Stokes V (B_l) and N (N_l) profiles are provided in columns 10 and 11 respectively.

Following performing LSD, to improve the SNR further and reduce the impact of potential remnant spurious signals, we performed a weighted average on the observations for each night, in order to generate a mean profile per night which would be used for the remainder of the analysis process. Additionally, a simple linear fitting was performed on the Stokes I profiles, in order to better normalise the LSD profile and smooth out any offset. This normalisation factor was also applied to Stokes V and N. This process will increase accuracy in the magnetic field calculations to come. The mean wavelength and Landé factor, as well as the SNR for each average nightly profile, are visible in columns 5, 6, and 7 of Table 2.2 respectively. The final Stokes I and V profiles are displayed in Fig. 2.2. The N profiles were flat and showed no signs of pulsations, therefore we do not show them in the figure.

4 Results

4.1 Magnetic status and longitudinal field

We calculated the longitudinal field values B_l for the averaged nightly profiles, following the procedure described in Chap. 1 Sec. 5.2. The values are available in column 10 of Table 2.2, along with the values for N_l in column 11, which are calculated from the N profiles by applying the same methods used for calculating B_l from the Stokes V profiles. It is quickly apparent that, taking into account their errors, the values for B_l and N_l are consistent with zero within 2σ in all cases.

However, B_l can be zero even if the star is magnetic, e.g. if the magnetic field is dipolar and seen edge-on. A Stokes V signature is then present but it is symmetrical around the centre of the line, leading to B_l=0. Therefore we applied the FAP algorithm to the averaged nightly profiles for each target, to check for the presence of a magnetic signature. This resulted in no detections in V nor in N for any target.

4.2 Upper limit on undetected fields

As a result of the lack of magnetic detections for all of the targets, we performed modelling in order to determine the maximum dipolar field strength ($B_{\rm pol}$) values of a magnetic field that might have remained hidden in the noise of the data. This process is described in Chap. 1 Sec. 5.4, but refer the reader to Neiner et al. [81] for a more detailed description of the process.

The results of both the initial upper limit calculations, assuming a 90 per cent detection probability, for each individual profile as well as those using the combined power equation above are detailed in Table 2.3. The upper limit of $B_{\rm pol}$ values vary between 5 and ∼1400 G depending on the star.

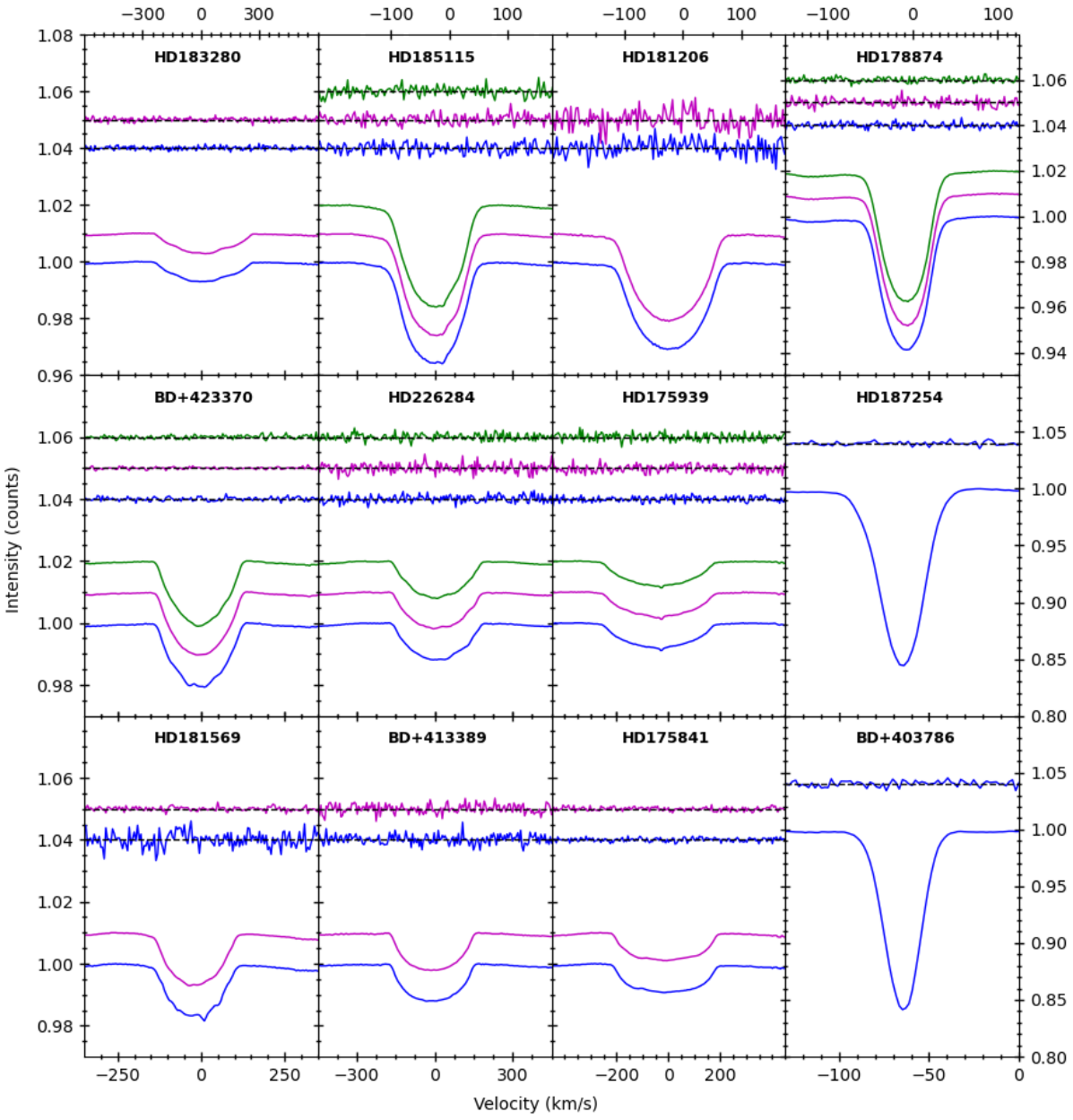

FIGURE 2.2 – Stokes I (lower) and V (upper) profiles for each target star. When they exist, each subsequent night of observation for a particular target is displayed in blue, magenta and green, respectively. Variations in x- or y-ranges along the top and right-hand side apply *only* to the plots immediately adjacent. The Stokes V profiles have been magnified by a factor 30 to improve legibility, and $V/I_c = 0$ is shown by a dashed black line.

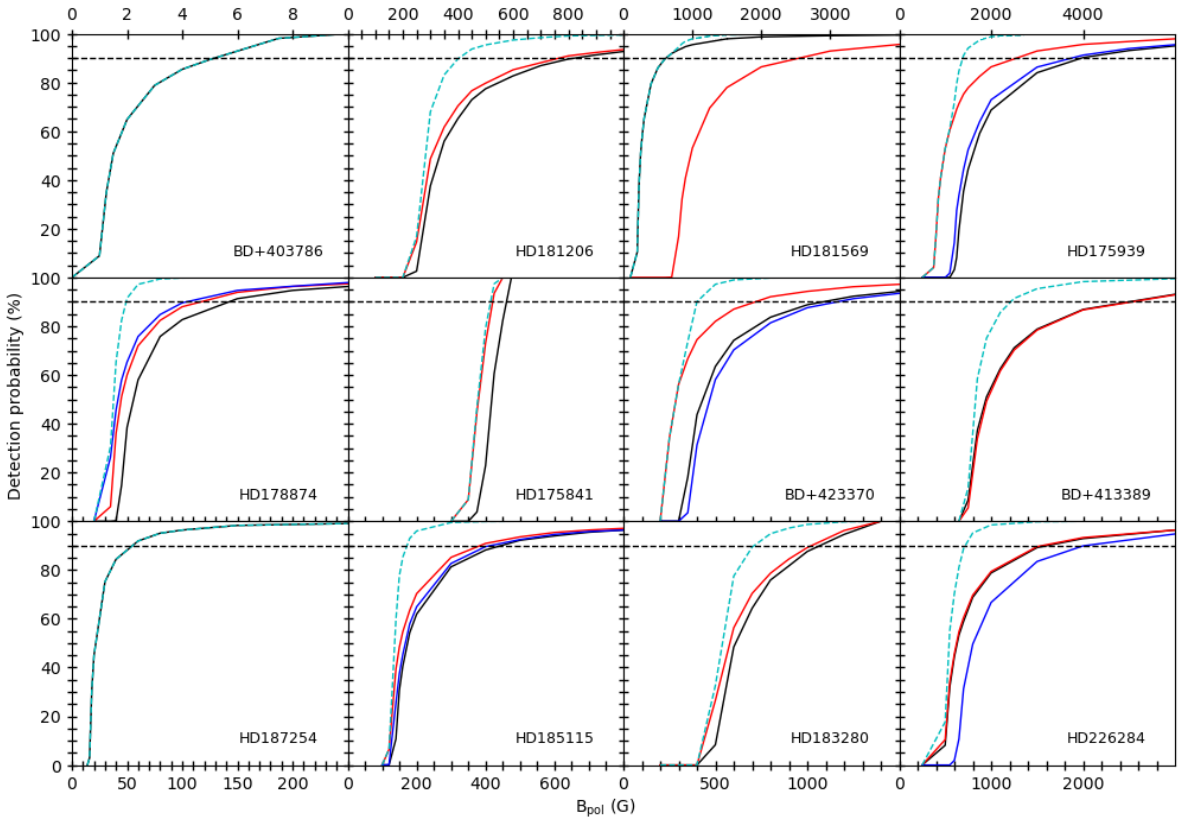

FIGURE 2.3 – Detection probability for the observations of each star as a function of the magnetic polar field strength. The curves represent the first (black), second (red), third (blue) and combined (cyan dashed) profiles. The horizontal black dashed line represents a 90 per cent detection probability. Plots in the same column share an x-axis range, unless stated otherwise above.

Target ID KIC ID	$B_{pol,max}$ (G)	$\widetilde{B}_{pol,max}$ (G)	T_{eff} (K)	$v \sin i$ (km s^{-1})	L (L$_\odot$)
BD +40°3786[a,e] 5965837	5	5	6800 ± 250	15 ± 3	148 ± 15
BD +41°3389[a,b,e] 6289468	2500 2532	1213	8107 ± 70	149.7 ± 7	31 ± 2
BD +42°3370[a,e] 6951642	718 1086 1162	405	7203 ± 250	121 ± 3	35 ± 4
HD 175841[a,c,e] 4989900	421 461	415	8400 ± 150	191.0 ± 15	60 ± 2
HD 175939[b,e] 6756386	2554 3756 4041	1383	7891 ± 62	192.8 ± 11.8	34 ± 2
HD 178874[b,e] 11498638	106 117 143	49	6248 ± 57	39.7 ± 1.2	19 ± 2
HD 181206[a,b,e] 9764965	770 830	406	7478 ± 41	85.1 ± 2.5	8 ± 1
HD 181569[a,d] 3437940	622 2554	622	7700 ± 120	120 ± 5	54 ± 5
HD 183280[a,e] 10664975	1024 1069	713	7892 ± 250	243 ± 10	93 ± 9
HD 185115[a,d] 9775454	385 420 445	172	7050 ± 150	70 ± 5	10 ± 2
HD 187254[e] 8703413	55	55	8000 ± 150	15 ± 2	5 ± 2
HD 226284[a,e] 5473171	1580 1617 2077	719	7784 ± 250	164 ± 5	48 ± 5

TABLE 2.3 – Upper dipolar field strength limit (in G) for both the individual (column 2) and combined (column 3) profiles of each target. The values of effective temperature and luminosity used in the H-R diagram are displayed in columns 4 and 6, respectively. Rotational velocity values are provided in column 5. Superscript indices indicate the origin of the displayed stellar parameters : a) LAMPENS et al. [107], b) TKACHENKO et al. [125], c) TKACHENKO et al. [126], d) CATANZARO et al. [127], e) CATANZARO & RIPEPI [128].

5 Discussion

5.1 General Results

None of the targets observed displayed any significant magnetic signal. Seven of our twelve targets have $T_{\rm eff} \gtrsim 7500$ K. Previous research indicates that about 10 per cent of such stars host a strong magnetic field [70, 129, 130]. Statistically, we should expect to see one of these stars display a magnetic signature. Moreover, our targets were not randomly selected stars, but candidates that were pre-selected as good magnetic candidates from a wider sample through rotational modulation signatures. With this kind of pre-selection, Buysschaert et al. [59] obtained a magnetic detection rate of ∼70 per cent in late-B to mid-A-type stars (which displayed relatively simple lightcurves dominated by rotation with some showing additional low-amplitude signals possibly due to pulsation), and we should then expect ∼5 magnetic detections in our sample of seven stars with $T_{\rm eff} \geq 7500$ K. The non-detection of a field in any of our targets is thus a significant null result.

Moreover, magnetic OBA stars typically have a magnetic field strength of the order of 3 kG, though it can range between 300 G and 30 kG [e.g. 11]. From the results of the upper limits modelling for the seven targets with $T_{\rm eff} \geq 7500$ K, we can see that all seven stars have upper limits below 3 kG and six of the seven stars have upper limits around 700 G or smaller. If the magnetic field of (hotter) δ Sct stars were the fossil fields observed in 10 per cent of OBA stars, we should have detected them in some of our targets.

Therefore, either our sample displays a frequency of magnetic field representation lower than the average 10 per cent of OBA stars or, if a magnetic field is present in these stars, its strength is well below the average field for OBA stars.

Five of our twelve targets have $T_{\rm eff} \lesssim 7500$ K. The three discoveries of magnetic δ Sct stars with $T_{\rm eff} \lesssim 7500$ K so far have fields that are not strongly dipolar but instead are complex fossil, dynamo, or ultra-weak fields with strength between ∼1 and ∼1000 G. For our four cooler targets (BD+40°3786, BD+42°3370, HD 178874, HD 185115), our respective upper limits of 5, 405, 49, 172 G (Table 2.3) are quite good, especially for BD+40°3786 and HD 178874. Statistics is difficult on only four targets, but the fact that we did not detect any field while these four targets were carefully pre-selected as magnetic candidates is still intriguing.

In the following subsections we investigate why the targets in our sample may not be magnetic.

5.2 Stellar evolution

A possible factor that we considered is what impact the evolutionary stage of these stars might have on their potential magnetic field strength. Indeed, in the case of fossil fields, considering magnetic flux conservation, older, more evolved stars must have weaker fields at their surface than their younger counterparts [42]. Moreover, Shultz et al. [11], Bagnulo et al. [12], Landstreet et al. [13, 14] et Fossati et al. [131] showed that an additional intrinsic decay of the field strength may occur. For cooler stars as well, more evolved stars have typically weaker magnetic field strengths [e.g. 132] than their progenitors.

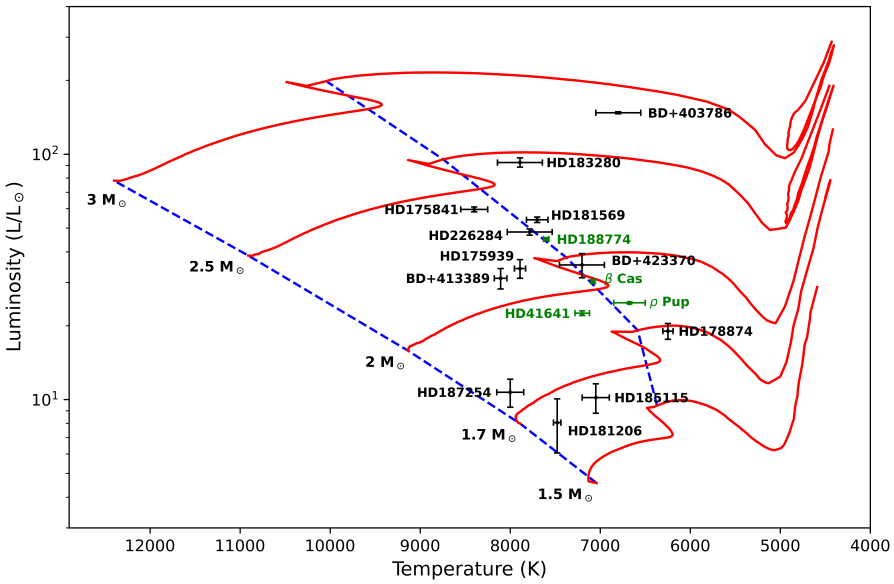

FIGURE 2.4 – Evolutionary tracks of model stars with Sun-like metallicity and rotation, and masses of 1.5, 1.7, 2.0, 2.5 and 3 $M_{\odot}$ respectively. Blue dashed lines correspond to the ZAMS and TAMS. Black dots represent this sample and green dots represent confirmed magnetic δ Sct stars, with datapoints labelled accordingly.

To test this factor, we generated a set of evolutionary tracks for stars with Sun-like metallicity ($Z = 0.014$) and rotation ($V/V_c = 0.4$), shown in Fig. 2.4, using models from the Université de Genève database and detailed in EKSTRÖM et al. [133], over which we plotted the stars from our sample. The values for effective temperature $T_{\rm eff}$ and luminosity L for our targets and their respective errors were taken from an array of surveys [107, 125-128, 134] and are displayed in columns 4 and 5 of Table 2.3. Where unavailable, we determined them using the following equation, valid in the intervals $3.2 < \log g < 4.7$; $3.690 < \log T_{\rm eff} < 3.934$, as determined by CATANZARO & RIPEPI [128] :

$$\log L/L_{\odot} = (-15.46 \pm 0.34) + (5.185 \pm 0.08) \log T_{\rm eff} - (0.913 \pm 0.014) \log g \qquad (2.1)$$

To more easily identify the evolutionary stage, the blue dashed lines visible in Fig. 2.4 were generated, representing the *Zero Age Main Sequence* (ZAMS) and *Terminal Age Main Sequence* (TAMS). The ZAMS was determined from the initial values of the models, which corresponded well with a classical mass-luminosity relation for the given parameters, and the TAMS was set to determine the time at which the mass fraction of hydrogen in the core was lower than $X_c(H) = 10^{-5}$.

Over the next few subsections, we detail the results for the various stars in the sample, ordered by evolutionary stage, and draw individual conclusions.

5.2.1 Main sequence stars

In Fig. 2.4, the following stars are squarely located within the main sequence (MS). We consider BD+41°3389, HD 175841, HD 175939, HD 181206, HD 187254, and HD 185115. The LSD+FAP method provided no magnetic field detection for these targets, and we determined maximum field strengths at 90 per cent probability of 1213, 415, 1383, 406, 55, and 172 G respectively from the upper limits algorithm. Except for HD 185115, the other five stars have $T_{\rm eff} \sim 7500$ K or more. A typical fossil field is thus expected in a few of those targets but not detected, in spite of the very good upper limit for at least three targets. For HD 185115, the upper limit of 172 G is probably not sufficient if the field of this cooler star is a dynamo field.

5.2.2 Terminal age main sequence stars

We consider here stars that are located at the end of the MS or the very beginning of the red giant branch (RGB) in Fig. 2.4. Here we consider BD+42°3370, HD 181569, and HD 226284, with respective maximum field strengths with 90 per cent probability of 405, 622, and 719 G, from the upper limits algorithm. Once again, there were no detections for any of these stars through the LSD+FAP methods, although the upper limit values around 600-700 G for the two hotter stars (HD 181569 and HD 226284) are quite good with respect to the expected fossil field strength.

For the cooler star BD+42°3370, Samadi-Ghadim, Lampens & Gizon [118] performed a specific analysis of the *Kepler* lightcurve with the goal of determining the nature of the dominant frequencies, such as those presented in Fig. 2.1. They used the *Kepler* and *TESS* lightcurves to measure the magnetic activity index $S_{\rm ph}$ (adopting a stellar rotation frequency of 0.721 c/d), and found $S_{\rm ph}$ to vary with a cycle of length ~ 3.2 yr, which they attributed to a possible signature of long-term stellar activity, and discussed their results in light of the presented spectropolarimetric measurements. Despite the fact that this star does not present Zeeman signatures that might indicate the presence of a magnetic field, and taking into account the upper limits value we acquired in this study, they could not rule out the possibility of a magnetic field being responsible for some of the frequencies observed arguing that, because the star had been observed spectrophotometrically in a state of low activity, the magnetic field could be under-represented. In any case, our upper limit of 405 G for this star is probably not sufficient to detect a dynamo field.

5.2.3 Red giant branch stars

Finally, some stars are evolved, progressing along the RGB. We consider BD+40°3786, HD 178874, and HD 183280 to be at this stage of their life cycles, and we found values of 5, 49, and 713 G (Table 2.3) respectively from the upper limits algorithm, and no magnetic field detections through the LSD+FAP method for these stars. For BD+40°3786, our excellent upper limit allows us to conclude that the magnetic field is either ultra-weak (as in the case of ρ Pup) or nonexistent. For HD 178874 a weak dynamo field, similar to the one of β Cas, could have remained hidden in this evolved cooler star. On the other hand, the upper limit for HD 183280

is quite high for an evolved hot star, it is therefore not surprising that we did not detect a field in this target. However, the value found for its rotational velocity ($v \sin i \approx 243$ km s^{-1}) is unusually high for a star on the RGB, therefore this star might be less evolved than found here and the magnetic field should have been detected if the star is on the MS.

5.2.4 Evolution study summary

From this evolution study, we thus conclude that we can explain the absence of detection of a magnetic field in at least two stars (BD +42°3370, HD 178874), and possibly in HD 183280, but not in the other targets.

5.3 Re-examining *Kepler* data in light of the magnetic non-detections

5.3.1 Case-by-case discussion

Considering the results of magnetic non-detections for this sample, it is worthwhile to re-examine the *Kepler* data. This is briefly done here in the same order as in Fig. 2.1. We recall that the presence of a set of harmonic frequencies points to rotation and thus to a magnetic candidate. When two sets of harmonics are present, it may suggest rotation from two different stars (in a binary or multiple system).

BD+40° 3786 = KIC 5965837 : No harmonic series were found. The *Kepler* signals seem consistent with δ Sct pulsation, but with relatively low frequencies. The strongest signals are at 4.05 d^{-1} and 3.39 d^{-1}. This star was determined by Lampens et al. [107] to be a ρ Pup star. In this case it may host an ultra-weak field. When comparing the magnetic analysis of ρ Pup itself with our upper-limit calculation for BD+40 3786 this seems consistent, though such an ultra-weak field could have remained undetected even with the very low upper field limit we achieved here.

BD+41° 3389 = KIC 6289468 : There are two sets of harmonics, one with a fundamental frequency of 1.6290 d^{-1} and the other at 1.551 d^{-1}, the former being significantly stronger. There are many additional low-frequency signals unrelated to the two harmonic series, and which also do not resemble typical γ Dor pulsations. For instance, there is a 'comb' of frequencies centred near 1 d^{-1} which are split almost, but not exactly, evenly by ∼0.09 – 0.1 d^{-1}. There are δ Sct frequencies out to ∼31 d^{-1}.

BD+42° 3370 = KIC 6951642 : There are two sets of harmonics, one with a fundamental frequency of 0.7288 d^{-1} and the other at 0.8008 d^{-1}. However, the peak of the former is broad and it is unclear if it forms a genuine harmonic series. There are two wide and richly-populated groups of δ Sct frequencies centred near 15 d^{-1} (stronger) and 30 d^{-1} (weaker). This star also has at least one combination frequency, where a low frequency signal (2.08 d^{-1}) is equal to the difference between two higher frequency modes (16.44 d^{-1} and 13.48 d^{-1}). Another long-period binary [107], the frequency analysis of BD+42°3370 likely exhibits frequencies originating from both stars. Indeed, we observe two distinct sets of harmonics in the periodograms of Fig. 2.1. Therefore, while the rotational variation hints at dynamo field-like features, it is not guaranteed the field and pulsations are on the same target.

HD 175841 = KIC 4989900 : There are no harmonic pairs, and thus no candidate rotation frequency was identified. The most prominent low-frequency feature is a group of signals centred near 2.2 d^{-1} which could be consistent with γ Dor pulsation. The strongest δ Sct signals are at 6.17 d^{-1}, 8.05 d^{-1}, and 8.21 d^{-1}, but signals extend out to ∼15 d^{-1}. Without clear rotational variation, this star may indeed not be magnetic.

HD 175939 = KIC 6756386 : There are two sets of harmonics. The higher amplitude sequence has a fundamental frequency of 1.7655 d^{-1}, and the other 1.620 d^{-1}, with both having a first and second harmonic. The frequency spectrum is highly populated, with signals out to 50 d^{-1}. There is a group of at least four frequencies centred near 5 d^{-1} with near-equal spacing of ∼0.15 to 0.17 d^{-1}. HD 175939 has been determined to be a long-period binary [107], and we do observe two sets of harmonics in the frequency analysis, so it is difficult to determine which frequencies originate from which star. Nevertheless, the presence of these sets of harmonics points towards rotational modulation.

HD 178874 = KIC 11498538 : The only feature in the periodogram is a harmonic series with a fundamental frequency of 0.29982 d^{-1}, extending to the third harmonic (but the fundamental and first harmonic have significantly higher amplitude). The SC data reveal rapid variations with a timescale of ∼1 hour. However, these do not appear as peaks in the periodogram and thus are not coherent δ Sct modes. These may be solar-like oscillations but which are not easily measurable due to the short baseline of the SC data and/or too high of a noise floor. Between rotational variation found in its frequency analysis and cooler surface temperatures ensuring a convective envelope, HD 178874 presents all the features of a dynamo field. However, our 49 G upper limit value is probably not low enough to detect it.

HD 181206 = KIC 9764965 : There is one harmonic series with the fundamental frequency at 2.051 d^{-1}. There are a few non-harmonic low frequencies. There are not many δ Sct frequencies, but compared to the rest of the sample they are relatively high. The temperature of this star puts it at the limit between dynamo and fossil field types. The upper limit value of 406 G is too high to detect a dynamo field, but would be sufficient to detect a typical fossil field. However, we remark that HD 181206 has been classified as a metal-lined star (with spectral type Am(p)) by Bertaud [135]. All Am stars studied with sufficiently deep spectropolarimetric measurements show a magnetic field but with a typical strength of only a few Gauss [22]. The strongest field has been detected in the Am star Alhena with 30 G [23]. Our observations would not allow to detect such a weak or ultra-weak field.

HD 181569 = KIC 3437940 : The best candidate rotation frequency is at 0.8659 d^{-1}, with a first harmonic and a signal close to, but not exactly at, its second harmonic. There are multiple peaks with amplitudes of ∼200 ppm which bear no relation to the 0.8659 d^{-1} signal. These signals do not obviously resemble the typical patterns of γ Dor pulsation, and thus the type of pulsation they represent (γ Dor vs. δ Sct) is unclear. Signals are found out to ∼19 d^{-1}, with the strongest modes at 10.48 d^{-1}, 10.33 d^{-1}, and 12.02 d^{-1}.

HD 183280 = KIC 10664975 : There are two sets of harmonics. The stronger has a fundamental frequency of 1.2602 d^{-1} and the series extends until at least the sixth harmonic (perhaps suggesting a blended eclipsing binary is responsible). The weaker fundamental frequency of

1.1892 d^{-1} has only a first harmonic. There are low frequency signals unrelated to these two series. At least one of these, at 2.5735 d^{-1} corresponds to the difference between higher frequency δ Sct modes (19.8726 d^{-1} − 17.2992 d^{-1}, and 21.132 d^{-1} − 18.5590 d^{-1}), suggesting mode coupling within the star.

HD 185115 = KIC 9775454 : There do not seem to be any harmonic relations among the many low-frequency signals. However, there are two wide frequency groups centred near 1.5 d^{-1} and 3 d^{-1}, which could be consistent with γ Dor pulsation. Relatively higher amplitude peaks are evident at 4.1602 d^{-1} and 4.6105 d^{-1}, and a signal is seen at their difference (0.450 d^{-1}), suggesting some degree of mode coupling in the star. HD 185115 is the third long-period binary found in this sample [107, 109], with an orbital period of 1707 days, though this one does not present rotational variation observed in the previous two. It is thus unlikely to be magnetic.

HD 187254 = KIC 8703413 : The only feature in the periodogram is a harmonic series with a fundamental frequency of 0.1464 d^{-1}, extending to the third harmonic (but the fundamental and first harmonic have significantly higher amplitude). We see no sign of pulsation. The SC data shows a flare lasting for ∼12 minutes and an amplitude of ∼600 ppm. Flares were not seen in any other star in the sample, but given their short duration their detection is only possible with SC data. Flares are often good indicators of dynamo fields, however with a surface temperature around 8000 K it is unlikely that this is the case here. Instead, it is more likely that the flare originates from an unseen companion, as described for similar stars by Pedersen et al. [136]. HD 187254 is an Am star with a metal-rich surface composition ([Fe/H]=0.254) and according to Balona et al. [137] its *Kepler* lightcurve shows travelling features that could be caused by spots. Like for HD 181206, only weak and ultra-weak fields have been measured in Am stars, so our low upper limit value of 55 G might not be sufficient to detect such a field.

HD 226284 = KIC 5473171 : There are two sets of harmonics, one with a fundamental frequency of 1.405 $^{-1}$ (with one harmonics), and the other at 0.971 $^{-1}$ (with two harmonics). Their amplitudes are similar and it is difficult to determine which set is more likely to correspond to rotation of the δ Sct star. There are many low-frequency signals unrelated to these harmonic series, which then are likely to be pulsational. However, there are no clear patterns to aid in their identification without a more detailed analysis. δ Sct pulsation extends out to ∼18 d^{-1}, and the dominant signal is at 7.57 d^{-1}. There may be a combination frequency between a low-frequency signal at 0.266 d^{-1} and two higher-frequency signals at 14.402 d^{-1}, 14.136 d^{-1} (i.e. their difference is the low frequency). Such combinations have been seen in other δ Sct stars, and suggests that all of these pulsation frequencies exist in the same star and may be due to non-linear interaction.

5.4 Rapid non-periodic variations in short cadence data

The two stars without δ Sct pulsation, HD 187254 (KIC 8703413) and HD 178874 (KIC 11498538), nonetheless showed their own types of rapid variation. In HD 187254 (Fig. 2.5), one flare was observed in the single available short cadence timeseries, which may be an event associated with a lower-mass companion (see Sec. 5.3.1). In HD 178874, fast oscillations are seen throughout the entirety of the short cadence light curves with timescales of roughly one hour (in

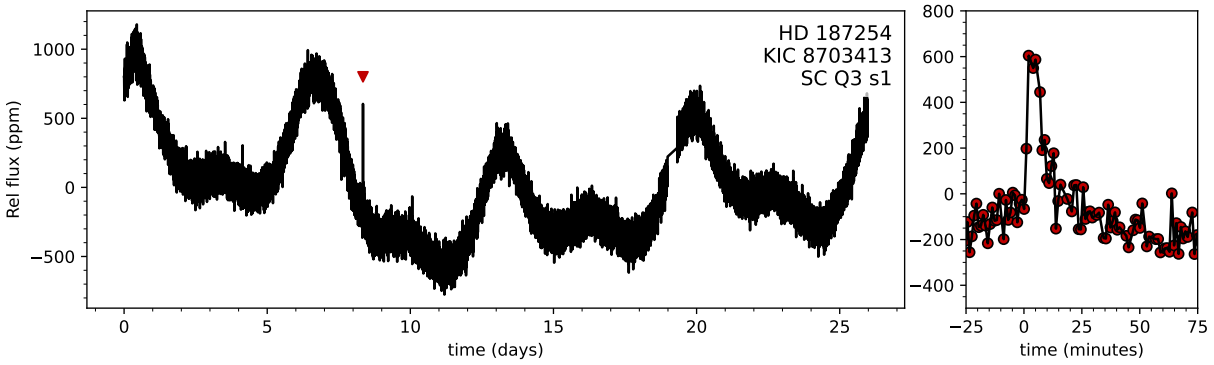

FIGURE 2.5 – Short cadence *Kepler* light curve for HD 187254 = KIC 8703413. The left panel shows the entire light curve, with the red triangle indicating the flare. The right panel zooms in on the flare.

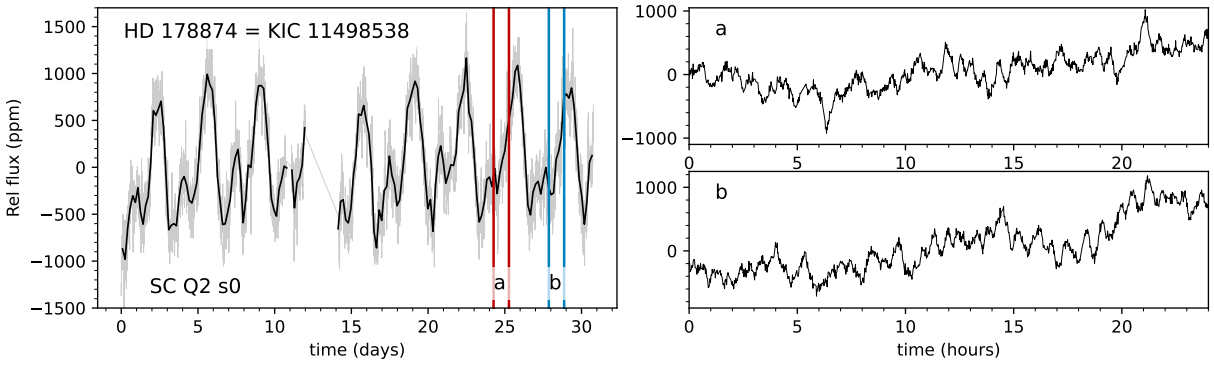

FIGURE 2.6 – Short cadence *Kepler* light curve for HD 178874 = KIC 11498538. The left panel shows the entire light curve in lighter grey, with a solid black line plotting the data with four hour bins (to average over the faster variations). Two pairs of vertical lines mark two 1-day sections. The right panels zoom in on these two 24-hour windows, showing the rapid but incoherent oscillations that take place on a timescale of approximately one hour. The selected short observing windows are arbitrary – similar variations are seen throughout the full time series.

addition to the much slower rotational variability, Fig. 2.6). As mentioned in Sec. 5.3.1, these features do not appear in the frequency spectrum, nor do they appear coherent in the light curve (right panels of Fig. 2.6).

5.4.1 Results of case-by-case study

From the above analysis, we conclude that we can explain the absence of detection of a magnetic field in an additional five stars : BD +40°3786, HD 175841 and HD 185115 which show no rotational modulation, HD 181206 and HD 187254 which are Am stars.

It should also be noted that of our list of 12 potentially hybrid candidates, only three appear to display frequencies typical of both δ Sct and γ Dor variable stars and thus may be genuine hybrids : BD+40°3786, HD 175841 and HD 185115. Once again, the latter is a confirmed binary, so care should be taken when drawing conclusions regarding the frequencies of this star.

6 Conclusions

Although our sample is statistically small and our data likely do not have a sufficient SNR to detect dynamo fields in the four coolest stars of our sample, at least some magnetic stars should have been detected among the eight hottest targets of our sample, considering that we pre-selected them based on the possible existence of a rotational modulation signal. If the chances of magnetic field detection using rotational modulation as a prior is valid (following the work by Buysschaert et al. [59]), then the fact that no field was detected with good upper limits amongst the hot stars in our sample is a significant result.

From our case-by-case analysis in the previous section, we can find a plausible explanation for the non-detection of a magnetic field in seven out of twelve targets. Either these stars show no rotational modulation, or our observations lead to a too high upper field limit with respect to the field strength expected from the evolutionary status, chemical peculiarity (Am), or temperature of the star (cool stars with dynamo fields).

For the remaining few stars (BD +41°3389, HD 175939, HD 181569, HD 226284, and possibly HD 183280), we observe rotational modulation in their *Kepler* data and the upper limits we derive are low enough (622 to 1213 G) to detect a fossil magnetic field in these hotter ($T_{\rm eff}$ = 7700-8107 K) targets. All five stars are confirmed δ Sct variables from our analysis.

It is possible that we overestimated the probability of detecting a field in this sample, that the chance of these stars hosting a magnetic field is not more than 10 per cent, and due to the low statistics we were unlucky with the targets chosen for this study. However, if the chances of magnetic field detection using rotational modulation as a prior is valid (following the work by Buysschaert et al. [59]), then we should have expected to detect a magnetic field in at least some of these five stars.

There are two possible explanations for the dearth of magnetic fields in these remaining five stars :

- either the low frequencies observed in the lightcurves of these hybrid candidates are not due to rotational modulation associated to the presence of a magnetic field. They could be related to binarity, e.g. ellipsoidal variation or tidally excited g-modes. Alternatively, they could be due to the presence of Rossby-modes that are related to the rotational frequency as found in several γ Dor stars [138-140]. There could also be a γ Dor companion associated to the δ Sct star. However, HD 175939, HD 185115 and BD+42°3370 are the only three targets of our sample for which (long-period) binarity was found and this explanation does thus not seem adequate for all five stars.
- or the magnetic fields of hot δ Sct stars are typically weaker (and possibly more complex) than the dipolar fossil fields of OBA stars. This explanation seems plausible considering that the magnetic δ Sct stars discovered so far all have fields below ∼1 kG (see Table 2.1). This could be demonstrated by acquiring deeper spectropolarimetric observations of the five hotter targets listed above or of other bright, low $v \sin i$, δ Sct stars. Since *TESS* observed brighter targets than *Kepler*, including many δ Sct stars, good candidates for a search for weak fields in δ Sct stars are now available and will be the targets of the MOBSTER

collaboration [96, 141]. If weaker fields were confirmed in δ Sct stars, they would provide important constraints to stellar models, in particular to the interplay between magnetism, rapid rotation, and pulsations. If these stars are indeed found not to be magnetic even with deeper spectropolarimetric observations, this begs the question of the origin of this discrepancy with normal OBA stars and hotter pulsators [142].

Chapter 3

Magnetism in LAMOST CP stars observed by TESS

Objectives

The identification of new magnetic hot stars is necessary to progress in the study of magnetism. Especially, there is a dearth of known magnetic pulsating stars, while these targets would allow us to perform magneto-asteroseismology and gain important insight into stellar structure and evolution. A thousand new magnetic candidate CP stars have been identified with LAMOST, among which ∼700 prime targets have rotational modulation determined from *TESS*. We aim to check for the presence of a magnetic field in a subsample of these LAMOST CP stars, test the viability of the 5200 Å depression used to select the mCP candidates in the LAMOST survey as a reliable indicator of magnetism, and expand on the limited database of known magnetic hot stars. The sample includes some pulsators that would be valuable targets for magneto-asteroseismology if their magnetic field is confirmed. We selected ∼100 magnetic candidate LAMOST CP stars, presenting a depression at 5200 Å in their spectrum and that also display rotational modulation in their *TESS* photometric lightcurves. We obtained spectropolarimetric observations of 39 targets from this sample with ESPaDOnS at CFHT. We utilise the Least Squares Deconvolution method to generate the mean profile of the Stokes V and I parameters, from which the longitudinal magnetic field strength for each target can be determined. For HD 49198, we performed more in-depth analysis to determine the polar magnetic field strength and configuration. We detect fields in at least 36 of our sample of 39 targets, with the remaining three either not having sufficiently high SNR to accurately determine the existence of a field, or having other issues that prevented their characterisation. This success rate in detecting magnetic field (above 92%) is very high compared to the occurrence of magnetic fields in hot stars (∼10%). Four of these newly discovered magnetic stars are magnetic pulsators. In particular, we detect the strongest field around a δ Scuti star discovered to date : a 12 kG dipolar field in HD 49198. From our analysis, we conclude that using the 5200 Å depression displayed in the spectra in combination with rotational modulation in photometric data is a very reliable method for identifying magnetic candidates in this population of stars.

Work based on Thomson-Paressant et al., A&A, **689**, A208, p11 (2024) [143]

Contents

1 Introduction

Chemically peculiar (CP) stars are typically main sequence stars that present atypical abundances of certain chemical elements in their surface layers. There are a number of different CP classes, depending on what features they display and what over- or under-abundances they display in their spectra (Ap/Bp, He-strong, He-weak, HgMn, Si, etc. [see 144]). It is believed that these chemical peculiarities appear after the formation of the star, as part of its evolution, due to processes such as atomic diffusion or magnetic effects, which dredge chemical elements up to the surface layers or settle in the interior [145, 146]. CP stars account for approximately 10% of main sequence intermediate mass stars between early-F and early-B [147-150], and a further 10% of OBA main sequence stars present a strong, large-scale magnetic field [151-153]. These two subsets have a significant overlap, corresponding to magnetic CP (mCP) stars with field strengths ranging from $\sim$0.1$-$30 kG [154, 155], mainly of the Ap/Bp-type.

These mCP stars are key observation targets for several reasons. The mechanisms at the origin of their chemical peculiarity (i.e. atomic diffusion, magnetic fields, rotation, and their combinations) are in and of themselves interesting phenomena to study to garner a better understanding of stellar physics and stellar evolution. In addition, their complex atmospheres are great examples upon which we can test and evaluate the validity of atmospheric models, and the variability in their lightcurves due to chemical spots allows for the precise determination of their rotation periods, a benefit that is essential for the study of stellar magnetism [156].

Pulsating stars along the instability strips on the Hertzsprung-Russell (H-R) diagram (e.g. δ Scuti, γ Doradus, β Cephei, etc.) can also display chemical peculiarities and, since this is typically a good indicator of magnetism, these candidates are very appealing targets for magneto-asteroseismology. Pulsating stars allow us to probe their stellar interiors and physical processes, thus they provide key insight into how stars in general form and evolve throughout the H-R diagram [157]. Coupling this pulsational information with knowledge of the magnetic field structure for these stars puts strong constraints on seismic models.

Through the magnetic analysis of CP stars presented in this paper, we aim to expand the list of known mCP stars and prove the validity of using the 5200 Å depression for inferring magnetism within this family of stars. This is particularly valuable for the subset of pulsating variable stars contained within this sample, as the number of confirmed magnetic pulsators is very limited. In addition, a detailed magnetic analysis is performed for one of the target. In-depth analysis of these stars will allow for the constraining of magneto-asteroseismic models, which in turn will provide a better understanding of the influence magnetic fields have on the internal structure of stars and a way to probe the magnetic field inside the star.

2 Target Selection

The *Large Sky Area Multi-Object Fibre Spectroscopic Telescope* (LAMOST) [158, 159], operating at the Xinglong Station in China, was designed to perform a spectroscopic survey of 10 million stars in the Milky Way, as well as millions in other galaxies. Since its first data release in June 2013, it has released additional data sets each year, and has recently surpassed its scientific

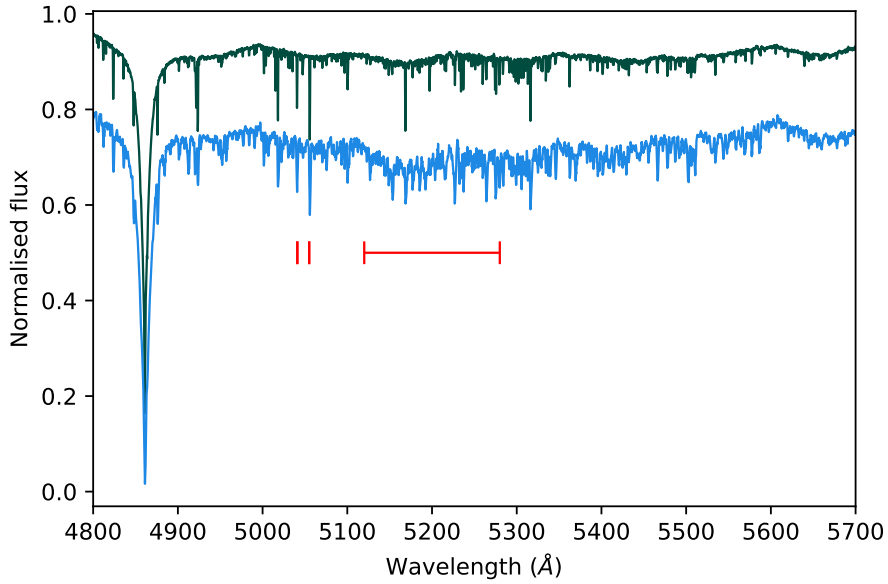

FIGURE 3.1 – Visualisation of the 5200 Å region (red bar) for non-CP star HD 220575 (top), and of confirmed mCP star HD 212714 (bottom). Both stars have a similar spectral type (B8) and their spectra were both taken with the ESPaDOnS instrument. The characteristic Si II lines at 5041 and 5055 Å are also indicated (red tick-marks).

goals.

From the initial LAMOST survey, containing some 4 million stars, a sub-sample of 1002 candidate mCP stars was determined by HÜMMERICH, PAUNZEN & BERNHARD [160]. This was done by selecting all targets that contained a depression at 5200 Å in the LAMOST DR4 spectra of early-type stars (see Fig. 3.1). This depression at 5200 Å, along with ones at 1400, 1750, 2750, 4100 and 6300 Å, have been determined to be uniquely characteristic of mCP stars [161-165]. In particular, it was found that Fe is the primary contributor to the 5200 Å depression, and that the latter is present for the whole range of effective temperatures in mCP stars, making it a fantastic indicator of magnetism in these stars. All the stars in this subset are between 100 Myr and 1 Gyr old, with masses between 2-3 $M_{\odot}$.

This subset was then cross-checked with photometry from *TESS* [89] to look for variability in their lightcurves, and determine stellar parameters such as rotation period and pulsation frequencies [166]. Through this analysis, they determined the rotation periods for 720 mCP stars, including 25 showing signals consistent with pulsation.

From here, stars that had $m_V \lesssim 10$, $v \sin i \lesssim 100$ km s^{-1}, required <6 hours of observation time with CFHT/ESPaDOnS to achieve a theoretical magnetic field detection threshold of 300 G *and* displayed rotational modulation in their photometric lightcurves were maintained in the selection. From a list of ∼100 targets, the sample presented here is finally composed of 39 stars suitable for follow-up spectropolarimetric observations to look for magnetic fields [59, 86], with a particular emphasis on those found to display pulsation signatures in the previous step.

3 Spectropolarimetric Observations

The targets of our sample were observed with ESPaDOnS [49]. The observations primarily took place over 4 semesters between 2021 February 23 and 2022 July 18, but with a few additional observations being performed during January 2024. The list of targets and their respective observations are available in Table 3.1. The exposure time used for each target was defined by considering the stellar properties (in particular temperature and $v\sin i$) and assuming that the field possibly present in the targets is at least 300 G. Studies suggest that magnetic OBA stars typically have a magnetic field strength of ∼3 kG, though it can range between ∼300 G and ∼30 kG [e.g. 11]. As a result, the magnetic threshold selected for these observations is expected to be largely sufficient for the overwhelming majority of targets in this sample. In the case of δ Sct stars however, recent studies suggest that the average field strength might be closer to ∼100 G (see Chap. 2 and/or [86]), and that of γ Dor might be lower than that, since definite detections of the latter have yet to be discovered.

Data taken by ESPaDOnS was reduced using the LibreEsprit [66] and Upena [167] pipelines, however we elected to perform continuum normalisation using SpeNT [10]. Spectral line masks were computed using data from VALD3 [67-69] to use as a template, based on the stellar parameters of each respective star, namely $T_{\rm eff}$ and $\log g$. These template masks were fine-tuned by removing regions coinciding with Hydrogen lines, telluric absorption features, and any other features that we considered detrimental to the quality of the spectrum. We then adjusted the line depths of the mask, to better match those found in the stellar spectrum, following the standard procedure described in Grunhut et al. [70]. This is particularly important for CP stars since their line depths differ from those of non-peculiar stars.

We then followed the standard procedure described in Chap. 1 Sec. 5.1 for generating the LSD Stokes profiles presented in Sec. B.

Target	TIC	Spectral Type	Vmag	Date	Mid-HJD +2459000	T_{exp} (N × 4 × s)
BD +00 2099	271310339	kB8hA3mA3CrEu	9.90	23-Feb-21	269.9500	1x4x519
BD +01 1920	271375640	A1III-IVSrSiEu	10.02	07-Jan-24	1318.0421	1x4x206
BD +08 2211	312111544	kA3hA5mA7SiEu	9.81	04-Jan-24	1315.1807	1x4x220
BD +10 2572	404536886	kA3hA7mA9SrCrEu	9.75	21-Feb-21	633.0596	1x4x133
BD +40 4697	305482510	B9III-IVSi	9.75	18-May-21	354.1158	1x4x276
BD +43 3648	188301298	kB9hA0mA2Si	9.57	18-May-21	354.1043	1x4x177
BD +44 767	65643991	kA0hA1mA3(Si)	9.90	25-Nov-21	544.7399	1x4x73
BD +49 1011	428515156	B8IV-VCrSi	9.71	26-Nov-21	545.7688	1x4x128
HD 11140	72150546	B8IVSi	8.56	01-Sept-21	459.9184	1x4x94
HD 14251	292977419	B8IV-V	9.43	30-Aug-21	457.9600	1x4x538
HD 18410	251412475	kB7hA7mA6CrEuSi	9.14	01-Sept-21	459.9253	2x4x67
HD 19846	445923870	B9IV-VEu	8.57	25-Nov-21	544.7592	1x4x359
HD 22961	284084463	A0IV-VSi	9.57	26-Nov-21	545.785	1x4x465
HD 28238	373024953	A2IV-VSrCrEu	9.16	28-Aug-21	456.1498	1x4x24
				26-Nov-21	545.8317	1x4x24
HD 36259	268068786	B8IVSi	9.08	01-Sept-21	460.0312	1x4x878
HD 36955	427377135	kA0hA2mA4CrEu	9.58	01-Sept-21	460.0706	1x4x656
HD 48560	11767386	kA1hA2mA5CrEu	9.60	27-Nov-21	547.0746	1x4x93
HD 49198	16485771	A0III-IVCrSi	9.31	26-Nov-21	545.8924	1x4x319
				27-Nov-21	547.0635	1x4x319
				18-Feb-22	629.9653	1x4x319
				21-Feb-22	632.8058	1x4x319
				22-Feb-22	633.9703	1x4x319
HD 49522	91136550	A0VCrEuSi	8.88	23-Feb-21	269.9116	1x4x316
HD 56514	440829763	A5IV-VSrCrEu	9.36	23-Feb-21	269.9287	1x4x266
HD 63843	35884762	A2IVSrSi	10.25	18-Jan-24	1329.0059	1x4x280
HD 66533	169971995	kB9hA3mA8SrCrEu	9.44	27-Nov-21	547.1427	1x4x32
HD 71047	27256691	A5III-IVSr	9.60	23-Feb-21	269.9804	1x4x299
HD 86170	62815493	kA2hA3mA6SrCrEu	8.41	23-Feb-21	269.9932	1x4x30
HD 108662	393808105	B9VCrEu	5.24	20-May-21	355.9027	2x4x30
				21-May-21	356.8757	1x4x30
HD 177128	120495323	kA1hA4mA6SrCrEu	9.11	18-May-21	353.9324	1x4x100
HD 212714	164282311	B8IVEuSi	8.72	18-Jul-22	779.8864	1x4x1008
HD 232285	240808702	B9VCrEuSi	9.42	30-Aug-21	457.8978	1x4x147
HD 256582	319616512	B5VHeB9	10.01	22-Feb-22	633.8106	2x4x1434
HD 259273	234878810	B9III-IVSi	9.73	25-Dec-21	574.8461	2x4x937
HD 266267	235391838	A9VSrSiEu	10.04	15-Jan-24	1326.0506	1x4x55
HD 266311	237662091	kA1hA3mA6SrCrEu	9.74	23-Feb-21	269.9003	1x4x40
HD 277595	122563793	B8VSi	9.55	01-Sept-21	459.9937	2x4x200
HD 281193	385555521	A4IVCrEuSi	10.08	25-Nov-21	544.7461	1x4x89
TYC 2873-3205-1	384988765	B9.5VSi	9.98	01-Sept-21	459.9566	1x4x546
TYC 3316-892-1	458780077	B9IV-VSi	9.74	25-Nov-21	544.7318	1x4x186
TYC 3319-464-1	117663254	B9.5IV-VCrEu	9.74	01-Sept-21	459.9384	1x4x146
TYC 3733-133-1	252212077	A2IVCrEu	9.66	26-Nov-21	545.8352	1x4x40
TYC 3749-888-1	321832920	A7VSrCrEuSi	9.81	27-Nov-21	545.8406	1x4x73

TABLE 3.1 – Summary of observational parameters for the targets in our sample. Column 3 provides spectral type from HÜMMERICH, PAUNZEN & BERNHARD [160] and column 4 presents apparent V magnitude. Observation dates are provided in two formats in columns 5 and 6, with number of sequences (N) and exposure times in seconds in column 7.

4 Results and discussion

Using the LSD Stokes V and I profiles generated in the previous step, we calculated the longitudinal field values B_l for each target in our sample [71, 72] and also applied the FAP algorithm to verify our results, both described in Chap. 1 Sec 5.2.

From our sample of 39 stars, 36 of them had definite detections (>92% detection rate), and three had no detections. Of these three, one should not have been included in the initial sample (HD 14251, see Sec. 4.1) and the other two (BD +44 767 and HD 281193) have lower SNR values than required for a definite detection of a field of at least 300 G, despite large B_l values, and require additional observations to reach our goal threshold and check for the presence of a magnetic field down to 300 G. These 2 stars could thus also be magnetic but our data are of too poor quality to conclude. If we consider only properly selected targets and good quality data, our detection rate is in fact 100%.

From the determined values for B_l, we can then calculate the polar field strength using the equation adapted from Schwarzschild [79] and following the procedure described in Chap. 1 Sec. 5.3.

However, with only one or two observations available for most of the targets presented here, only a minimum value of $B_{\rm pol}$ can be inferred. This is done by assuming $\cos(i \mp \beta) = 1$ and that $B_l^{\pm}$ is the maximum/minimum amplitude (based on the sign) of the dipolar fit. As such, should additional longitudinal field measurements become available, the resulting $B_{\rm pol}$ can only increase.

The $B_{\rm pol}$ values are presented in Table 3.2. They range from ∼300 G to ∼13 kG, which is typical for mCP stars [see e.g. 11, 150].

In order to establish the SNR required to detect magnetic fields with our desired threshold of 300 G, we require values of $v \sin i$ for each target, most of which lacked individual spectroscopic studies to determine accurate values for this parameter. As such, the observations were performed utilising a $v \sin i$ estimate based on the rotational velocity of the star, determined from the precise rotation period from *TESS* photometric lightcurves, while assuming $\sin i = 1$ and an estimated value for the radius of the star. While this works well as a first approximation, and indeed did not significantly impact the quality of our observations for the vast majority of the targets in our sample, it is not a wholly reliable method. In order to accurately calculate B_l and $B_{\rm pol}$, we elected to determine values for $v \sin i$ ourselves via the Fourier method. This typically operates by performing the Fourier transform of a number well defined and isolated spectral lines, and the position of zeroes present in this Fourier transform provides information on the value of $v \sin i$ [168]. Thanks to the very high resolution spectra provided by ESPaDOnS and to the nature of the LSD method, we have access to a very well-defined mean spectral line profile for each star from which we can apply this technique, resulting in a $v \sin i$ value that is more representative than performing this step on several individual spectral lines. For the few targets that presented individual studies in the literature, the values we find are consistent with those determined in other works [e.g. 169], excluding large scale surveys such as LAMOST where we found that the determined $v \sin i$ were largely inaccurate and unreliable. The results of our findings are

presented in column 5 of Table 3.1.

The results of this study provide many new confirmed magnetic stars that are well suited for additional observations and analysis, and also demonstrate the reliability of using the 5200 Å depression in addition to photometric rotational modulation for identifying magnetic candidates. Although the number of pulsating stars in this preliminary sample is limited, with three δ Sct (HD 36955, HD 49198 and HD 63843) and one SPB (HD 277595), all of them are confirmed magnetic detections. These magnetic discoveries are significant results since the sample size of known magnetic pulsating stars is small. There are two more pulsators in our sample awaiting observations. As mentioned previously, these magnetic pulsating stars are essential for providing better constraints to magneto-asteroseismological models and consequently improving our understanding of stellar interiors.

A number of special cases, including the few targets with ND results from the FAP algorithm, those determined to contain stellar companions, as well as any stars presenting pulsations, are detailed in the sections below.

In the few cases where a binary companion was detected and displayed a distinct LSD Stokes I profile from the primary, i.e. SB2 systems, we checked whether a magnetic field could be detected for the secondary. In all such cases, no magnetic field detection was recorded. For these companions, as well as for the 3 target stars with no field detection listed above, we calculate upper limits of the polar magnetic field strength $B_{\rm pol}$, determining the maximum value of a magnetic field that might have remained hidden in the noise of the data. This technique is described in Chap. 1 Sec. 5.4.

A couple of stars appear to also contain binary companions, namely HD 28238 and HD 49198, determined through the variation in the LSD Stokes I profile in one or multiple observations. These targets are thus identified as SB1 systems. We see additional features and variation in the LSD Stokes I profiles of both HD 212714 and HD 256582, however in this case the nature of the variations are less clear, and since the I profiles of the two components are visually indistinct, it makes performing the previously described analysis difficult. We suggest that these features could be the result of rotational effects, or perhaps also SB2 systems.

4.1 HD 14251 – TIC 292977419

HD 14251 was initially flagged as a doubtful CP star during the initial survey of LAMOST targets in Hümmerich, Paunzen & Bernhard [160] : they noted that the star shows enhanced metal-lines but no traditional Si, Cr, Sr, or Eu peculiarities. Through the analysis of the spectropolarimetric data and the generation of the Stokes profiles seen in Fig. B.2f, we clearly see a double I profile characteristic of a spectroscopic binary SB2 system. Neither of the two stars are found to be magnetic, demonstrated by the lack of signal in the Stokes V profile and the ND result of the FAP algorithm. An upper limit calculation gives values of 2250 and 3000 G at 90% detection probability for the primary and secondary respectively, where for the secondary we used a template mask with an adopted $T_{\rm eff} = 8500$ K (compared to 12,500 K for the primary) and determined $v \sin i = 5.44 \pm 2$ km s^{-1} using the Fourier method centred on the LSD Stokes I profile of the secondary. With these upper field limits, we cannot exclude the possibility that we

missed the existence of a magnetic field. However, our analysis shows that this star is an SB2, which may explain the confusion with a mCP star. It is thus likely that HD 14251 is simply a non-magnetic SB2 system.

4.2 BD+44 767 – TIC 65643991

Despite a clear and narrow LSD Stokes I profile in Fig. B.2c, any signal that could be visible in V is too confounded by noise to be certain, confirmed by the ND result of the FAP algorithm. Upper limit calculations suggest we had a 90% probability of detecting a field at least as strong as 1500 G, should one exist. Observations were planned using a $v \sin i = 7.86$ km s^{-1}, determined from the *TESS* lightcurves, however using the Fourier method in this work we instead determine a value of $v \sin i = 19 \pm 1$ km s^{-1}, which impacts the SNR required to achieve the 300 G magnetic field threshold and would have subsequently required higher exposure times. As a result, the effectiveness of our observations was negatively impacted by an inaccurately determined value of $v \sin i$, further confirmed by the 1500 G upper limit value that we determined. Additional observations with a higher SNR would allow us to confirm or deny the existence of a field in this star.

4.3 HD 281193 – TIC 385555521

This target presented an ND result from the FAP algorithm, in combination with very large error bars in both B_l and N_l. There appears to be a possible hint of signal in V in Fig. B.6f, but it is not statistically significant. Performing upper limit calculations suggests we had a 90% probability of detecting a field at least as strong as 14,500 G, should one exist, which does not provide much of a restriction. HD 281193 is a relatively fast rotator with $v \sin i = 103 \pm 3$ km s^{-1} determined via Fourier analysis. The $v \sin i$ utilised to compute the required SNR for the observations was strongly underestimated which led to the poor quality of our data and high upper limit on the detectable field strength. Unfortunately with such a high $v \sin i$, additional spectropolarimetric observations with enough SNR will be difficult to obtain.

4.4 HD 259273 – TIC 234878810

This target is a known eclipsing binary (EB) with a 3.409 d orbital period [166], however we clearly observe a signal in the Stokes V profile after performing LSD, and acquire a definite detection result from the FAP algorithm. In this case, the magnetic field is clearly aligned on the primary star (as seen in Fig. B.6b). The N profile also shows a signature at the position of the primary component (FAP gives ND and MD respectively for the two sequences), due to the binary radial velocity motion. It is much weaker than in Stokes V and does not put the magnetic detection into question. However, it may affect the exact B_l value determined from the Stokes V profile. Calculating the FAP for the secondary star gives an ND result, and the upper limits algorithm determined a 90% probability of detecting a field with $B_{\rm pol} \geq 307$ G. To achieve this, we once again recalculated the LSD profiles using a template mask with $T_{\rm eff} = 8500$ K for the secondary, and determined $v \sin i = 25 \pm 2$ km s^{-1} from the resulting LSD Stokes I profile using

the Fourier method. For the magnetic primary, we recovered $v \sin i = 5.1 \pm 2$ km s^{-1}, which was considerably slower than anticipated. Additional information for this system is provided in Sec. 4.9.

4.5 HD 277595 – TIC 122563793

Through our spectropolarimetric analysis, HD 277595 has also been identified as an SB2 system, once again demonstrated by the double I profile in the LSD Stokes profiles displayed in Fig. B.6e. In contradiction to the other SB2 HD 14251, however, HD 277595 is a clear mCP star in Hümmerich, Paunzen & Bernhard [160] and this time we clearly see a signal in Stokes V, in the primary star, implying it is magnetic, confirmed by the definite detection via FAP. We determined a value of $B_l = 526.7 \pm 120.6$ G, and the FAP shows a non-detection for the secondary component of the system, confirming the magnetic field is centred on the primary. Calculating an upper limit value for the secondary, using a $T_{\rm eff} = 8500$ K template mask and calculating $v \sin i = 9.42 \pm 1$ km s^{-1} (compared to 12,500 K and 13 ± 1 km s^{-1} for the primary), we determine we had a 90% probability of detecting a field at least as strong as 1866 G in the secondary component.

In addition, SPB pulsations were observed in the *TESS* lightcurves, which appear to coincide with the magnetic primary, especially considering the B8VSi spectral type and the comparatively cool secondary. The primary component of HD 277595 is thus a new magnetic SPB star.

4.6 HD 36955 – TIC 427377135

HD 36955 displays multiple δ Sct pulsations between 30 and 50 d^{-1}, with an additional peak at 18.5 d^{-1} (see Fig. 3.4). Through the analysis of the spectropolarimetric data, we determine a clear magnetic detection, with $B_l = -580.6 \pm 60$ G, corresponding to an approximate polar magnetic field strength of the order of $B_{\rm pol} \gtrsim 1850$ G, assuming a dipolar field structure. HD 36955 is thus a new magnetic δ Sct star.

4.7 HD 63843 – TIC 35884762

We observe δ Sct pulsations in this star with frequencies between 9 and 22 d^{-1} (see Fig. 3.4). As with the previous star, we detect a clear magnetic field with $B_l = 2191.3 \pm 15$ G and, assuming dipolar field structure, $B_{\rm pol} \gtrsim 6600$ G. HD 63843 is thus another new magnetic δ Sct star.

4.8 HD 49198 – TIC 16485771

Amongst our sample of stars, one target in particular received more observations than the others : HD 49198. This was as a result of it being a relatively bright target, displayed clear δ Sct pulsations between about 12 and 38 d^{-1} (see Fig. 3.4), and had a clear well-defined magnetic detection during the first semester, making it a new magnetic δ Sct star and a particularly appealing target for this study. It is also an SB1, as evidenced by the shift in the Stokes I profile seen in Fig. B.4b. The multiple observations allowed us to perform additional analysis for this star, and infer the overall characterisation of the magnetic field.

First, the B_l values we calculated for this star were significantly higher than those for almost any other targets in our sample, with very small error bars. Using these values in combination with the rotational period, inferred by *TESS* photometry, we can visualise the evolution of the longitudinal magnetic field with respect to the rotation of the star, seen in Fig. 3.3. Fitting a simple sinusoidal function to the data points, to approximate the variation of a dipolar field, we see that the fit is extremely representative ($\chi^2 = 0.305$). Such a low χ^2 means we are probably overestimating the error bars on the B_l values. It is therefore safe to assume that the magnetic field of HD 49198 is dipolar in nature, with a strength varying between :

$$\begin{cases} B_l^+ = -785.5 \pm 32.6 \text{ G} \\ B_l^- = -3,212.2 \pm 32.6 \text{ G} \end{cases}$$

Assuming that the field is indeed dipolar, we can derive the polar field strength $B_{\rm pol}$ and the magnetic field obliquity β. First, we need to calculate the inclination of the rotational axis of the star with respect to the line of sight. For this, we follow the method detailed in various other articles [e.g. 95, 170], and described thoroughly in Chap. 1 Sec. 5.3, where we utilise an Oblique Rotator Model first defined by Stibbs [77] to determine a value for i, then for β and $B_{\rm pol}$. We retrieve values from *Gaia* [76] for the effective temperature $T_{\rm eff} = 9839 \pm 220$ K and absolute magnitude $M = 0.72 \pm 0.09$, the value from *TESS* for the rotation period $P_{\rm rot} = 6.2237647$ d, infer the rotational velocity $v \sin i = 14.97 \pm 1$ km s^{-1} using the Fourier method on the LSD Stokes I profile, and utilise the radius-luminosity-temperature relation (Eq. 1.3) to calculate a value for the inclination.

We determine values of $L = 43.92 \pm 3.64$ L$_\odot$, $R = 2.29 \pm 0.14$ R$_\odot$ and $i = 53 \pm 7°$ for the luminosity, radius and inclination respectively. Using this value for i in combination with the ratio between the minimum and maximum longitudinal field values, we can then determine a value for β with respect to the inclination using Eq. 1.4 [78].

In our case, utilising the values for i, B_l^+, and B_l^- defined above, we find $\beta = 155 \pm 5°$. Finally, $B_{\rm pol}$ can be estimated, where we have assumed a limb-darkening coefficient of $u = 0.5044$, determined from Claret [80]. Using the calculated values for i, β, and B_l, we determine $B_{\rm pol} = 11,740 \pm 2700$ G. The error on this value is limited by our precision on the stellar parameters.

In Fig. 3.3 we see that the maximum of the folded lightcurve (top panel) is slightly shifted with respect to the minimum of the longitudinal field curve (bottom panel). This is often observed in chemically peculiar stars where chemical spots are close to but not right at the magnetic pole.

This kind of in-depth analysis is most beneficial when working with numerous exposures, as it allows us to better constrain the polar field strength value and its structure, taking pulsations into account. By acquiring additional observations of this star covering the rotation and pulsation phases, we will be able to perform ZDI [83], allowing us to model and characterise the magnetic field at the surface of the star.

4.9 *TESS* frequency spectra

We revisited the *TESS* data for the four pulsators and one EB of this sample, including more recent data than was presented in Labadie-Bartz et al. [166] whenever available. For the

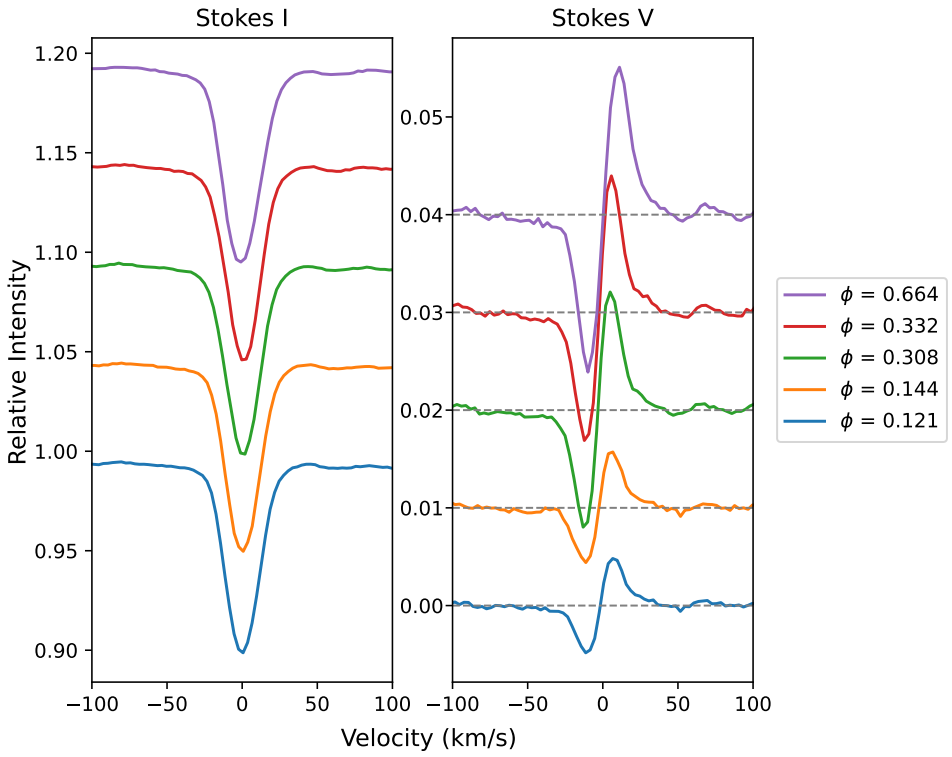

FIGURE 3.2 – Stokes I (left panel) and V (right panel) profiles for HD 49198, ordered with respect to the rotational phase of the star and shifted vertically for clarity. The zero-points for each respective Stokes V profile has been defined by a dashed line.

three δ Sct pulsators, it is important to ensure that the stellar oscillation frequencies are below the Nyquist frequency of the *TESS* photometry. Only one of these, HD 36955 (TIC 427377135), had 2-minute cadence data (from sector 6), so we largely rely on the *Full Frame Image* (FFI). The cadence of the FFIs has increased since the start of the mission, resulting in higher Nyquist frequencies and thus the ability to detect higher frequency signals. In the first two *TESS* cycles (sectors 1 to 26), the FFI cadence was 30 minutes (Nyquist frequency of 24 d^{-1}), in the next two cycles (sectors 27 to 55) the FFI cadence was 10 minutes (Nyquist frequency of 72 d^{-1}), and in cycle 56 and later the FFI cadence was increased to 200 seconds (Nyquist frequency of 216 d^{-1}).

The frequency spectra are plotted in Fig. 3.4, computed using Period04 [110]. First the rotational frequency and any harmonics were removed, and subsequent peaks were identified through iterative pre-whitening and a simultaneous fit of all significant peaks (above a SNR threshold of 4, using a 2 d^{-1} window centred on each signal). Inspection of the highest-cadence *TESS* light curve available for these targets (2-minute cadence for HD 36955, and 200 second cadence for the rest) did not show any significant peaks beyond what is plotted in Fig. 3.4, demonstrating that the 10-minute cadence data do not suffer from super-Nyquist aliasing (although the amplitude of the highest frequency peaks for HD 36955 may be slightly suppressed in the sector 32 data). The frequency spectrum in Fig. 3.4 for HD 49198 supersedes what is shown in LABADIE-BARTZ et al. [166] which relied on 30-minute cadence data (and so did suffer from super-Nyquist aliasing).

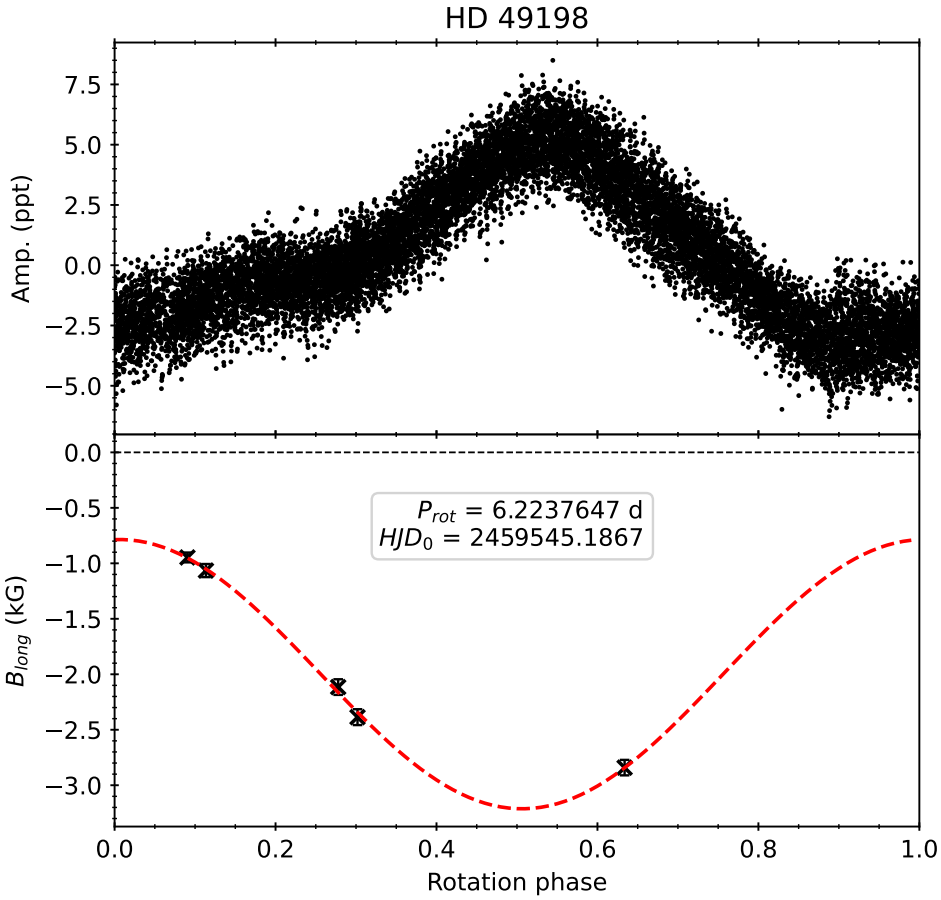

FIGURE 3.3 – *TESS* photometric lightcurve of HD 49198 (top panel), phase-folded with respect to the rotation period, utilising data from all currently available sectors (s20, s60, s73). Longitudinal magnetic field values (bottom panel) for HD 49198 with their respective error bars, phase-folded with respect to the rotation period and overplotted with a simple dipolar fit. The values for the rotation period (P_{rot}) and initial Heliocentric Julian Date (HJD_0) are provided for reference.

HD 277595 : The low-frequency group of signals centred around 1.5 d^{-1} is poorly resolved, and it is unclear as to whether or not there are genuine differences between sectors 19 and 59, or if the perceived differences are due to insufficient frequency resolution. However, the difference in the signals lower than 0.5 d^{-1} do seem genuine. Considering the spectral type (B8VSi), the photometric variations are consistent with SPB pulsation.

HD 49198 : The frequency spectrum is similar when comparing sectors 60 and 73, with some changes in the relative strength of a few signals. The observed behaviour is typical for δ Scuti pulsators.

HD 63843 : There are significant differences in the relative amplitude of signals that are strong in one or both sectors (e.g. at 19.7 d^{-1} and 16.7 d^{-1}). Two higher frequency signals, at 26.5 and 26.8 d^{-1} only appear prominently in sector 61. These signals are typical of δ Scuti pulsators.

HD 36955 : The frequency spectra are similar in sectors 6 and 32 for the high frequency δ

Scuti pulsation, but with some relative changes in amplitude. The lower frequency signals (< 2 d^{-1}) change between sectors and possibly reflect γ Dor pulsation, although this is not entirely clear.

HD 259273 : We re-visited the *TESS* photometry for this eclipsing binary considering the information gleaned from our analysis of the ESPaDOnS data. In Labadie-Bartz et al. [166], the rotation period of the magnetic star was presumed to be the same as that of the orbital period (3.409073 d), due to the unambiguous nature of the eclipses and the coherent out-of-eclipse variability consistent with rotation. However, from the very narrow Stokes I line profile for the magnetic component (Fig. B.6b) we measured $v \sin i = 5.1 \pm 2$ km s^{-1}. Coarsely estimating the radius of the magnetic star to be between 2 and 3 $R_\odot$ (consistent with its late B spectral type), considering the uncertainty on $v \sin i$, and setting $i = 90°$, the rotation period should be between about 14 and 50 days – considerably slower than the orbital period and the out-of-eclipse variability. A more careful extraction of the two sectors of available *TESS* data revealed a slow oscillation with a 15.5 day period, as shown by the red curves in Fig. 3.5, which may be caused by rotation of the magnetic star. Future additional spectropolarimetry can be used to unambiguously determine the rotation period. The secondary is more broad lined with $v \sin i = 5.1 \pm 2$ km s^{-1}, where a radius of 1.5 (2.0) $R_\odot$ and $i = 90°$ corresponds to a rotation period of 3.0 (4.0) d, and thus may be tidally locked.

After subtracting the slow oscillation, the same photometry phased to the orbital period is shown in Fig. 3.6 along with the RV measurements for both components determined from the Stokes I profile (Fig. B.6b), and one RV measurement of the primary (magnetic) star from LAMOST DR8 [171]. Although the RV measurements are sparse, they suggest that the magnetic star is a genuine member of the eclipsing pair (and not, e.g., a further out tertiary), and that it is the hotter component. Since the magnetic star seems to rotate much slower than the orbital period, it is not tidally locked (but the secondary may be). A rotating secondary can only explain the variation if it has surface features that are stable for at least as long as the *TESS* observing baseline ($\sim$2 years). Magnetism can cause such spots, but no magnetic field was detected in the secondary (Sec. 4.4). The out-of-eclipse variation is then perhaps best explained by a reflection effect where the hotter primary irradiates the primary-facing hemisphere of the secondary.

The orbit appears to not be perfectly circular, as the secondary eclipse occurs at 0.510 in phase after the primary eclipse. From the RV semi-amplitudes and the relative eclipse depths, the secondary should be $\sim$0.77 times the mass of the primary, and $\sim$0.9 times the effective temperature of the primary (consistent with an early to mid A star). Further data and analysis are required to properly characterise the stellar and binary properties of this system, but the information presented here provides a useful starting point.

The radial velocity measurements (determined from a Gaussian fit) from the two Stokes I profiles for HD 259273 are 87.56 ± 0.05 km s^{-1} and -119.08 ± 0.5 km s^{-1} for the primary and secondary components, respectively, for the observation taken at MJD = 2459574.846135, and 83.62 ± 0.05 km s^{-1} and -114.99 ± 0.5 km s^{-1} for the observation at MJD = 2459574.892165.

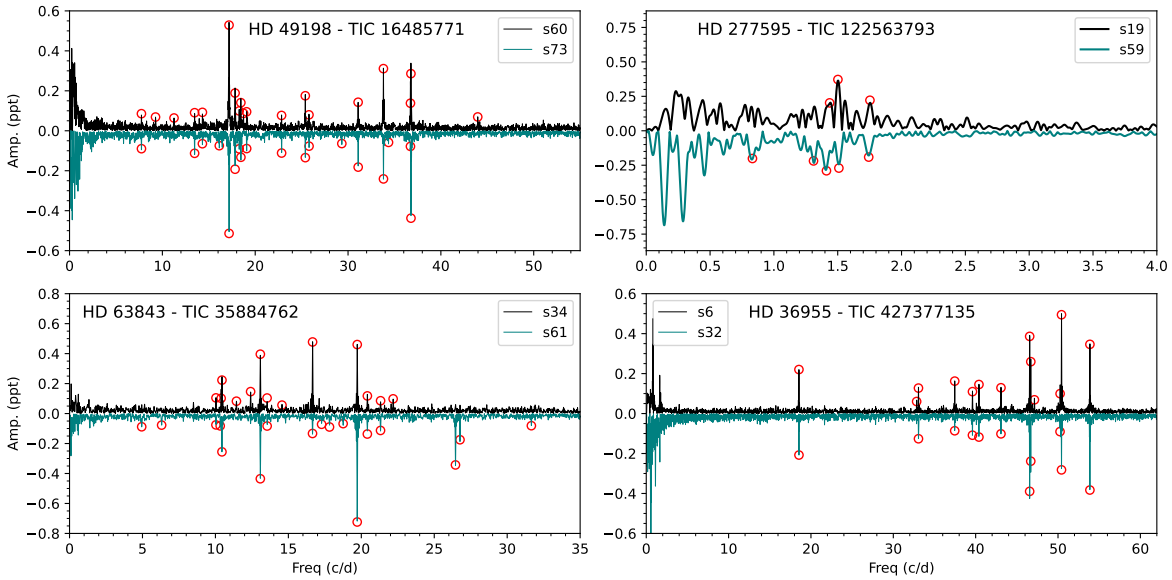

FIGURE 3.4 – *TESS* frequency spectra for the four pulsators after removing the rotational signal (except for HD 63843 which does not show detectable rotational modulation in the *TESS* data), computed from two different sectors of data for each star (the curve for the latter sector is inverted). Individual frequencies are marked with red circles.

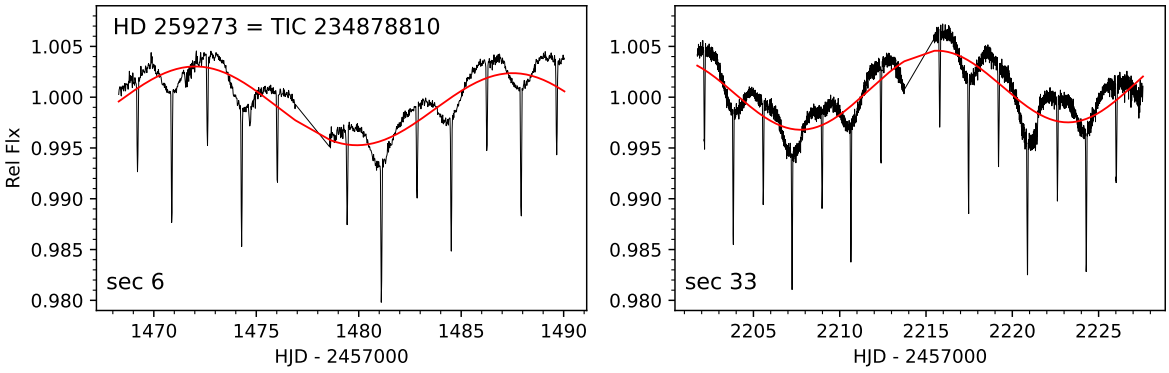

FIGURE 3.5 – *TESS* light curves of HD 259273 from sectors 6 and 33. The red curve shows the 15.5 day signal that is potentially associated with rotation of the magnetic star.

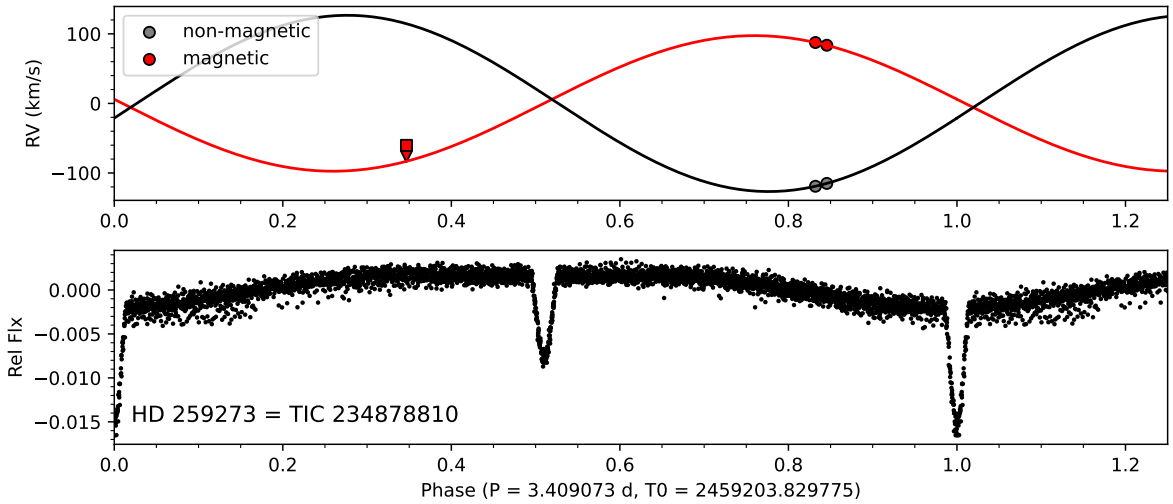

FIGURE 3.6 – *TESS* light curve of HD 259273 (bottom) from sectors 6 and 33, phased to the orbital period, after removing the ∼15.5 day signal. The upper panel shows the RV measurements from the two ESPaDOnS Stokes I spectra shown in Fig. B.6b for both components (red and black circles for the magnetic and non-magnetic stars respectively). The RV measurements from LAMOST are indicated by a red square (for the red arm of the spectrograph) and triangle (for the blue arm). A sinusoid is fit to the ESPaDOnS RVs to give a qualitative impression of the expected RV curves, but is not quantitatively reliable with just two closely-spaced measurements.

Target	Date	Mn λ (nm)	Mn Landé	SNR	v sin i (km s^{-1})	u	FAP	$B_l \pm \sigma B$ (G)	$N_l \pm \sigma N$ (G)	$B_{\rm pol} \pm \sigma B$ or $B_{\rm lim}$ (G)
BD +00 2099	23-Feb-21	536.7149	1.202	1537	24 ± 1	0.5443	DD	-521 ± 35	34 ± 34	> 1646 ± 111
BD +01 1920	07-Jan-24	529.6655	1.208	913	5 ± 1	0.5443	DD	-416 ± 7	-9 ± 6	> 1314 ± 22
BD +08 2211	04-Jan-24	537.8177	1.199	943	6 ± 1	0.5751	DD	152 ± 13	20 ± 7	> 474 ± 40
BD +10 2572	21-Feb-21	540.0438	1.189	1683	10 ± 3	0.5751	DD	-1268 ± 26	10 ± 20	> 3948 ± 82
BD +40 4697	18-May-21	535.3467	1.197	1137	18 ± 1	0.4444	DD	3898 ± 60	16 ± 37	> 12,900 ± 200
BD +43 3648	18-May-21	531.1814	1.205	1520	17 ± 1	0.5046	DD	-2021 ± 106	6 ± 92	> 6504 ± 341
BD +44 767	25-Nov-21	555.8105	1.199	1213	18 ± 1	0.5151	ND	453 ± 192	-40 ± 193	< 1500
BD +49 1011	26-Nov-21	543.1386	1.192	801	7 ± 1	0.4249	DD	-279 ± 38	-35 ± 37	> 934 ± 128
HD 11140	01-Sept-21	533.8171	1.191	2174	21 ± 1	0.4249	DD	206 ± 70	82 ± 70	> 690 ± 234
HD 14251a	30-Aug-21	532.7064	1.191	3416	40 ± 1	0.4249	ND	142 ± 152	82 ± 152	< 2250
HD 14251b					5 ± 2		ND	2 ± 89	-35 ± 89	< 3000
HD 18410	01-Sept-21	542.0123	1.192	1478	21 ± 1	0.5751	DD	1867 ± 39	-7 ± 34	> 5814 ± 121
HD 19846	25-Nov-21	528.7895	1.197	1360	27 ± 1	0.4444	DD	194 ± 50	-48 ± 35	> 642 ± 165
HD 22961	26-Nov-21	529.6589	1.205	1839	18 ± 1	0.5046	DD	102 ± 38	45 ± 38	> 328 ± 124
HD 28238	28-Aug-21	537.5226	1.206	747	6 ± 1	0.5279	DD	-207 ± 17	0 ± 16	> 684 ± 55
	26-Nov-21	536.1829	1.207	822			DD	1 ± 18	17 ± 18	
HD 36259	01-Sept-21	533.7634	1.191	2190	28 ± 1	0.4249	DD	761 ± 19	-1 ± 17	> 2548 ± 63
HD 36955	01-Sept-21	526.764	1.208	1855	33 ± 1	0.5279	DD	-581 ± 60	35 ± 58	> 1849 ± 191
HD 48560	27-Nov-21	529.8405	1.207	1466	8 ± 2	0.5279	DD	-932 ± 30	14 ± 28	> 2967 ± 94
HD 49198	26-Nov-21	525.9691	1.206	1459	15 ± 1	0.5044	DD	-1065 ± 59	-56 ± 50	11,740 ± 2700
	27-Nov-21	524.039	1.206	1394			DD	-2386 ± 72	-26 ± 41	
	18-Feb-22	527.567	1.205	1220			DD	-2841 ± 70	-50 ± 38	
	21-Feb-22	523.3311	1.206	1454			DD	-947 ± 44	41 ± 35	
	22-Feb-22	528.355	1.205	1392			DD	-2115 ± 70	40 ± 45	
HD 49522	23-Feb-21	526.4611	1.205	1221	22 ± 1	0.5046	DD	-2353 ± 25	-7 ± 16	> 7573 ± 80
HD 56514	23-Feb-21	531.4868	1.216	2027	32 ± 1	0.5765	DD	-256 ± 54	1 ± 53	> 795 ± 168
HD 63843	18-Jan-24	526.345	1.189	1708	7 ± 2	0.5659	DD	2191 ± 15	5 ± 10	> 6853 ± 47
HD 66533	27-Nov-21	532.1027	1.197	906	15 ± 1	0.5443	DD	-282 ± 19	-17 ± 18	> 889 ± 59
HD 71047	23-Feb-21	525.6292	1.199	1816	16 ± 1	0.5765	DD	165 ± 28	-1 ± 25	> 516 ± 88
HD 86170	23-Feb-21	534.0372	1.197	924	5 ± 2	0.5443	DD	-104 ± 26	-16 ± 24	> 328 ± 83
HD 108662	20-May-21	534.5184	1.195	1394	20 ± 1	0.4444	DD	-690 ± 73	8 ± 73	> 2283 ± 243
	21-May-21	527.9288	1.197	1118			DD	-5 ± 22	-32 ± 20	
HD 177128	18-May-21	527.0712	1.200	1452	19 ± 1	0.5630	DD	860 ± 58	-67 ± 54	> 2693 ± 183
HD 212714	18-Jul-22	543.2427	1.181	2961	59 ± 7	0.4249	DD	-114 ± 38	-8 ± 38	> 380 ± 128
HD 232285	30-Aug-21	534.9881	1.197	925	7 ± 1	0.4444	DD	771 ± 17	12 ± 13	> 2553 ± 56
HD 256582	22-Feb-22	566.5622	1.197	3907	45 ± 1	0.3749	DD	-154 ± 74	-24 ± 73	> 526 ± 253
HD 259273a	25-Dec-21	528.9497	1.197	2452	5 ± 2	0.4444	DD	-144 ± 8	0 ± 8	> 449 ± 26
HD 259273b					25 ± 2		ND	-2000 ± 990	538 ± 824	< 307
HD 266267	15-Jan-24	540.7631	1.208	919	5 ± 3	0.5765	DD	403 ± 11	27 ± 11	> 1254 ± 35
HD 266311	23-Feb-21	539.0441	1.196	767	8 ± 1	0.5443	DD	-1347 ± 21	-32 ± 18	> 4256 ± 65
HD 277595a	01-Sept-21	539.4005	1.191	3635	13 ± 1	0.4249	DD	527 ± 121	13 ± 120	> 1764 ± 404
HD 277595b					9 ± 1		ND	20 ± 121	-7 ± 121	< 1866
HD 281193	25-Nov-21	537.4729	1.206	2296	104 ± 2	0.5630	ND	628 ± 321	-638 ± 322	< 14,500
TYC 2873-3205-1	01-Sept-21	526.6307	1.201	1815	18 ± 1	0.4724	DD	213 ± 35	-1 ± 35	> 697 ± 114
TYC 3316-892-1	25-Nov-21	538.0924	1.197	1648	18 ± 1	0.4444	DD	965 ± 57	-55 ± 53	> 3192 ± 187
TYC 3319-464-1	01-Sept-21	542.2375	1.198	614	7 ± 1	0.4444	DD	280 ± 22	13 ± 19	> 925 ± 72
TYC 3733-133-1	26-Nov-21	548.7484	1.197	754	9 ± 1	0.5279	DD	-1127 ± 30	-13 ± 24	> 3589 ± 96
TYC 3749-888-1	27-Nov-21	555.074	1.188	2043	25 ± 1	0.5751	DD	-458 ± 63	-47 ± 62	> 1425 ± 196

TABLE 3.2 – Results of magnetic characterisation of our sample. Columns 3, 4, and 5 display the mean values for wavelength and Landé factor, and SNR for the LSD I profiles respectively. In the case of multiple sequences during a single night, these values were averaged together. Our Fourier-method determined values for v sin i are presented in column 6, along with in column 7 the determined limb-darkening coefficients u [80] for $B_{\rm pol}$ calculations. The results of the FAP algorithm are shown in column 8, and the longitudinal field measurements from the Stokes V (B_l) and the corresponding N (N_l) profiles, with their respective errors, are provided in columns 9 and 10. Finally, values for the polar field strength $B_{\rm pol}$ and their errors when a magnetic field was detected or the upper limit $B_{\rm lim}$ for non-detections are presented in column 11. The B_{pol} values for targets having only one or two polarimetric sequences are lower bounds, and have been represented as such.

5 Conclusions

Of our sample of 39 candidates we determined 36 of them to be clearly magnetic, with only one likely non-magnetic and a couple requiring better data to check their magnetic status. Thus, a large number of confirmed mCP stars have been determined, suitable for in-depth follow-up and analysis. In particular, three new magnetic δ Sct stars and one new magnetic SPB star have been discovered in this work. This is an extremely promising result for the study of stellar magnetism.

This study also proves the viability of the method formalised by Hümmerich, Paunzen & Bernhard [160], using the 5200 Å depression combined with rotational modulation as a reliable indicator for the presence of a magnetic field in CP stars. This is a key result, one that can be utilised to generate large lists of candidate mCP stars with very high chances of detecting fields in all of them.

The magnetic pulsating stars determined as a result of this analysis are essential targets for follow-up observations and subsequent magneto-asteroseismic analysis. Such magnetic pulsating hot stars are rare and our discoveries, while few in number, still provide a large increase of targets in this category. Again, thanks to the reliability of the detection method, all targets that fall in the area overlapped by both chemical peculiarity and pulsation can be quickly and efficiently assessed for the presence of the 5200 Å depression and rotational modulation and, with a high likelihood, a magnetic field.

Chapter 4

The complex fossil magnetic field of the δ Scuti star HD 41641

Objectives

Only three magnetic δ Scuti stars were known as of the date of publication. HD 41641 is a δ Scuti star showing chemical peculiarities and rotational modulation of its light-curve, making it a good magnetic candidate. We acquired spectropolarimetric observations of this star with Narval at TBL to search for the presence of a magnetic field and characterise it. We indeed clearly detect a magnetic field in HD 41641, making it the fourth known magnetic δ Scuti star. Our analysis shows that the field is of fossil origin, like magnetic OBA stars, but with a complex field structure rather than the much more usual dipolar structure.

Work based on Thomson-Paressant et al., MNRAS, **500**, 2, p1992-1999 (2020) [95]

Contents

1 Introduction

At time of publication, three δ Sct variables have been found to exhibit magnetic fields : HD 188774 [41], HD 67523 [42], and β Cas [43, 44]. HD 21190 has also been claimed to be a magnetic δ Sct star [45, 46], however this result is in contention with those from Bagnulo et al. [102] and thus is still up for debate. Finally, HD 35929 was claimed as a possible magnetic δ Sct candidate [47] but the spectropolarimetric results were unclear and have not been confirmed.

In this paper, we search for the presence of a magnetic field in HD 41641 using spectropolarimetry, to confirm HD 41641 as the fourth known magnetic δ Sct star.

The observations of HD 41641 are summarised in Sec. 2, the measurements of a magnetic field are presented and modelled in Sec. 3, and the results are discussed in Sec. 4.

2 Spectropolarimetric Observations and Methods

2.1 Observations

To check for the existence of a magnetic field around HD 41641, it was observed over two separate periods. The first occurred during 17 nights, between 21 October 2015 and 2 December 2016, using the Narval echelle spectropolarimeter [172], which is operating on the Bernard Lyot Telescope (TBL) at the Observatoire Midi-Pyrénées, France. The second run was performed over 16 nights, between 19 October 2023 and 15 January 2024, using ESPaDOnS at CFHT. The full list of nightly average observations is visible in Table 4.2.

We used the circular polarisation mode to measure the Stokes V spectrum along with the intensity spectrum, also known as Stokes I. We detail how these are determined in Chap. 1 Sec. 3. In addition, successive Stokes V sequences were acquired to increase the overall SNR of a potential magnetic measurement.

We utilised the LSD method described in Chap. 1 Sec. 5.1 to generate the average line profiles for Stokes I and V, for each observation. To compute the necessary line mask, lines were selected from the *Vienna Atomic Line Database* (VALD) database [67-69]. For HD 41641, the initial mask was computed with an effective temperature $T_{\rm eff} = 7250$ K and a gravity $\log g = 3.5$ dex, selecting only lines with a depth of at least 1% of the continuum level. From this mask, we then removed all hydrogen lines and any lines blended with either telluric lines or hydrogen lines, as well as lines present in the original VALD line list that did not appear in the observed spectrum. Through this processing, the total number of lines to be used by the LSD was reduced from an initial 13,979 to 6,745. For the final mask, the values for the mean Landé factor and mean wavelength were $g_L = 1.6807$ and $\lambda = 531.7517$ nm respectively.

Table 4.1 – Stellar parameters as determined by Escorza et al. [173].

V	7.86 mag	$\log g$	3.5 ± 0.3 dex
M_*	$2.3^{+0.7}_{-0.5}$ $M_\odot$	$v \sin i$	30 ± 2 km.s^{-1}
$T_{\rm eff}$	7200 ± 80 K	RV	29.3 ± 0.3 km.s^{-1}
R_*	$4.5^{+2.7}_{-1.7}$ $R_\odot$	ξ	1.1 ± 0.3 km.s^{-1}

Narval					ESPaDOnS				
Date	Mid-HJD -2457000	T_{exp} s	Phase	SNR	Date	Mid-HJD -2457000	T_{exp} s	Phase	SNR
21 Oct 2015	317.6957	8x4x27	0.124	860	19 Oct 2023	3238.0503	30x4x21	0.195	5890
09 Nov 2015	336.7578	3x4x27	0.519	571	20 Oct 2023	3239.0633	30x4x21	0.375	5537
11 Nov 2015	338.7326	5x4x27	0.870	1325	24 Oct 2023	3242.9876	30x4x21	0.074	5359
12 Nov 2015	339.7545	8x4x27	0.052	1610	25 Oct 2023	3244.0024	15x4x21	0.255	4166
16 Nov 2015	343.6598	8x4x27	0.748	1666	01 Dec 2023	3280.9651	30x4x21	0.837	5129
15 Mar 2016	463.3385	8x4x27	0.061	962	03 Dec 2023	3282.9843	30x4x21	0.197	5803
20 Mar 2016	468.3606	7x4x27	0.955	1846	29 Dec 2023	3308.9267	30x4x21	0.817	5753
08 Oct 2016	670.6344	10x4x27	0.977	2129	30 Dec 2023	3309.9050	30x4x21	0.991	5408
27 Oct 2016	689.5768	10x4x27	0.350	683	31 Dec 2023	3310.8843	45x4x21	0.166	7189
28 Oct 2016	690.7036	10x4x27	0.551	1763	01 Jan 2024	3311.8886	30x4x21	0.344	5632
29 Oct 2016	691.6058	10x4x27	0.712	1775	02 Jan 2024	3312.8903	30x4x21	0.523	5484
30 Oct 2016	692.7331	10x4x27	0.912	1808	03 Jan 2024	3313.9474	30x4x21	0.711	5054
31 Oct 2016	693.6274	10x4x27	0.072	2231	05 Jan 2024	3315.9062	30x4x21	0.060	5161
02 Nov 2016	695.6581	10x4x27	0.433	1843	06 Jan 2024	3316.7739	15x4x21	0.214	4240
25 Nov 2016	718.6306	10x4x27	0.524	1841	07 Jan 2024	3317.9476	30x4x21	0.423	5393
01 Dec 2016	724.4852	10x4x27	0.567	1161	15 Jan 2024	3325.8939	30x4x21	0.839	5489
02 Dec 2016	725.6170	10x4x27	0.769	2237					

TABLE 4.2 – Summarised journal of observations of HD 41641, with averaged nightly profiles and indications of mean Julian Date at midpoint of each observation, exposure time, phase with respect to the rotation period (P_{rot} = 5.6153 d), and signal-to-noise ratio of the Stokes I profiles. The chosen value for HJD_0 is 2457317.0.

To improve the SNR further and reduce the impact of potential remnant signals in N, we performed a weighted average on the observations for each night, in order to generate a mean profile per night which would be used for the remainder of the analysis process. On average, the LSD improved the SNR by a factor of almost 17x between the spectrum and the LSD profile at 500 nm. By averaging several observations, the SNR between a single measurement and the nightly average can be improved by a further 3x, giving a final improvement of 51x.

Through our analysis, it was determined that the observations on 27 Oct 2016 were poor, having a residual signal in N that remained even after night-by-night averaging. This is visible in Fig. 4.1, with the night in question being represented by the dark blue line at phase 0.637. Numerous attempts were made to improve the profile for this night, such as assessing each observation individually and looking for defects, but no clear improvement was observed, and thus it was decided to not consider the 27 Oct 2016 for the remainder of the work.

As mentioned in the introduction, E16 discovered two potential frequencies most likely related to the rotation period of HD 41641 labelled F7 and F24, corresponding to 2.80898876 d and 5.63189907 d respectively. The authors concluded that the rotation period was best represented by F24, but for the sake of completeness and accuracy, both were tested here. In THOMSON-PARESSANT et al. [95], having access only to data from the first observing run, we suggested that F7 was the more viable rotation frequency for a number of reasons based on variability and the 'best fit' to the B_l values. However, since acquiring new datasets in 2023/2024, we can now confidently say that we agree with E16 that F24 is indeed the correct choice, and all tables have been updated to display this.

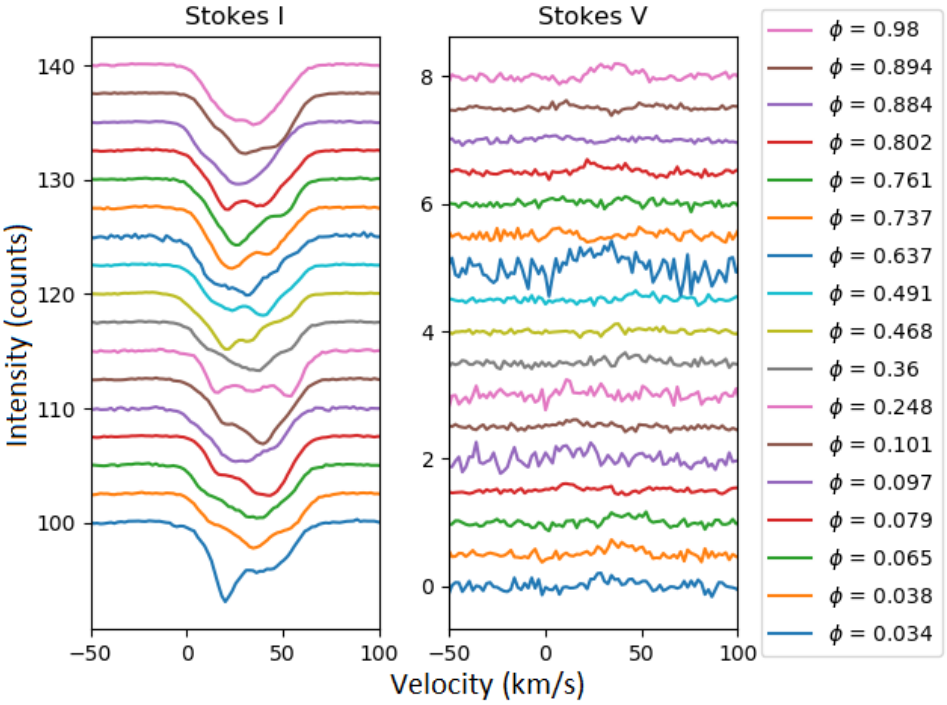

FIGURE 4.1 – Stokes I (left) and Stokes V (right) LSD profiles of HD 41641 for the averaged 17 nights of observation with Narval, artificially shifted vertically to improve readability and ordered from bottom to top with respect to their phase using the rotation frequency F7.

2.2 Testing chemical signatures

The LSD Stokes I profiles visible in the left panel of Fig. 4.1 displayed bump features present within the line profile that evolve on a night-by-night basis. This could be the result of either brightness or chemical spots on the surface of the star, or the δ Scuti pulsations. In the case of a spot, this can be tested by comparing the bumps by particular chemical elements in order to determine their distribution on the surface.

With this in mind, we created a submask for each element present within the LSD mask and which had $\gtrsim$ 30 lines to maintain a minimum SNR threshold (with a few exceptions such as Nitrogen). We ended up with 24 submasks, each with a number of respective lines as presented in Table 4.3. Since the lines in the original mask were extracted from VALD, the line identification used for the submask is the one from VALD, which may not always be correct. Due to the limited number of lines in the case of certain elements, we chose to group lines resulting from both neutral and ionised states of each element together.

By applying the LSD method with each of the chemical submasks, we can generate a set of profiles that correspond to the lines from each chemical element, which can then be averaged night-by-night, as was done for the full spectrum. These can then be analysed in two ways : either by comparing for a single element all the averaged nightly profiles, or by comparing on a single night the averaged spectra for all the elements.

We elected to begin by the latter, observing all the elements for a single night, beginning with

TABLE 4.3 – Distribution of spectral lines for elements detected within the spectra of HD 41641.

Z	Element		Nb of lines	Z	Element		Nb of lines
6	Carbon	C	119	26	Iron	Fe	1763
7	Nitrogen	N	11	27	Cobalt	Co	113
8	Oxygen	O	21	28	Nickel	Ni	189
11	Sodium	Na	23	39	Yttrium	Y	30
12	Magnesium	Mg	64	40	Zirconium	Zr	55
14	Silicon	Si	133	57	Lanthanum	La	41
16	Sulfur	S	61	58	Cerium	Ce	344
20	Calcium	Ca	125	59	Praseodymium	Pr	40
22	Titanium	Ti	311	60	Neodymium	Nd	164
23	Vanadium	V	137	62	Samarium	Sm	111
24	Chromium	Cr	427	64	Gadolinium	Gd	64
25	Manganese	Mn	175	66	Dysprosium	Dy	36

the 2 Dec 2016 due to its high SNR, and eventually comparing individual nights. We observed that most elements displayed a clear "dip" on the blue wing of the profile and additional smaller features, while others had less clear features with the strongest sometimes rather on the red wing. This initially seemed to define two families of elements, suggesting the possible existence of two distinct chemical regions on the surface. To confirm this, the elements were grouped into their two respective families and plotted by family. It was determined that those presenting a main feature on the red wing simply had too low of an SNR, presenting other noisy features not related to anything physical. Indeed, by referring back to the number of lines that these elements presented, they all had < 100 lines each. As such, it was concluded that only a single pattern exists, with a main spot on the blue wing on 2 Dec 2016, and visible in all chemical elements for which sufficient SNR can be reached. Checking the other nights, we saw that this pattern travels along the line profiles with time. Since it appears for all chemical elements, it must be either a brightness pattern or pulsations, rather than specific chemical inhomogeneities.

In E16, during their analysis of the chemical abundances of HD 41641, the authors suggested that these spot-like features might be due to local concentrations of particular elements. However, from our results, we must rather conclude that the spots are not related to local concentrations of chemical elements.

2.3 Testing the presence of a companion

A theoretical companion to HD 41641 had been proposed by both E16 and PORETTI et al. [174], but both achieved different conclusions after further study. Poretti suggested that HD 41641 could be a double-lined spectroscopic binary, whereas E16 determined that other lines within the frequency space were merely due to chemical spots.

In the spectra presented here, we note a small velocity shift (visible in Fig. 4.5) between observations taken 6 months apart. This does not seem to be related to an instrumental effect and could therefore be a sign of the presence of a companion. In addition, through the analysis of the intensity profiles by chemical element, a feature was discovered with a slight offset in

velocity to the primary source, between -100 and -50 km/s, which could also be a signature from a companion. We subsequently checked for the existence of a companion to our target star.

We theorised that, should such a companion exist, and considering that it does not appear in the full LSD profiles (i.e. with all chemical elements included), it would be much cooler than our target. Thus, we performed a similar process as had been completed up to now with our target, but instead using a line mask extracted from the VALD database information for significantly cooler stars, setting $T_{\rm eff} = 3500$ K and maintaining an identical value for the surface gravity. If a cool companion was present, this process should accentuate the lines from the companion and reveal its existence. Having completed this analysis, it was quickly apparent that no clear signs of a companion exist. In particular the feature between -100 and -50 km/s does not appear in the cool star LSD profiles and was likely just noise.

To summarise, in the data presented in this study, we find no compelling evidence of a cool companion.

3 Magnetic field

3.1 Magnetic field measurements

The LSD Stokes V profiles visible in the right panel of Fig. 4.1 display a clear signature. Applying a FAP algorithm to the averaged nightly profiles yielded that 10 out of the 17 nights revealed definite signal detection in V, with an additional one showing a marginal detection. The value ranges for the respective detection types is described in Chap. 1 Sec. 5.2. There were no detections in N for any of the profiles. The number of definite detections in Stokes V, with none in N, clearly shows the existence of a magnetic signal in HD 41641. Although the FAP shows no detection in N, we decided nonetheless to continue to ignore the 27 Oct 16 profile in the remainder of this work, as visibly its N profile does not look flat (see the profile for phase 0.637 in Fig. 4.1).

From the remaining 16 averaged profiles, after having removed the 27 Oct 16 data, dynamical plots were generated, with a phase binning of 0.017. The bin size was selected in such a way as to ensure the greatest amount of clarity for the dynamical plots, and reduce empty space between profiles. As such, some profiles overlap slightly in phase-space.

Fig. 4.2 and 4.3 display the residual LSD Stokes I and the Stokes V profiles respectively in the bottom panel, as well as colourscales of these profiles folded with the frequency F7 in the top panel.

For Stokes I (Fig. 4.2), although the phase coverage is not ideal, the evolution of the bumps along the profile is nonetheless visible. This pattern is visible when the profiles are folded with F7, i.e. with the rotation period or an harmonic thereof. Nothing clear appears when we fold the Stokes I profiles with any of the main pulsation frequencies listed by E16. We thus conclude that the observed bumps are due to a brightness pattern rather than to the δ Scuti pulsations.

This brightness pattern could be directly related to the presence of an oblique dipole field, as observed in hot stars, for example the main spot could be a magnetic pole or there could be an eclipse by a magnetosphere. However, looking at the Stokes V colourscale (Fig. 4.3), there is

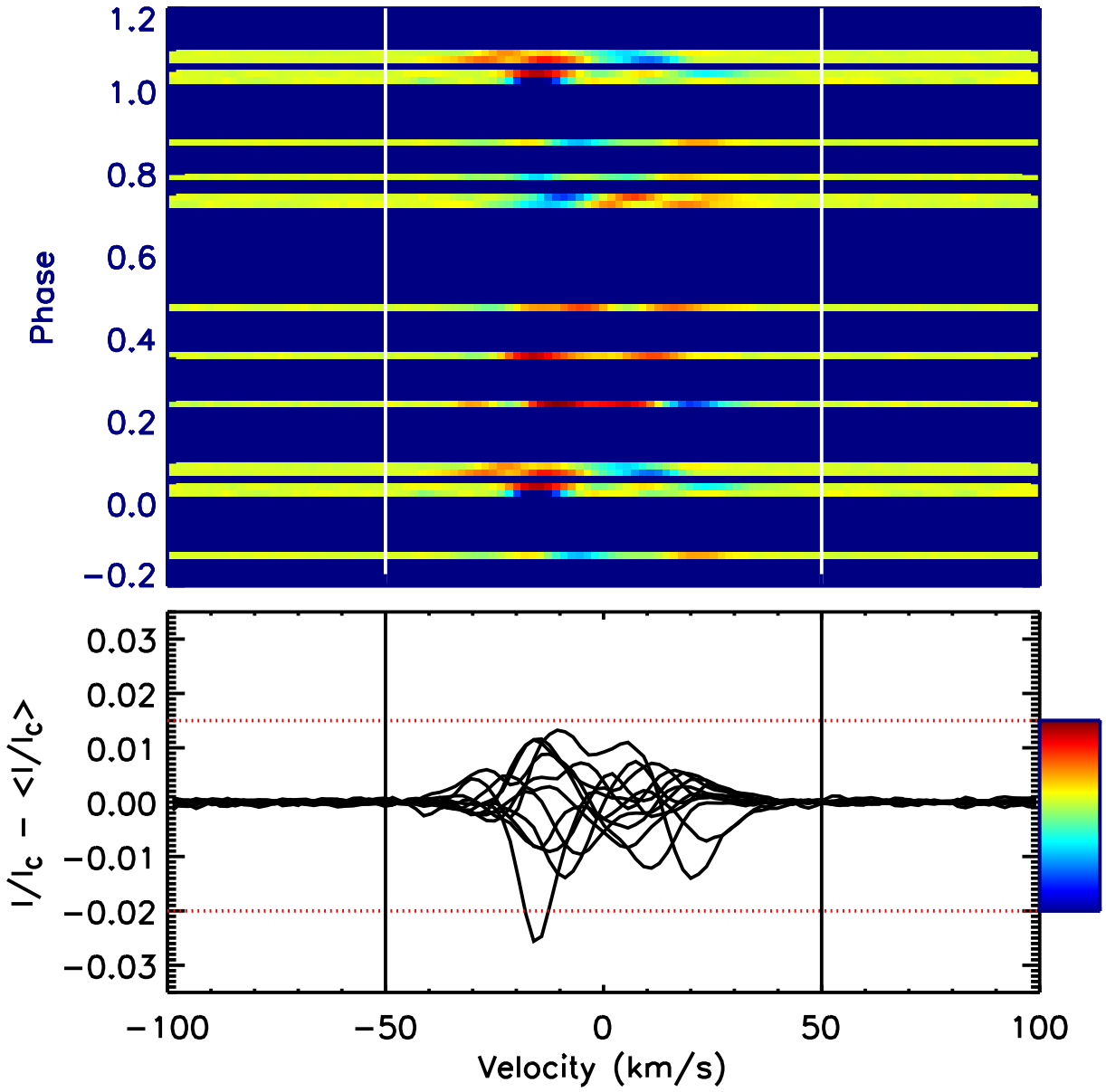

FIGURE 4.2 – Residuals of the LSD Stokes I profiles with respect to the averaged Stokes I profile shown over-plotted (bottom panel) and as a dynamical plot folded in phase with the rotation frequency F7 (top panel). Colourbar represents values of Stokes I that vary between -0.02 (blue) and 0.015 (red) of the average profile value.

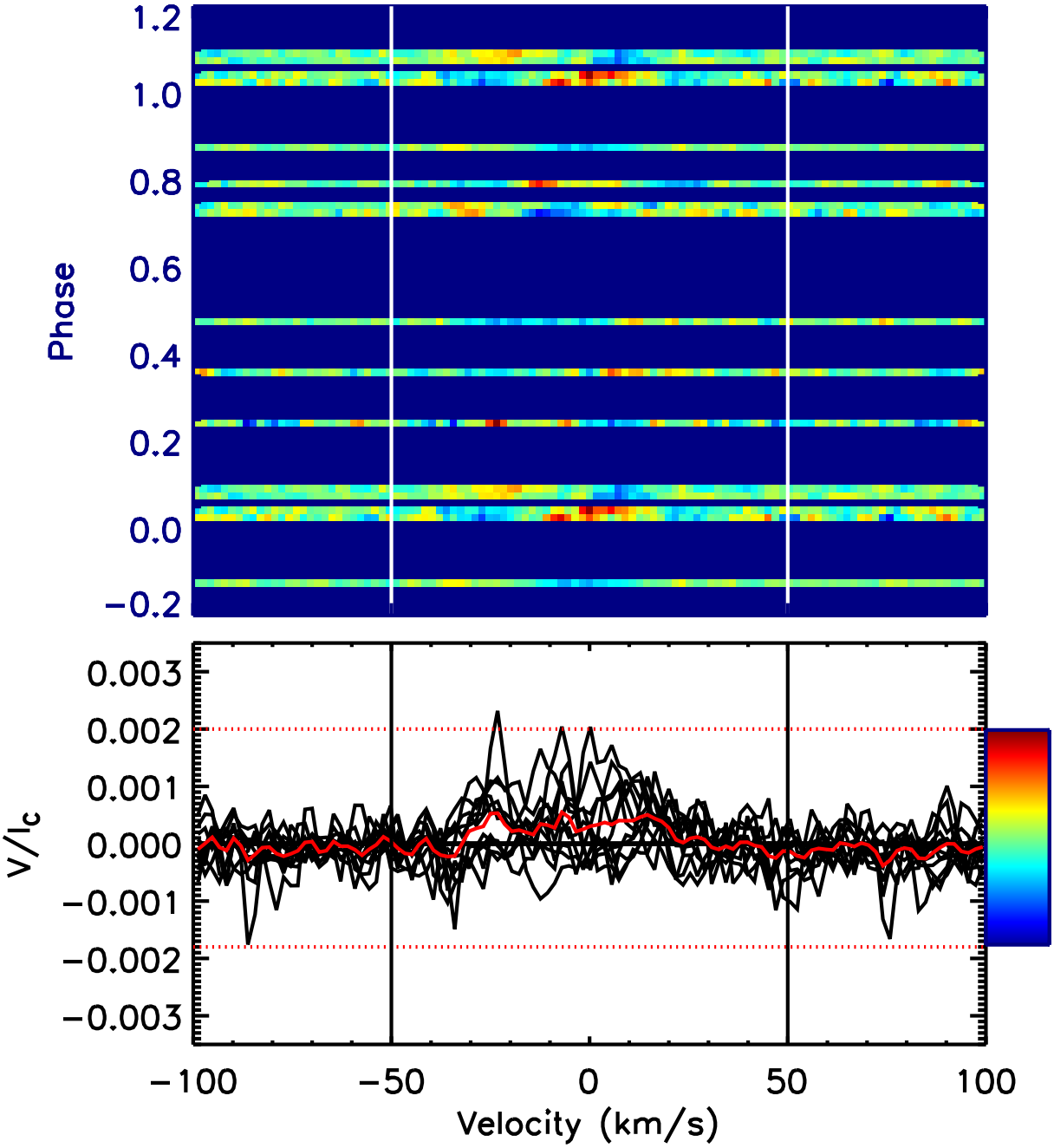

FIGURE 4.3 – LSD Stokes V profiles (bottom panel) and corresponding dynamical plot folded in phase with the rotation frequency F7 (top panel). Colourbar represents values of Stokes V that vary between -0.0018 (blue) and 0.002 (red). The red line corresponds to the average of all the profiles.

Narval				ESPaDOnS			
Date	FAP	$B_l \pm \sigma B$ (G)	$N_l \pm \sigma N$ (G)	Date	FAP	$B_l \pm \sigma B$ (G)	$N_l \pm \sigma N$ (G)
21 Oct 2015	ND	438 ± 145	330 ± 145	19 Oct 2023	DD	263 ± 16	28 ± 16
9 Nov 2015	ND	-175 ± 117	-100 ± 117	20 Oct 2023	DD	71 ± 12	-4 ± 12
11 Nov 2015	ND	-3 ± 100	-29 ± 100	24 Oct 2023	DD	159 ± 16	7 ± 16
12 Nov 2015	DD	226 ± 61	40 ± 61	25 Oct 2023	DD	258 ± 21	-2 ± 21
16 Nov 2015	ND	-161 ± 84	-16 ± 84	1 Dec 2023	DD	-75 ± 19	-58 ± 19
15 Mar 2016	ND	95 ± 205	-85 ± 205	3 Dec 2023	DD	255 ± 15	18 ± 15
20 Mar 2016	ND	47 ± 58	19 ± 58	29 Dec 2023	DD	-130 ± 14	0 ± 14
8 Oct 2016	DD	-40 ± 55	-6 ± 55	30 Dec 2023	DD	92 ± 13	2 ± 13
27 Oct 2016	DD	49 ± 255	-105 ± 255	31 Dec 2023	DD	228 ± 12	-3 ± 12
28 Oct 2016	DD	-123 ± 94	-45 ± 94	1 Jan 2024	DD	92 ± 13	-30 ± 13
29 Oct 2016	MD	-258 ± 112	27 ± 112	2 Jan 2024	DD	-90 ± 13	-16 ± 13
30 Oct 2016	DD	-3 ± 79	-85 ± 79	3 Jan 2024	DD	-230 ± 20	24 ± 20
31 Oct 2016	DD	227 ± 55	73 ± 55	5 Jan 2024	DD	198 ± 20	14 ± 20
2 Nov 2016	DD	-97 ± 75	-146 ± 75	6 Jan 2024	DD	293 ± 20	-11 ± 20
25 Nov 2016	DD	-124 ± 75	-6 ± 75	7 Jan 2024	DD	10 ± 13	15 ± 13
1 Dec 2016	DD	-143 ± 95	72 ± 95	15 Jan 2024	DD	-116 ± 16	-8 ± 16
2 Dec 2016	DD	-195 ± 54	-30 ± 54				

TABLE 4.4 – Magnetic detection status from FAP results, along with longitudinal magnetic field measurements (B_l) from the LSD Stokes V profiles and similar measurements (N_l) from the LSD Null profiles, including their respective errors calculated outside the line profile region. Also included are the FAP results, with magnetic detection status represented by Definite (DD), Marginal (MD) and Non-detection (ND).

no clear dipolar pattern visible.

3.2 Longitudinal magnetic field

The next stage of the process involves calculating the values for the longitudinal magnetic field B_l from the LSD Stokes V and I profiles, following the procedure described in Chap. 1 Sec. 5.2. It is important to define an appropriate region about the line profile, as selecting one that is too large or too small can cause erroneous results. With this in mind, we determined a velocity range of ± 50 km.s^{-1} around the line centroid. The results are displayed in Table 4.4, along with similar measurements in N, and their respective error values. Subsequently these B_l values were plotted with respect to rotation (F7) phase as seen in Fig. 4.4, along with a 1-term and a 2-term sinusoidal fit, in order to visualise the variation of the magnetic field with respect to the rotation of the star. We find that the B_l values do not seem to follow a sinusoidal pattern, i.e. that the magnetic field does not seem to be dipolar.

To get a sense of the magnetic field strength, we nevertheless use the dipolar fit to B_l values and deduce :

$$\begin{cases} B_l^+ \sim 59.6 \pm 0.6 \text{ G} \\ B_l^- \sim -170.3 \pm 0.6 \text{ G} \end{cases}$$

We can then derive the polar field strength B_{pol} and the magnetic field obliquity β (assuming a dipole field).

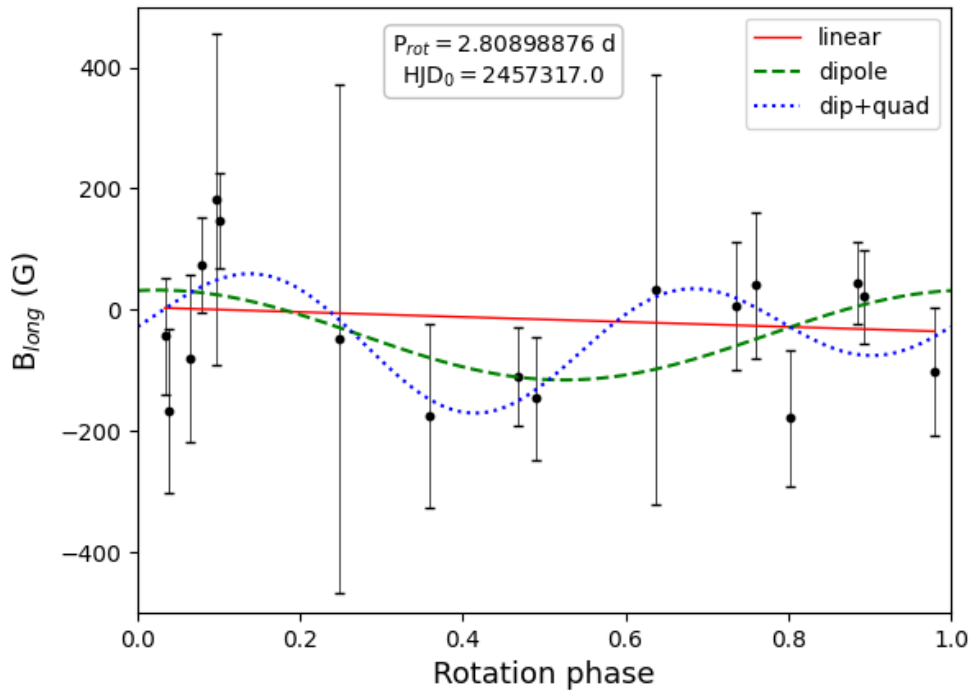

FIGURE 4.4 – B_l values with respect to phase, setting F7 as the rotation frequency. Full red, dashed green and dotted blue line fits represent respectively the linear, sinusoidal (dipolar field) and double-wave (dipolar+quadrupolar field) models of the B_l values.

Since we determined that F7 is the rotation frequency rather than F24, we first determined a new value for i, which differs from the one found by E16. This value corresponds to $i = 22 \pm 11°$. Using the ratio $r = B_l^+/B_l^- \sim -0.35$ and following the work completed by PRESTON [78] and LANDSTREET [175], we then find $\beta = 79 \pm 11°$. Finally, using the aforementioned parameters for i, β and B_l, a value for $B_{\rm pol}$ can be determined, following SCHWARZSCHILD [79] and using a limb-darkening coefficient of 0.4 :

$$B_{\rm pol} = \frac{B_l^{\pm}}{0.296 \times \cos(i \mp \beta)} = 1055^{+?}_{-689}\ \text{G} \tag{4.1}$$

In addition, we modelled the LSD Stokes V profiles with these parameters. We obtained a poor fit to the observations, in particular an incompatible shape of the Stokes V profiles, which confirms that a simple dipole does not match the observations. We can then compare the reduced χ^2 values for a linear ($\chi^2_{\rm red} = 1.098$), dipolar ($\chi^2_{\rm red} = 0.772$) as well as dipolar+quadrupolar ($\chi^2_{\rm red} = 0.887$) fit. These results suggest that the dipolar and dipolar+quadrupolar fits are slightly better fits to the data than the linear fit. This suggests that some rotational modulation is indeed present in the data. However, the error bars for some points are particularly large and could be represented by any fit, while several other points are wholly excluded from the sinusoidal fits. We therefore conclude that rotational modulation is present in the data but that a simple configuration (dipolar or dipolar+quadrupolar) does not represent the data well.

3.3 Choice of rotation frequency

As we mentioned earlier, there was some disagreement between our findings and those of E16 with regards to which frequency corresponded to the rotation frequency of HD 41641. E16 suggested that the frequency labelled F24, with a value of $f = 0.17756$ d^{-1}, was the correct one whereas our initial results suggest that F7, at $f = 0.3560$ d^{-1}, coincides more accurately with the rotation. Both frequencies are intrinsically linked, with F7 being twice that of F24.

We initially determined F7 to be the correct rotation frequency due to the following factors :

— By plotting the B_l values with respect to F7, as seen in Fig. 4.4, we see that observations obtained at different epochs but similar phases have similar longitudinal field values. Although the signal is not sinusoidal (i.e. dipolar), it appears periodic with F7. Using F24 instead shows no such periodicity.

— Similarly, this is also the case when considering the residual Stokes I dynamical plot, Fig. 4.2, where the evolution of the line profile with respect to phase draws distinct tracks with both the positive (blue) and negative (red) amplitudes when using F7. Again, this is not apparent when substituting F24.

— Finally, comparing Stokes V profiles of observations taken approximately 6 months apart (Fig. 4.5) on 20 Mar 2016 and 8 Oct 2016, and with very similar phase values of 0.88436 and 0.89384 respectively when using F7, it is immediately apparent that they are analogous apart from a slight shift in velocity visible in both Stokes I and V. These 2 similar profiles would have different phases when using F24.

Once we had access to the new ESPaDOnS datasets, we were able to reassess this factor, and concluded that the analysis done by E16 was indeed correct, such that F24 is the true rotation frequency. This has been taken into account in Tables 4.2 and 4.4.

3.4 Modelling the LSD Stokes profiles

To further check the configuration of the magnetic field, an attempt was made to model the LSD Stokes V profiles with a dipole field with free parameters. To this end, we utilised the method described in Alecian et al. [176]. In essence, this is an oblique rotator model, where we fit 4 or 5 parameters : the inclination angle i between the rotation axis and observer's line of sight, the obliquity angle β of the dipole field with respect to the rotation axis, the polar field strength $B_{\rm pol}$, a phase shift with respect to the chosen ephemeris $\Delta\psi$, and an optional off-centring distance d in the off-centred dipole case ($d = 0$ for a centred dipole and $d = 1$ if the centre of the dipole is at the surface of the star). We provide certain values such as macro- and micro-turbulence, phase values assuming F7 is the rotation frequency, mean wavelength and Landé factor, while fitting Gaussians to the Stokes I spectra to generate values for the depth of the Stokes I profile, $v \sin i$, and the radial velocity.

We calculated a grid of Stokes V profiles by varying the 4 or 5 parameters within user-defined bounds, and using a χ^2 minimisation to determine the best fit values. This can be repeated several times, with the parameters converging on more accurate values with each loop.

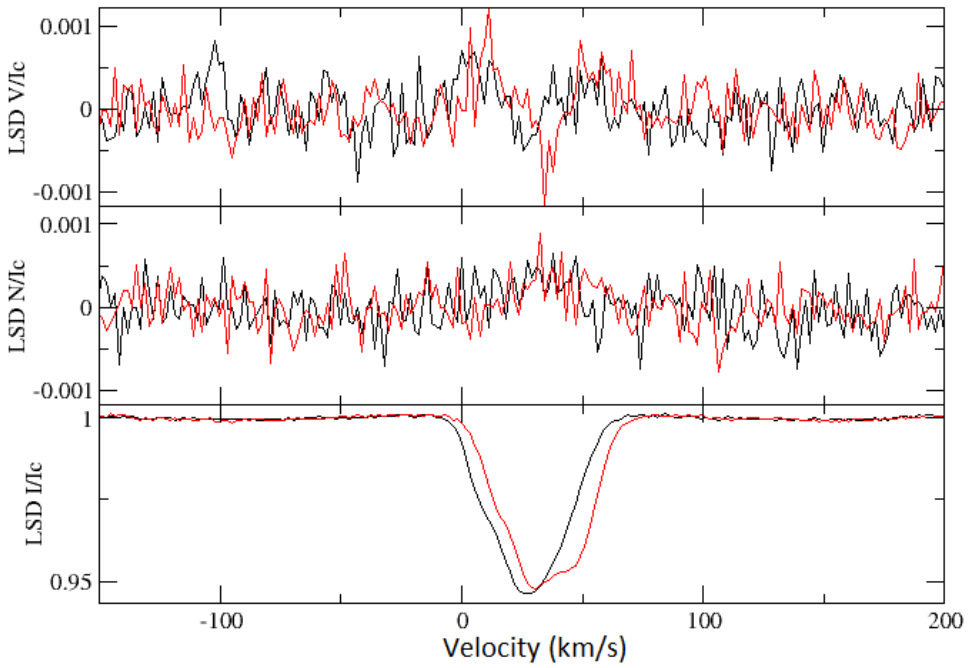

FIGURE 4.5 – Stokes V (top), N (middle), and Stokes I (bottom) LSD profiles of HD 41641 for the nights of the 20 Mar 2016 (black) and 8 Oct 2016 (red).

Using these best fit parameters, we can then try to fit a model curve to all the LSD Stokes V profiles simultaneously, in an attempt to reveal a possible dipolar signal.

It became quickly apparent that no such dipolar signal exists for HD 41641, as the model fits extremely poorly, fitting extremely few of the features visible in the LSD profiles. To ensure that the fitting process had converged properly, it was repeated several times with various first guess parameters, while also rejecting the region of the main spot within the profile when fitting the Stokes I spectra prior to modelling.

The results of the modelling are listed as follows. We determined two combinations of inclination and obliquity angles, which effectively corresponds to $i = 70 \pm 5°$ and $\beta = 30 \pm 5°$, and $i = 30 \pm 5°$ and $\beta = 70 \pm 5°$, both with $\chi^2 = 1.875$. The model also suggests a phase shift $\Delta\psi = 0.0738 \pm 0.005$ and, assuming it is a dipole, a maximum polar field strength of $B_{\rm pol} = 1880 \pm 10$ G.

The best-fit model is visible in Fig. 4.6. We stress that the dipolar fit to the data is very poor and the above values must therefore be considered with great care and are provided here only to give an idea of the amplitude of the magnetic field signature. This model again shows that a dipolar fit is not appropriate for this star.

Comparing the results determined here for i, β and $B_{\rm pol}$ with those calculated in Sec. 3.2, it is clear there is quite an offset, though this is expected as a result of the poor dipolar fit. We do however see a match between the calculated values of $\beta = 79 \pm 11°$ and $i = 22 \pm 11°$ and the model with values of $\beta = 70 \pm 5°$ and $i = 30 \pm 5°$. Finally, the error bar of the calculated $B_{\rm pol}$ looks far more reasonable than the range of possible values determined by the dipolar modelling in Sec. 3.2, but considering the bad fit we obtain, this error bar is not realistic.

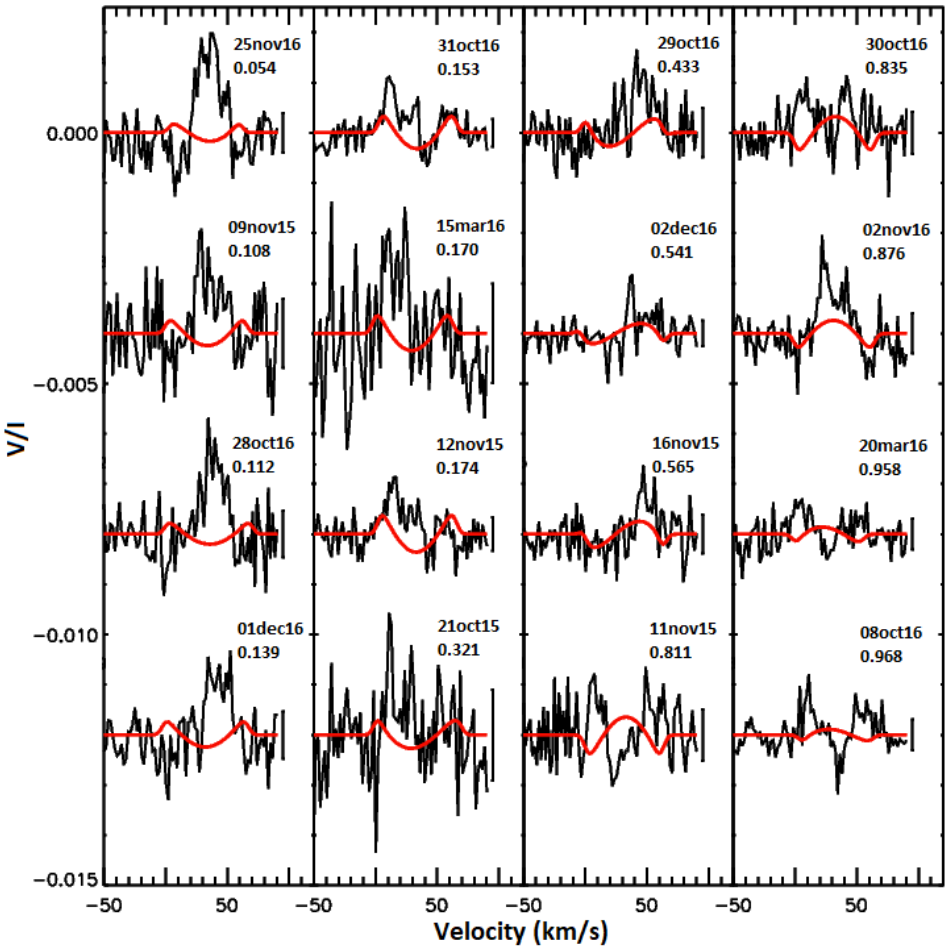

FIGURE 4.6 – Results of dipolar modelling performed on the 16 best profiles. Profiles are ordered in phase, increasing vertically first then horizontally. Model fit is displayed as red overlay.

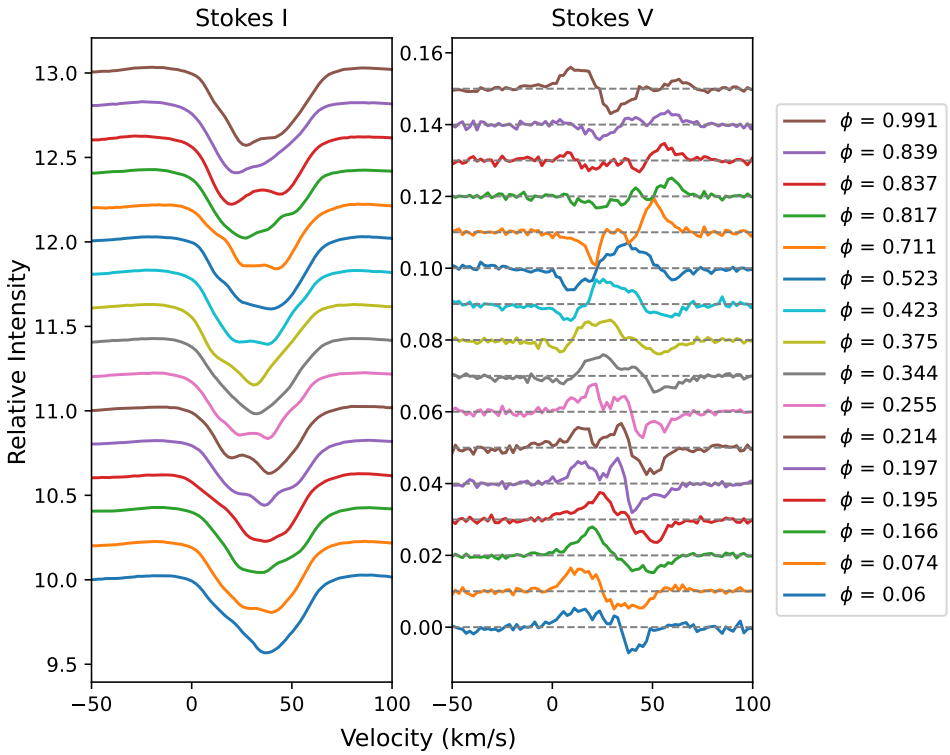

FIGURE 4.7 – Stokes I (left) and Stokes V (right) LSD profiles of HD 41641 for the averaged 16 nights of observation from ESPaDOnS, shifted vertically to improve readability, and ordered from bottom to top with respect to their phase using the rotation period $P_{\rm rot} = 5.6153$ d. The zero-point for each Stokes V profile has been indicated with a dashed line.

3.5 Analysis following new 2023/2024 datasets

As described in Chap. 1 Sec. 2.1, we recently acquired several hundred new datasets for HD 41641, over the course of 16 nights. Thanks to the greater quality of the data and improved phase coverage, we are able to perform a more precise characterisation of the star's magnetic field. Over the following paragraphs, we will present our findings.

The datasets were processed in exactly the same way as the previous ones, utilising an identically tailored template mask and having consecutive sequences taken on a given night averaged together to significantly improve the SNR of the resulting LSD Stokes profiles. These Stokes profiles are visible in Fig. 4.7, ordered with respect to rotation phase using $P_{\rm rot} = 5.6153$ d (which corresponds to a more precise determination of F24, which will be discussed later) and $\mathrm{HJD}_0 = 2457317.0$.

We then calculated longitudinal magnetic field values B_l for our new datasets, visible in Table 4.4. By combining the two epochs of observations, we end up with a very good phase coverage, allowing for a more precise determination of the rotation period by fitting to the B_l values. We performed a grid of dipolar fits to the full list of magnetic field measurements with respect to the mid-HJD of each night-averaged observation, using a range of values around both F7 and F24, in order to determine the fit with the best overall visual appearance and χ^2 result. This investigation led to the determination (and confirmation) that E16 were correct in

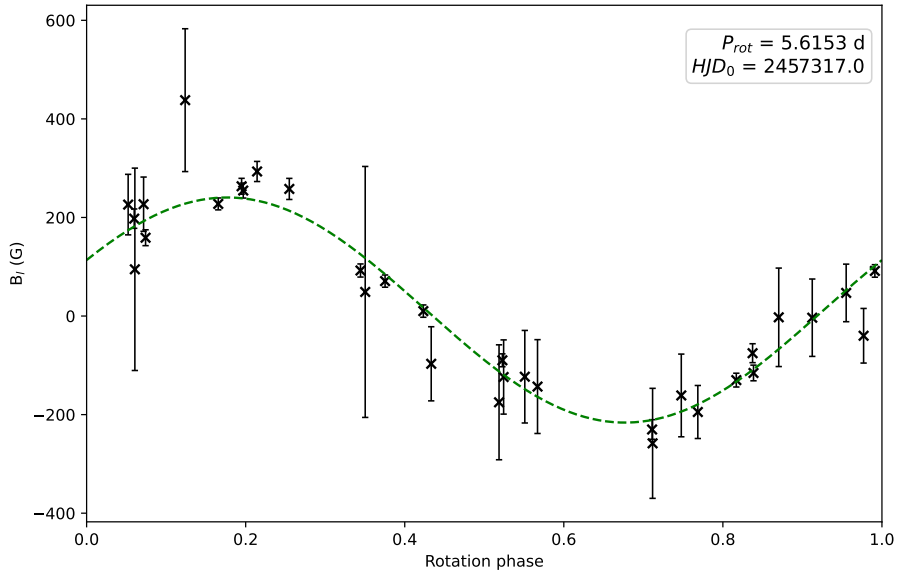

FIGURE 4.8 – B_l values with respect to phase, using the newly determined rotation frequency $f_{\rm rot} = 0.178085$ d^{-1}. Green line represents the dipolar field model fit to the B_l values.

their assessment that F24 is the correct approximation to the rotation frequency. Through our analysis, we were able to further refine this value, reaching a final result of $f_{\rm rot} = 0.178085$ d^{-1}, or $P_{\rm rot} = 5.6153$ d. A representation of the full set of B_l measurements and the resulting dipolar fit is visible in Fig. 4.8. It is now abundantly clear that the field has a dipolar structure and that it stable over periods of several years, thanks to the determination of the correct rotation frequency.

Using this new dipolar fit, we can calculate new values for the maximum and minimum of the field as

$$\begin{cases} B_l^+ = 240.5 \pm 9.0 \text{ G} \\ B_l^- = -216.2 \pm 9.0 \text{ G} \end{cases}$$

and, following the same method as before, we calculate revised values for inclination i, obliquity β, and polar field strength $B_{\rm pol}$ as

$$i = 76 \pm 12^\circ \qquad \beta = -103 \pm 13^\circ \qquad B_{\rm pol} = 748 \pm 28\ G \tag{4.2}$$

The determinations of both i and β have changed, and by consequence so too has $B_{\rm pol}$. While the nominal value of the latter has decreased somewhat, the precision has improved significantly.

4 Conclusions

We carried out a spectropolarimetric study of the δ Sct star HD 41641, complementing the findings of E16. We first utilised data taken with the Narval echelle spectropolarimeter from 21 October 2015 to 2 December 2016. The spectra were used to determine the existence and possible origin of the magnetic field of HD 41641, as well as confirm some of the stellar parameters as determined by E16.

First of all, we confirm that HD 41641 is indeed magnetic, making it the 4th magnetic δ Sct star discovered to date. Through our analysis, we initially determined that a different rotation frequency than the one suggested by E16 fit the data more accurately. Switching from a frequency of 0.17756 d^{-1} to 0.3560 d^{-1} revealed a periodic variation in the magnetic field measurements as well as in the LSD Stokes I profiles. As a result, some of the other stellar parameters calculated by E16, such as the inclination i, were no longer suitable and required recalculation. The new value for i was determined to be $i = 22 \pm 11°$ and the magnetic obliquity angle β, assuming a dipolar field, was found to be $\beta = 77 \pm 11°$.

This led to the deduction that HD 41641 presented characteristics consistent with a fossil field. By comparing Stokes V profiles at the same rotational phase, but with observation periods separated by 6 months or more, as is the case in Fig. 4.5, we observe very similar features, i.e. the field is stable over a period of at least a year. In addition, HD 41641 is hot and not a fast rotator, and thus fits the criteria for a typical fossil field-type magnetic field. However, modelling produced no evidence of a dipolar structure to the field using F7, which pointed towards a complex fossil field. Such complex fossil field are rare but exists, e.g. HD 37776 [177], but additional observations are necessary to properly characterise the field and assess the long-term variability.

Following these conclusions, we acquired an additional suite of data 7 years after the previous set. By proceeding in exactly the same fashion as before, our analysis led to some new conclusions.

First, in contradiction with our initial decision, we determined that F24 and not F7 is the frequency that most closely correlates with rotation, aligning with the results previously found by E16. This value of rotation frequency was then fine-tuned by our own analysis, utilising the B_l measurements from both observation runs and using a grid search to determine the best fitting sinusoid. We now propose a value of $f_{\rm rot} = 0.178085$ d^{-1}.

Finally, using this new rotation frequency, we can conclusively determine that HD 41641 presents a dipolar field of fossil origin, as it is demonstrably stable over a period of several years. This led to new calculations for the inclination, obliquity, and polar magnetic field strength, finding values of $i = 76 \pm 12°$, $\beta = -103 \pm 13°$, and $B_{\rm pol} = 748 \pm 28$ G respectively.

With the good phase coverage we now have access to, by combining both epochs of observational datasets together, the next step in this analysis is to perform ZDI modelling to map the magnetic field and the pulsation modes over the surface of the star. This will be the purpose of a future paper.

Chapter 5

Discovery of new magnetic δ Scuti pulsators and current state-of-the-art in δ Scuti magnetism

Objectives

At this time, the list of known magnetic δ Scuti stars is extremely limited, with only a handful of well-studied examples. We seek to expand this list, by retrieving targets from a variety of sources and demonstrating that they present simultaneously a magnetic field signature and δ Scuti pulsation frequencies. We obtained archival and new spectropolarimetric datasets from a variety of known δ Scuti stars and analysed them using the LSD method to generate mean Stokes I and V profiles for each target, from which we can determine longitudinal magnetic field measurements. Additionally, we assessed photometric data from the *TESS* satellite to identify frequency peaks consistent with δ Scuti pulsations in known magnetic stars. We present a compiled list of all the confirmed magnetic δ Scuti stars discovered to date, containing 13 stars. The majority of this sample lies outside the usual δ Scuti instability strip in the H-R diagram, which suggests that magnetism has an impact on the structure and evolution of these stars, though we do not observe any unusual correlations between magnetic field strength and various stellar parameters. This does not align with theoretical predictions, and indicates that there remains missing ingredients to determine the impact of magnetism on stellar structure and evolution. This constitutes the largest database to date of its kind, one that will continue to grow over time with subsequent studies.

Work based on Thomson-Paressant et al., A&A, in prep. (2024)

Contents

1 Introduction

The field of stellar magnetism has progressed in leaps and bounds in the past decade, as our techniques for identifying *a priori* indicators of the presence of magnetic fields have evolved and improved over time, thanks in part to the ever-growing list of known and well-studied magnetic stars. In the case of δ Scuti stars (δ Sct), the first spectropolarimetrically confirmed target was only discovered in 2013 [HD 188774, 94], with an additional few being added to the list in the years following (ρ Pup, [42] ; β Cas, [44] ; HD 41641, [95]). While recent efforts to perform large-scale studies in this field have had varying degrees of success [86, 143], in the hopes of generating a database of known magnetic δ Sct, the rate of detection appears to be gradually increasing over time. Regardless of the success of these studies, they inevitably provide insight and additional observational constraints, such that subsequent studies are more fine-tuned and thus more likely to provide positive results.

Amongst the already known magnetic δ Sct, there does not appear to be any consistency in the characterisations of their magnetic fields, suggesting the existence of several regimes. However, due to the limited size of the dataset, it is difficult to conclude as to the origin of this diversity and what mechanisms might be responsible for the existence of the observed diversity. In order to be able to hypothesise as to the nature of this disparity, as well as assess whether any correlations exist between the stellar parameters of δ Sct stars and the representation of magnetism in these stars, it is essential to expand this database and acquire a larger list of well-studied magnetic targets.

It is with this goal in mind that we propose a list of 13 spectropolarimetrically confirmed magnetic δ Sct, that we have identified and characterised to verify their nature, and which represents all known targets of this type discovered to date. From this list, we hope to begin to visualise any possible correlations that might exist between the character of their magnetic field and key stellar parameters, and provide a first statistical image of magnetism in δ Sct stars.

2 Data analysis

The targets in our sample have been compiled from a number of sources in the literature. Five were already known to be magnetic and we demonstrate the existence of δ Sct pulsations (HD 8441 and HD 68351, [178] ; HD 10783, [179] ; HD 81009, [180] ; HD 213918, [181]), and to this list we also include HD 73857, which was previously identified as a δ Sct in the literature [182] and for which we show is also magnetic. To ensure the veracity of the targets in our sample, we imposed the following restrictions : i) that they have at least a single sector of *TESS* (preferably several) to verify the presence of δ Sct pulsations, and ii) that spectropolarimetric data is available to determine the magnetic nature of the star.

A number of young Herbig-type stars have also been shown to present both features (e.g. HD 35929 and HD 72106), but for the purposes of this study we have elected to only consider targets that have evolved to the main sequence or slightly beyond.

In the following subsections, we will briefly describe the procedure performed to validate the two aforementioned selection criteria.

2.1 *TESS* photometry

To correctly identify the pulsation frequencies in our target sample, and assess whether there might be blending of stellar signals as a result of close neighbours, we utilise photometric data from the *TESS* [89], made available thanks to the *Mikulski Archive for Space Telescopes* (MAST) at the Space Telescope Science Institute [1].

We followed a very similar procedure to the one described in Labadie-Bartz et al. [166], but the key steps will be reiterated below for completeness. Light curves were extracted from the *TESS* FFI, using the Lightkurve [183] and TESScut [184] packages to select a 40×40 pixel image around each target from which to extract the light curves. In all cases, the latter were detrended using a principle component analysis (PCA) method, excluding a 10×10 pixel square centred on the target star and using the remaining pixels in the image as regressors. The light curves were then subjected to an initial multi-term Fourier analysis with the goal of fitting frequencies below 0.5 d^{-1}, which was then subtracted from the data. These low frequencies typically include rotational and systematic signals that are detrimental to our analysis.

We also retrieved individual observations at either 120 or 20 second cadence, depending on which were available, for each of our targets. This permitted us to assess the very high frequency domain ($f > 72$ d^{-1}) and check for roAp oscillations, which can be reflected into the δ Sct regime due to the Nyquist limit generated from the FFI light curves. These light curves are made available on MAST already extracted and provides two options for detrended flux. We utilised the flux values corresponding to the Pre-search Data Conditioning Simple Aperture Photometry (PDCSAP), which removes long term trends and systematics.

Both types of light curves (FFI and PDCSAP) were then put through Fourier analysis techniques, utilising a two-term modified generalised Lomb-Scargle periodogram from the Astropy [185, 186] package. This not only allowed us to identify and verify the existence of significant peaks in the δ Sct frequency regime, but also to infer the rotation frequency for individual stars. The resulting periodograms are present in Fig. 5.3.

Through the analysis of *TESS* photometry, we identify HD 73857 as a high-amplitude δ Sct (HADS). These HADS occupy a sub-region of the δ Sct instability strip, and typically have only one or two excited radial modes (often corresponding to the fundamental mode and/or first overtone mode), with significantly larger peak-to-peak amplitudes than their more 'classical' counterparts [187, 188]. This is in agreement with the findings of previous articles [e.g. 189-191].

2.2 Spectropolarimetric measurements

Datasets for our sample come from a suite of spectropolarimetric instruments, including Musicos [192], Narval [50], and ESPaDOnS [49]. While the resulting spectra may vary slightly from instrument to instrument (e.g. wavelength range, resolution, signal-to-noise), the techniques utilised to reduce and analyse the data, as well as the interpretation of the results themselves, is identical in all cases.

Outside of the stars studied by collaborators in previously published articles [HD 188774,

1. https://archive.stsci.edu/missions-and-data/tess

ρ Pup, β Cas, HD 41641, HD 49198, HD 36955, and HD 63843 ; 42, 44, 94, 95, 143], each new target in our sample had a variable number of sequences available for analysis, ranging from as little as a single sequence up to 42 on the top end. For every one of them, we generated a template line mask with spectral line information retrieved from VALD [67-69], and then follow the procedure described in Chap. 1 Sec. 5.1 to generate the LSD profiles.

3 Results

3.1 Longitudinal magnetic field calculation

From the aforementioned LSD Stokes profiles, we are able to determine the strength of the magnetic field along the line of sight [71, 72]. These longitudinal magnetic field values are calculated by following the procedure detailed in Chap. 1 Sec. 5.2. The resulting B_l values are presented in Table 5.2, along with N_l values which are calculated in the same way but on the N profiles instead, and FAP algorithm results. We complete this step for each night of observation performed for a given target.

3.2 Polar magnetic field strength approximations

Using these B_l values, we can approximate the polar field strength $B_{\rm pol}$, which gives us an idea of the overall strength of the magnetic field at the surface of the star, assuming a dipolar field structure. We follow the method described in previous articles [e.g. 95, 143, 170], and detailed in Chap. 1 Sec. 5.3.

The rotation period $P_{\rm rot}$ used in our calculations has been determined from *TESS* photometry by identifying rotational modulation, i.e. a frequency peak with harmonics in Fourier space, and is extremely reliable. $v \sin i$ has been calculated from the shape of the LSD Stokes I profiles via the Fourier method, and should also represent the most reliable values for this parameter currently available. Other stellar parameters have either been taken from the literature, or retrieved from *Gaia* [76].

In the cases where we only have access to a couple of spectropolarimetric observations and a dipolar fit cannot be performed, we can nevertheless determine a lower bound of the theoretical $B_{\rm pol}$, and make the following assumptions with this in mind. First, we set $\cos(i \mp \beta) = 1$, and second we select the largest absolute value of B_l and assume it is the maximum amplitude of an eventual dipolar fit. Consequentially, if we were to acquire additional datasets for these targets, the resulting $B_{\rm pol}$ can only increase, and these values have been represented in Table 5.2 accordingly.

3.3 Correlations between field characterisation and stellar parameters

Having access to this hitherto unprecedented sample size of high fidelity magnetic δ Sct stars allows us to perform a preliminary analysis into the state of magnetism within this group of stars. To this end, we made efforts to retrieve a maximum of stellar parameters already available from the literature. This typically corresponded to effective temperature, apparent magnitude,

spectral type, and mass. In many cases however, few parameters were readily available, requiring us to take estimates from the *Gaia* DR3 archive [76], and/or determine them ourselves via scaling relations. Temperatures retrieved from *Gaia* were determined using the Extended Parameter Space for Hot Stars (ESP-HS), which provides corrections to the stellar parameters determined for stars with effective temperatures $\gtrsim 7,500$ K, which have been shown to be less reliable when determined using the standard procedures [193].

For luminosity, we used the parallax values from *Gaia* [194], in combination with Eq. 5.1 below to acquire values of absolute magnitude. We then inserted these values into the previously defined Eq. 1.3, which we recall below, to convert them into solar luminosities. This equation assumes that our stars have masses between 2 and 55 $M_\odot$, which is consistent with the fact that δ Sct are intermediate mass stars. Using the same assumption, we can also calculate masses for the few targets without values in the literature using Eq. 5.3.

$$M_v = m_v + 5(\log p + 1) \tag{5.1}$$

$$\log\left(\frac{L}{L_\odot}\right) = 0.4(4.85 - M_v) \tag{5.2}$$

$$\frac{M}{M_\odot} = \left(0.7\frac{L}{L_\odot}\right)^{2/7} \tag{5.3}$$

All the stellar parameters utilised in our study are presented in Table 5.1, with parameters taken from the literature where possible, and those that have been inferred from *Gaia* or determined via scaling relations represented by a † symbol.

Using the established values for effective temperature and luminosity, we generated the Hertzsprung-Russell (H-R) diagram displayed in Fig. 5.1. To assess their approximate evolutionary stage, we used evolutionary tracks generated with the BaSTI code [195] for the typical range of masses where we expect to observe δ Sct ($1.5 - 4.0$ $M_\odot$), using metallicity $Z = 0.062$ and no rotation. To more easily identify the evolutionary stage, the green dashed lines visible in Fig. 5.1 were generated, representing the ZAMS and TAMS respectively. The ZAMS was determined from the initial values of the models, which corresponded well with a classical mass-luminosity relation for the given parameters, and the TAMS was set to determine the time at which the mass fraction of hydrogen in the core was lower than $X_c(H) = 10^{-5}$.

We also retrieved the sample of A-F type stars from Murphy et al. [196] to use as reference, while also highlighting those amongst their sample that they classified as δ Sct. This catalogue of reference stars has hard cutoffs at 6,500 and 10,000 K, which explains why we do not see any points on the two extremities of Fig. 5.1. Murphy et al. [196] also attempts to define the red and blue edges of the δ Sct instability strip, constrained via observations, and presenting the following temperature-luminosity relations :

$$\log L_{\text{red}} = -8.11 \times 10^{-4}\, T_{\text{eff}} + 6.672 \tag{5.4}$$

$$\log L_{\text{blue}} = -1.00 \times 10^{-3}\, T_{\text{eff}} + 10.500 \tag{5.5}$$

These edges have been represented in Fig. 5.1 by the red and blue dashed lines respectively.

For all the stars in the sample, stellar ages were approximated by interpolating between the calculated BaSTI evolutionary tracks, using a 10,000-by-10,000 pixel mesh grid, and taking into account the precision on our determined values of effective temperature and luminosity. Due to the fact that quite a number of the stars in our sample are chemically peculiar (CP), presenting by definition particular variations in chemical abundances in their envelopes versus global ones, we recognise that this is not an accurate determination of age for the specific targets and *should not* be used as reference for future works. Nevertheless, in combination with their evolutionary stage inferred from their position in the H-R diagram (Fig. 5.1), it still might provide some insight into how magnetic fields might evolve over the course of stellar lifetimes in δ Sct stars.

Having now access to a wide range of stellar parameters for our sample, we sought to assess whether any correlations might exist between these parameters and the magnetic field characterisation determined through our spectropolarimetric analysis, despite our sample remaining statistically small. To this end, we generated the correlation plots shown in Fig. 5.2, where we compare $B_{\rm pol}$ with stellar mass, age, temperature, and rotational velocity.

In a similar vein, we investigated whether any correlation was visible between the strength of the magnetic field and the location of the δ Sct frequency peaks in Fourier space, generating the array of plots in Fig. 5.3. These periodograms have been pre-whitened using a two-term fit to the lower frequency domain, typically removing signals relating to rotation. While some low-frequency variability is still visible in a few cases, they do not hinder the identification of the δ Sct pulsations visible within the Fourier spectra.

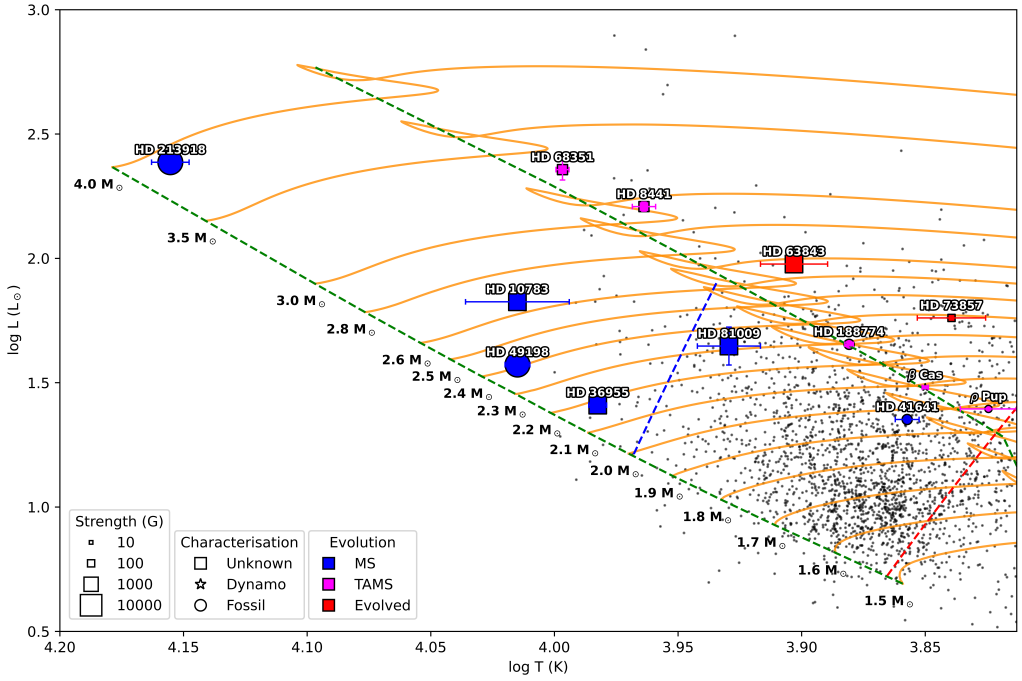

FIGURE 5.1 – Representation of the 13 confirmed magnetic δ Sct stars known to date. Orange lines correspond to BaSTI evolutionary tracks [195] for a range of stellar masses, with the ZAMS and TAMS represented with green dashed lines. The red and blue dashed lines correspond to the observationally constrained red- and blue-edge of the δ Sct instability region. Black points are δ Sct reference stars from MURPHY et al. [196].

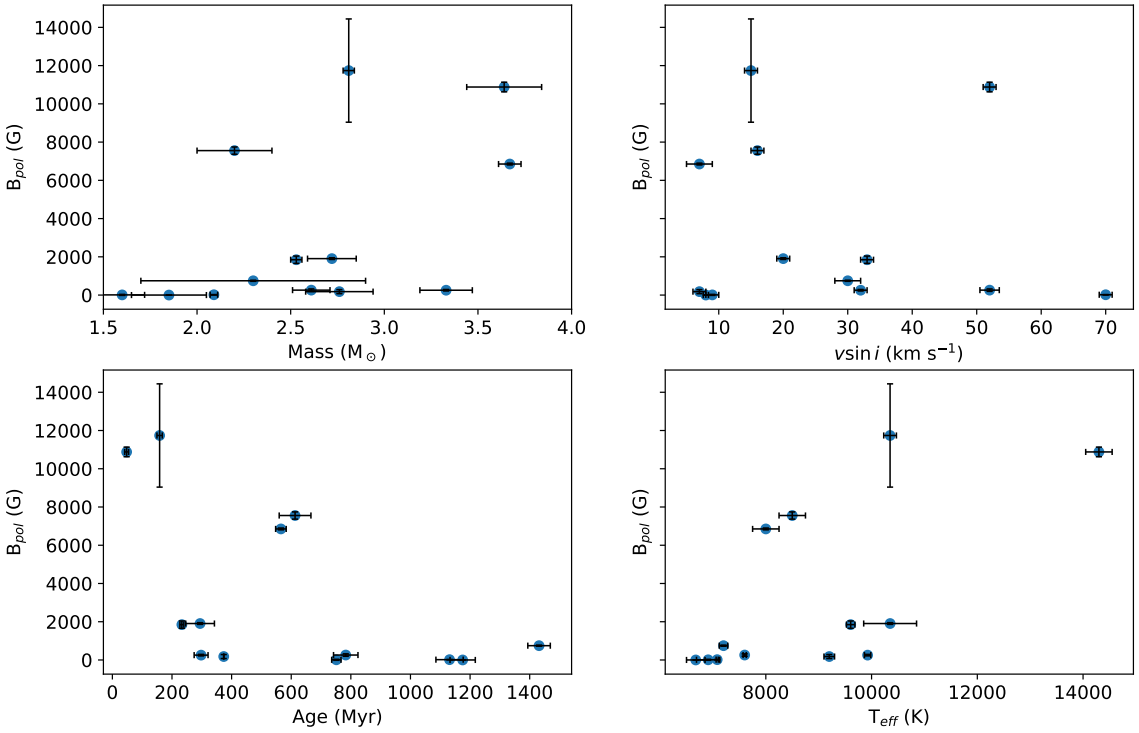

FIGURE 5.2 – Comparison plots between the polar magnetic field strength and other stellar parameters for the stars in our sample.

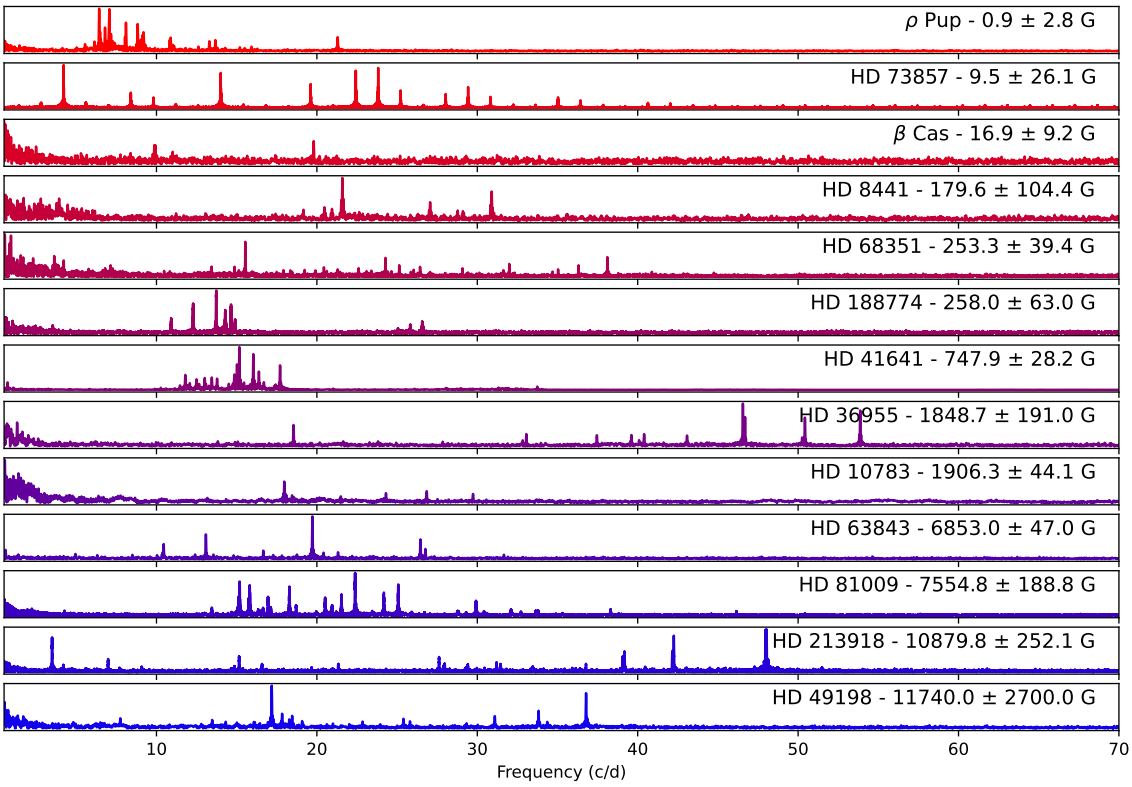

FIGURE 5.3 – Lomb-Scargle periodograms for the stars in our sample, arranged in descending order with respect to the calculated polar field strength.

ID	TIC	Spectral Type	m_v	Mass ($M_\odot$)	$v \sin i$ (km s^{-1})	$T_{\rm eff}$ (K)	Period (d)	Parallax (mas)	M_v	L ($L_\odot$)	Age (Myr)	u	$B_{\rm pol}$ (G)	Mag. field
β Cas[1]	396298498	F2III	2.27	2.09 ± 0.02	70 ± 1	7080 ± 20	0.868	59.58 ± 0.38†	1.15†	30.3 ± 0.4†	1127 ± 49†	0.5902	17 ± 9	Dynamo
HD 8441[2]	238659021	A4VpSrSi	6.68	2.76 ± 0.18	7 ± 1	9200 ± 100	69.900	3.39 ± 0.07†	-0.67†	161.5 ± 6.7†	374 ± 0†	0.5279	180 ± 104	Unknown
HD 10783[3]	257921991	A2SiCrSr	6.43	2.72 ± 0.13	20 ± 1	10351 ± 500	4.134	5.91 ± 0.09†	0.29†	66.9 ± 2†	294 ± 48†	0.4378	1906 ± 44	Unknown
HD 36955	427377135	kA1mA3V	9.58	2.3 ± 0.1†	33 ± 1	9605 ± 80†	2.284	2.23 ± 0.04†	1.33†	25.7 ± 1†	233 ± 6†	0.5279	1849 ± 191	Unknown
HD 41641[4]	436428531	A5III	7.86	2.3 ± 0.6	30 ± 2	7200 ± 80	5.615	5.27 ± 0.05†	1.47†	22.5 ± 0.5†	1433 ± 38†	0.5785	748 ± 28	Fossil
HD 49198	16485771	A0III-IVCrSi	9.31	2.56 ± 0.03†	15 ± 1	9839 ± 220†	6.224	2.10 ± 0.04†	0.92†	37.4 ± 1.4†	158 ± 9†	0.5044	11740 ± 2700	Fossil
HD 63843	35884762	A2IVSrSi	10.25	3.34 ± 0.05†	7 ± 2	8000 ± 205†	9.269	0.85 ± 0.02†	-0.09†	94.9 ± 5.2†	565 ± 18†	0.5659	6853 ± 47	Unknown
HD 68351[5]	97312819	A0VpSiCr	5.61	3.33 ± 0.14	32 ± 1	9925 ± 60	3.310	4.67 ± 0.22†	-1.04†	227.5 ± 21.8†	298 ± 23†	0.4797	253 ± 39	Unknown
HD 73857[6]	366632312	A9III	7.18	1.6 ± 0.1	9 ± 1	6909 ± 220	0.716	4.51 ± 0.03†	0.45†	57.6 ± 0.7†	751 ± 16†	0.6030	10 ± 26	Unknown
HD 81009[7]	61004258	ApEuCrSr	6.53	2.2 ± 0.2	16 ± 1	8500 ± 250	33.972	6.92 ± 0.61†	0.73†	44.4 ± 7.8†	613 ± 54†	0.5630	7555 ± 189	Unknown
HD 188774[8]	171095675	A9IV	8.81	2.61 ± 0.10	52 ± 2	7600 ± 30	2.907	2.40 ± 0.02†	0.71†	45.1 ± 0.6†	778 ± 42†	0.5916	258 ± 63	Fossil
HD 213918	128379228	B6IVpSiSrFe	8.68	3.07 ± 0.03†	52 ± 1	14297 ± 255†	1.431	2.03 ± 0.03†	0.21†	243.6 ± 8.0†	48 ± 7 †	0.4876	10880 ± 252	Fossil
ρ Pup[9]	154360594	F5IIkF2IImF5II	2.81	1.85 ± 0.20	8 ± 1	6675 ± 175	6.557	51.40 ± 0.24†	1.36†	24.8 ± 0.2†	1177 ± 44†	0.6030	0.9 ± 2.8	Fossil

TABLE 5.1 – Table of stellar parameters. Aside from those determined through our own analysis (i.e. $v \sin i$, u, $B_{\rm pol}$), parameters are retrieved from [1] ZWINTZ et al. [44], [2] NORTH et al. [197], [3] NETOPIL et al. [198], [4] ESCORZA et al. [173], [5] WRAIGHT et al. [199], [6] CASAGRANDE et al. [200], [7] WADE et al. [72], [8] LAMPENS et al. [94], [9] NEINER, WADE & SIKORA [42], or alternatively [†] inferred from *Gaia* [76].

4 Discussion

4.1 Position in H-R diagram

As seen in Fig. 5.1, our sample probes a large area of the H-R diagram, covering a variety of stellar masses and ages, which in turn assists in our attempts to study the global picture of magnetism within the family of δ Sct stars. This includes stars on the main sequence and stars evolving beyond.

Our sample extends well beyond the blue-edge of the δ Sct instability strip, constrained via observations from Murphy et al. [196]. Indeed, our sample includes numerous early-A types, as well as a B6 (HD 213918), all of which are on the hotter edge for the temperatures typically observed in δ Sct stars. On the red-edge of this sample, we see an apparent dearth of magnetic candidates with luminosities lower than $L \sim 1.3\ L_{\odot}$. This appears to conflict somewhat with the representation of δ Sct stars from Murphy et al. [196], where the majority of their reference stars are dimmer and cooler. Additionally, the few stars closest to the red edge present comparatively weak fields (ρ Pup, β Cas, and HD 41641), with some presenting complexity that would be consistent with local dynamo fields often found in lower mass stars.

This could suggest that δ Sct stars with strong ($\gtrsim 1$ kG) magnetic fields are typically located at the hotter edge of the δ Sct instability strip. That is to say, that they are amongst the most massive and most luminous stars in the typical A-F spectral range. One should consider the fact that we are observationally biased towards hotter stars, as they are the most likely to present strong (likely fossil) magnetic fields that are relatively easy to detect, as opposed to the weak and ultra-weak fields we sometimes observe in cooler stars (e.g. ρ Pup).

That being said, we would expect stars that present weak, dynamo-generated, fields to be located in the region pertaining to stars with the lowest masses, as their internal structure more closely resembles that of low-mass stars, i.e. with convective envelopes or at least large regions associated with partial ionisation layers of hydrogen and helium. Looking at the scale of magnetic field strengths in our sample, this appears to be consistent, as the majority of the lower mass stars presented herein have globally weaker fields.

We also observe that a significant portion of our sample are more evolved stars, located at or near the TAMS, or at the start of the subgiant branch. Due to conservation of magnetic flux, we expect more evolved stars to present weaker fields on average than those on the main sequence : while the magnetic field strength remains roughly the same, the envelope cools and expands, and as such the strength of the magnetic field we can detect at the surface decreases significantly. An additional magnetic field decay has also been observed [12-14]. As with the previous point, this theory appears to also hold true in our sample (see also Fig. 5.2), save for the case of HD 63843 which is uncharacteristically strong in comparison. One thing to note is that the BaSTI tracks we have plotted in Fig. 5.1 do not take into account magnetic fields. While the full impact of magnetic fields on stellar evolution is not entirely clear, some studies suggest that magnetism decreases a star's main-sequence lifetime by impacting rotation rates, chemical mixing and stellar winds [30, 33, 201]. As a result, a star containing a magnetic field would be more evolved than one without a field at the same age.

4.2 Stellar mass regimes

At low masses, we expect to be in a regime of stars predominantly presenting weak dynamo fields, as opposed to the strong fossil fields we observe at higher masses. We should therefore see a 'ramp-up' of the strength of polar magnetic fields in the intermediate region. Aside from the outlier at 2.2 $M_\odot$, corresponding to HD 81009, this is essentially what we observe in our sample. Since stellar mass and effective temperature are intrinsically linked, we see something similar for the $T_{\rm eff}$ plot, in that hotter stars are more likely to host stronger magnetic fields. We note however that four stars in our sample have $T_{\rm eff} \gtrsim 10,000$ K, which is unusual for δ Sct. Theoretical studies have shown that rotation impacts the width and location of the κ-mechanism instability region of δ Sct stars, shifting it toward higher luminosities and effective temperatures [108, 202], which might help to explain this offset.

We also compare in Fig. 5.3 our $B_{\rm pol}$ values with the frequency peaks visible in the periodograms of the stars in our sample. Theoretically, the excitation of the κ-mechanism can be described via a work integral with two sets of parameters : a first set that describes the equilibrium state of the star's internal structure, and a second that quantifies the oscillations themselves. While under the presence of a magnetic field, there are two possible impacts :

— either the structure of the star – including factors pertaining to its thermodynamic equilibrium such as density, pressure, and temperature – is modified, in particular if the excitation region is close to the surface,

— or the oscillation modes and their associated quantities (e.g. amplitude, order) are modified.

In either case, the presence of a magnetic field should have a measurable impact, with the modification of the star's structure being proportional to B^2 and thus so too the excitation of the δ Sct modes. As such, we would expect to see a gradual increase in the frequency range within which are location the δ Sct frequencies with respect to growing values of $B_{\rm pol}$, as the depth of the instability region is linked to the frequency range in which we can observe pulsations. This correlation is not particularly visible in Fig. 5.3, which suggests that magnetism is not the only ingredient in the determination of the position of δ Sct frequencies. It should also be emphasised that for many of our targets, only a single spectropolarimetric dataset was available, making the calculation of $B_{\rm pol}$ correspond to a lower-bound rather than a true assessment. As such, should additional datasets become available, and the corresponding $B_{\rm pol}$ values prove to increase as a result, the order in which these stars are displayed could change and thus potentially reveal such a trend.

4.3 Effect of rotation

With regards to $v \sin i$, an initial assessment suggests a trend of faster rotators leaning towards lower $B_{\rm pol}$ values, ignoring the apparent outlier at 52 km s^{-1} which corresponds to HD 213918. It should be noted, however, that we are biased in the $v \sin i$ of stars in our sample. We detect weak fields at a wide range of $v \sin i$ values, which shows that our spectropolarimetric observations achieved sufficient sensitivity to be able to detect weak fields for all our targets. We also managed to detect a number of stronger fields, but with only four such targets we are

unable to conclude with regards to the distribution of these strong fields with respect to $v \sin i$. Undoubtedly, additional targets are required to test to what extent this trend remains true, ideally with at least a few higher velocity examples ($v \sin i > 100$ km s^{-1}).

5 Conclusion

We present a curated list of 13 magnetic δ Sct stars, assembled from a variety of sources, and confirm both their identification as δ Sct as well as the presence of a magnetic field. This constitutes the most comprehensive list of these objects to date, with the expectation that it will continue to be expanded upon as the authors and members of the community pursue studies in this field.

Being the start of a statistically significant database, we have sought to identify whether any trends might be observed within this sample, by considering their positions in the H-R diagram relative to each other and other 'classical' stars, as well as comparing the polar magnetic field strength values calculated as part of this study with the sample's stellar parameters.

We observe that our sample is overall shifted towards higher temperatures, luminosities and thus masses, with respect to a sample of A-F type reference stars and the observationally constrained δ Sct instability strip. This could be due to the impact of the magnetic field on the δ Sct pulsation excitation, shifting these pulsations to hotter stars. A significant portion of our sample also appears to be slightly evolved stars, having reached the TAMS or progressed beyond the main-sequence. Finally, stars presenting the strongest polar magnetic fields are amongst the hottest in our sample, as expected from fossil versus dynamo fields.

When comparing with stellar parameters, we observe behaviour that is generally consistent with theory, but note that there exists several observational biases in the parameter space of our sample. The latter is skewed towards targets with lower $v \sin i$ values, which reduces the required exposure time of spectropolarimetric observations, and hotter effective temperatures, which are more likely to present strong magnetic fields and thus are also easier to detect.

Finally, despite being predicted by theory, we do not see a clear correlation between surface magnetic field strength and the location of δ Sct peaks in Fourier space. This suggests that stellar magnetism is not the sole ingredient for the differences in position and spacing of δ Sct frequencies.

While the list of magnetic δ Sct stars presented here remains relatively small, it is the first study of its kind for δ Sct stars, and will hopefully pave the way for subsequent studies into the interplay between stellar magnetism and pulsating variable stars.

ID	TIC	Obs date	Mid-HJD -2451000	Instrument	Strategy ($N \times 4 \times s$)	Mean λ (nm)	Mean Lande	FAP FAP	$B_l \pm \sigma B$ (G)	$N_l \pm \sigma N$ (G)	$B_{pol} \pm \sigma B$ (G)	Characterisation
β Cas	396298498	2013-11-03	5600.2627	Narval	1x4x65	528.7963	1.199	ND	0.6 ± 6.6	-1.1 ± 6.6	16.9 ± 9.2	Dynamo
		2014-09-24	5925.6165	Narval	3x4x65	523.7686	1.200	MD	1.3 ± 2.5	-4.6 ± 2.5		
		2014-12-19	6011.2941	Narval	5x4x65	522.2549	1.200	DD	3.9 ± 1.9	0.0 ± 2.0		
		2014-12-21	6013.2990	Narval	5x4x65	524.663	1.200	DD	0.8 ± 2.1	1.4 ± 2.1		
		2015-12-01	6358.3578	Narval	10x4x65	528.0618	1.200	DD	0.6 ± 2.6	1.6 ± 2.6		
		2015-12-02	6359.3592	Narval	10x4x65	526.2186	1.200	MD	-1.5 ± 3.2	2.1 ± 3.2		
		2015-12-05	6362.2862	Narval	5x4x65	527.7356	1.200	MD	-3.5 ± 2.6	-1.3 ± 2.6		
		2015-12-06	6363.3513	Narval	15x4x65	524.9052	1.200	DD	-0.7 ± 2.1	-0.7 ± 2.1		
		2015-12-07	6364.3792	Narval	10x4x65	523.9241	1.201	MD	-3.5 ± 2.2	0.9 ± 2.2		
		2015-12-09	6366.3073	Narval	5x4x65	535.774	1.200	DD	3.4 ± 2.6	-3.9 ± 2.6		
		2015-12-11	6368.3693	Narval	5x4x65	527.5769	1.200	DD	2.8 ± 2.2	-1.8 ± 2.3		
		2015-12-12	6369.3464	Narval	10x4x65	526.3156	1.201	DD	-0.6 ± 2.6	-1 ± 2.6		
		2015-12-13	6370.3799	Narval	5x4x65	529.2903	1.200	ND	1.7 ± 2.4	-2.7 ± 2.4		
HD 8441	238659021	2004-07-30	2217.6484	Musicos	1x4x800	529.8070	1.202	MD	-3 ± 32	43 ± 32	>180 ± 104	Unknown
		2004-09-31	2249.6704	Musicos	1x4x600	530.7108	1.201	DD	56 ± 33	-53 ± 33		
HD 10783	257921991	2018-12-23	7476.7128	ESPaDOnS	1x4x168	531.4009	1.198	DD	-574 ± 13	-3 ± 9	>1906 ± 44	Unknown
		2018-12-24	7477.7373	ESPaDOnS	1x4x168	531.9343	1.198	DD	458 ± 25	0 ± 9		
HD 36955	427377135	2021-09-01	8460.0706	ESPaDOnS	1x4x656	526.7640	1.208	DD	-581 ± 60	35 ± 58	>1849 ± 191	Unknown
HD 41641	436428531	2015-10-21	6317.6957	Narval	8x4x27	532.0358	1.188	ND	438 ± 145	330 ± 145	748 ± 28	Dipole fossil
		2015-11-09	6336.7578	Narval	3x4x27	535.7854	1.191	ND	-175 ± 117	-100 ± 117		
		2015-11-11	6338.7326	Narval	5x4x27	533.5284	1.190	ND	-3 ± 100	-29 ± 100		
		2015-11-12	6339.7545	Narval	8x4x27	531.8484	1.190	DD	226 ± 61	40 ± 61		
		2015-11-16	6343.6598	Narval	8x4x27	530.9734	1.190	ND	-161 ± 84	-16 ± 84		
		2016-03-15	6463.3385	Narval	8x4x27	557.8794	1.186	ND	95 ± 205	-85 ± 205		
		2016-03-20	6468.3606	Narval	7x4x27	530.4079	1.192	ND	47 ± 58	19 ± 58		
		2016-10-08	6670.6344	Narval	10x4x27	528.7043	1.190	DD	-40 ± 55	-6 ± 55		
		2016-10-27	6689.5768	Narval	10x4x27	545.8406	1.185	DD	49 ± 255	-105 ± 255		
		2016-10-28	6690.7036	Narval	10x4x27	541.0206	1.188	DD	-123 ± 94	-45 ± 94		
		2016-10-29	6691.6058	Narval	10x4x27	537.2884	1.189	MD	-258 ± 112	27 ± 112		
		2016-10-30	6692.7331	Narval	10x4x27	536.8760	1.189	DD	-3 ± 79	-85 ± 79		
		2016-10-31	6693.6274	Narval	10x4x27	527.2550	1.191	DD	227 ± 55	73 ± 55		
		2016-11-02	6695.6581	Narval	10x4x27	528.4211	1.190	DD	-97 ± 75	-146 ± 75		
		2016-11-25	6718.6306	Narval	10x4x27	542.8027	1.188	DD	-124 ± 75	-6 ± 75		
		2016-12-01	6724.4852	Narval	10x4x27	537.2719	1.189	DD	-143 ± 95	72 ± 95		
		2016-12-02	6725.6170	Narval	10x4x27	524.5040	1.192	DD	-195 ± 54	-30 ± 54		
		2023-10-19	9238.0503	ESPaDOnS	30x4x21	521.7209	1.195	DD	263 ± 16	28 ± 16		
		2023-10-20	9239.0633	ESPaDOnS	30x4x22	519.1949	1.196	DD	71 ± 12	-4 ± 12		
		2023-10-24	9242.9876	ESPaDOnS	30x4x23	527.5646	1.195	DD	159 ± 16	7 ± 16		
		2023-10-25	9244.0024	ESPaDOnS	15x4x24	518.926	1.196	DD	258 ± 21	-2 ± 21		
		2023-12-01	9280.9651	ESPaDOnS	30x4x25	524.8393	1.194	DD	-75 ± 19	-58 ± 19		
		2023-12-03	9282.9843	ESPaDOnS	30x4x26	522.4993	1.195	DD	255 ± 15	18 ± 15		
		2023-12-29	9308.9267	ESPaDOnS	30x4x27	521.7346	1.195	DD	-130 ± 14	0 ± 14		
		2023-12-30	9309.9050	ESPaDOnS	30x4x28	521.2746	1.195	DD	92 ± 13	2 ± 13		
		2023-12-31	9310.8843	ESPaDOnS	45x4x29	518.6848	1.196	DD	228 ± 12	-3 ± 12		
		2024-01-01	9311.8886	ESPaDOnS	30x4x30	520.0929	1.196	DD	92 ± 13	-30 ± 13		
		2024-01-02	9312.8903	ESPaDOnS	30x4x31	520.8373	1.195	DD	-90 ± 13	-16 ± 13		
		2024-01-03	9313.9474	ESPaDOnS	30x4x32	531.2326	1.193	DD	-230 ± 20	24 ± 20		
		2024-01-05	9315.9062	ESPaDOnS	30x4x33	529.1782	1.194	DD	198 ± 20	14 ± 20		
		2024-01-06	9316.7739	ESPaDOnS	15x4x34	519.3949	1.196	DD	293 ± 20	-11 ± 20		
		2024-01-07	9317.9476	ESPaDOnS	30x4x35	518.9205	1.196	DD	10 ± 13	15 ± 13		
		2024-01-15	9325.8939	ESPaDOnS	30x4x36	526.3133	1.195	DD	-116 ± 16	-8 ± 16		
HD 49198	16485771	2021-11-26	8545.8924	ESPaDOnS	1x4x319	525.9691	1.206	DD	-1065 ± 59	-56 ± 50	11740 ± 2700	Dipolar
		2021-11-27	8547.0635	ESPaDOnS	1x4x319	524.0390	1.206	DD	-2386 ± 72	-26 ± 41		
		2022-02-18	8629.9653	ESPaDOnS	1x4x319	527.5670	1.205	DD	-2841 ± 70	-50 ± 38		
		2022-02-21	8632.8058	ESPaDOnS	1x4x319	523.3311	1.206	DD	-947 ± 44	41 ± 35		
		2022-02-22	8633.9703	ESPaDOnS	1x4x319	528.3550	1.205	DD	-2115 ± 70	40 ± 45		
HD 63843	35884762	2024-01-18	9329.0059	ESPaDOnS	1x4x280	526.3450	1.189	DD	2191 ± 15	5 ± 10	>6853 ± 47	Unknown
HD 68351	97312819	2012-12-23	5286.1349	ESPaDOnS	1x4x230	517.1605	1.205	DD	43 ± 8	-11 ± 9	>253 ± 39	Unknown
		2012-12-25	5288.1286	ESPaDOnS	1x4x230	517.5697	1.205	DD	78 ± 12	7 ± 12		
HD 73857	366632312	2018-04-18	7227.3810	Narval	1x4x900	541.1414	1.191	DD	-3.1 ± 8.5	13.4 ± 8.6	>10 ± 26	Unknown
HD 81009	61004258	1999-01-14	193.6448	Musicos	1x4x360	532.6345	1.196	DD	2412 ± 60	-15 ± 34	>7555 ± 189	Unknown
HD 188774	171095675	2014-09-06	5907.9513	ESPaDOnS	1x4x840	518.4316	1.195	MD	26 ± 12	-4 ± 13	258 ± 63	Dipolar
		2015-07-22	6227.0266	ESPaDOnS	10x4x129	516.4880	1.196	DD	53 ± 9	0 ± 9		
		2015-07-23	6227.9747	ESPaDOnS	10x4x129	515.8201	1.197	DD	28 ± 10	3 ± 10		
		2015-07-24	6228.8548	ESPaDOnS	10x4x129	516.0640	1.196	DD	-55 ± 9	-9 ± 9		
		2015-07-25	6229.9179	ESPaDOnS	20x4x129	519.1700	1.195	MD	55 ± 10	-8 ± 10		
		2015-07-27	6232.0566	ESPaDOnS	10x4x129	519.7395	1.195	DD	-36 ± 11	-6 ± 11		
		2015-07-28	6232.9331	ESPaDOnS	15x4x129	517.2552	1.196	DD	72 ± 10	-9 ± 10		
		2015-07-31	6236.0300	ESPaDOnS	10x4x129	519.5260	1.195	DD	84 ± 10	-9 ± 10		
		2015-08-04	6240.0195	ESPaDOnS	4x4x129	521.6588	1.195	MD	14 ± 22	-32 ± 22		
HD 213918	128379228	2012-11-25	5257.7631	ESPaDOnS	3x4x900	518.9928	1.203	DD	857 ± 85	65 ± 82	10880 ± 252	Quadrupolar
		2012-11-28	5260.7471	ESPaDOnS	1x4x900	519.6083	1.203	DD	-599 ± 64	42 ± 58		
		2012-11-29	5261.7982	ESPaDOnS	2x4x900	519.7885	1.203	DD	1605 ± 99	26 ± 98		
		2012-12-03	5265.7077	ESPaDOnS	1x4x900	520.7785	1.203	DD	3353 ± 78	-42 ± 70		
		2012-12-06	5268.7126	ESPaDOnS	1x4x900	520.1573	1.203	DD	2905 ± 74	84 ± 67		
ρ Pup	154360594	2014-02-09	5698.8667	ESPaDOnS	2x4x30	548.9392	1.187	ND	-0.1 ± 1	-0.3 ± 1	0.9 ± 2.8	UW fossil
		2015-10-30	6327.1443	ESPaDOnS	8x4x25	541.0814	1.188	DD	-0.3 ± 0.9	0.4 ± 0.9		

TABLE 5.2 – Summary of spectropolarimetric observations for the sample.

Chapter 6

Conclusion and outlook

1 Conclusions

Over the course of this thesis work, I have investigated the state of magnetism within the family of pulsating variable stars known as δ Sct. Progress has been achieved through both broad surveys and individual case studies, and the techniques used for identifying and characterising these stars have made significant advances as a result.

While rotational modulation has often been utilised as a reliable indicator of the presence of magnetism [59], my studies suggest that in the case of δ Sct (and indeed likely other pulsating variable stars) we need to include additional indicators in order to achieve a high magnetic field detection rate, such as in previous surveys. Indeed, as we have previously seen, there is a significant amount of overlap between pulsating variables and CP stars, and an even greater overlap between magnetic stars and CP stars. Sure enough, the chemical spots visible in their photometric light curves helps us to identify the rotational modulation signal which has historically been proven to be a reliable indicator for magnetism. We can combine this with other features such as the 5200 Å depression in the spectra of stars containing both chemical peculiarities and pulsation modes as an additional *a priori* indicator for magnetism in these stars. This is a very powerful result, and one I expect will come into play for future surveys of variable stars presenting chemical peculiarities.

As a result of my work in this field, we have progressed from having only three known magnetic δ Sct to now being in a position of having 13.

This started with the study of a single promising candidate in Thomson-Paressant et al. [95] (2020), HD 41641, from which followed a number of broad scale surveys. While this first survey did not yield the results we hoped, it provided some valuable insight and as a result the subsequent survey was much more successful.

Thomson-Paressant et al. [86] (2023) seemed to suggest that the representation of magnetism in δ Sct stars was less than the 10% reported by previous studies of non-variable A-type stars [59], having found no clear signals consistent with surface magnetic fields amongst a sample of 'ideal' candidates.

Thomson-Paressant, Neiner & Labadie-Bartz [143] (2024) demonstrated the reliability of the 5200 Å depression as an indicator for the presence of magnetism which, when combined with rotational modulation, is a powerful tool in our arsenal for identifying new candidate magnetic pulsating stars (including but not limited to δ Sct), and perhaps more importantly led to the expansion of the list of confirmed magnetic δ Sct by adding three new members.

By combining studies together from a variety of sources, I was able to further develop this list in Thomson-Paressant et al. (in prep.), reaching a new total of 13 targets. This work included stars that had been confirmed as possessing a magnetic field, but were as of yet unknown to display δ Sct pulsations, and inversely, others that were well known δ Sct for which I characterised the magnetic field via spectropolarimetry.

When considering the full breadth of confirmed magnetic δ Sct as the list stands today, there are a few interesting features that seem to appear. By comparing the positions in the H-R diagram of this subset of 13 stars with other 'classical' δ Sct stars, we observe that this sample is shifted towards higher temperatures, luminosities, and masses by proxy, with respect to typical A-F type stars. This suggests that magnetism has an import effect on the internal structure of these stars, such as shifting the location of the δ Sct pulsation excitation region, as well as the evolution of these stars, by accelerating their evolution compared to similar non-magnetic stars.

If we compare the stellar parameters of this sample with their magnetic field strengths at the surface, we do not observe any particularly unusual behaviour, but recognise that there exists a number of observational biases in the representation of the sample. Due to constraints provided by spectropolarimetry, we have a tendency to target slowly rotating and hotter/more luminous stars, as they generally require less telescope time and their rate of detection is higher due to typically stronger fields.

Finally, by analysing the location of δ Sct peaks in Fourier space with respect to the magnetic field strength, we do not see a clear trend. This suggests that while the stellar magnetic field does impact the location of the instability (as predicted by theory), it is not the only factor, and that there are ingredients missing to be able to reliably predict where these pulsational frequencies should be located.

2 Outlook and future perspectives

Thanks to the work presented here, the field of magnetism in δ Sct stars has made significant progress in recent years. The path forward in order to make further advances and achieve greater insight is now clear.

As mentioned above, we are aware of the observational biases present in the list of 13 confirmed magnetic δ Sct stars, and it would prove beneficial to minimise the impacts of these biases by attempting to expand our search field and parameter space. Since telescope time is a precious resource, effort should be made to maximise the likelihood that any 'less easy' magnetic candidate that is proposed presents a strong case for the presence of magnetism (e.g. a star with both rotational modulation and the 5200 Å depression).

Already I have a number of telescope proposals submitted and in progress, which will likely

lead to a suite of new targets that can be eventually added to the list. I am also in charge of the δ Sct component in an international large program at CFHT called MAESTROS which, if successful, will lead to the detection and characterisation of magnetic fields of dozens of candidates across the full spectrum of pulsating variable stars.

Over the next few years, while I am eager to continue contributing and making discoveries for δ Sct, I am also very interested to investigate the intersections between the δ Sct regime with those of other pulsating variable stars, such as γ Dor and SPB stars. While they are currently characterised as distinct groups, the mechanisms in play that generate the observed pulsations and the conditions under which these instabilities occur are not yet well understood, and as such the boundaries between groups could reveal some very interesting physics. In addition, since in some areas their instability strips overlap, giving rise to hybrid pulsators (e.g. δ Sct-γ Dor hybrids), characterising the magnetic fields in such objects would provide even more stringent constraints on asteroseismic models than either type of pulsator individually.

As the number of well-studied magnetic δ Sct stars continues to grow, the next step in this process is to perform magneto-asteroseismic modelling in order to study the interiors of these stars, an aspect that I am keen to get involved in. As described in the beginning of this thesis, combining the information gathered from magnetic and pulsational analysis provides very strict constraints on how stellar interiors are structured, which in turn provides insight into stellar physics. Having now access to hundreds of spectropolarimetric datasets for HD 41641, for example, this is a perfect candidate for performing this exact type of analysis, and it would be the logical progression to my previous studies on this star. I will endeavour to perform similar spectropolarimetric follow-up and asteroseismic analysis of the various targets of the list of 13 confirmed magnetic δ Sct presented herein, and I am certain that additional targets are likely to follow in the near future as well.

With the launch of the *PLAnetary Transits and Oscillations of stars* (*PLATO*) space satellite planned for the end of 2026, it is a critical time to identify magnetic candidates within its observation fields. Indeed, its first long-duration field of view has been decided, and target lists of all the pulsating variable stars in this field that display rotational modulation in their *TESS* photometric light curves have been established by my colleagues at the Paris Observatory and myself. While *TESS* has proven to be an extremely well-suited tool for detecting stellar pulsations, it suffers from poor frequency resolution which makes it less well designed for asteroseismic analysis, particularly when the pulsation modes are closely spaced. Contrarily, targets observed with *PLATO* are much brighter than *TESS* or *Kepler* targets, i.e. more easily observed with spectropolarimetry, and will be perfect for this sort of study. It is therefore essential to know in advance which targets within the field should be observed.

Appendix A

A new NeoNarval data reduction pipeline with PyReduce

Objectives

Following the upgrade of the Narval instrument at TBL to NeoNarval, concerns have been raised regarding the quality of results in polarimetry and precision in velocimetry. Investigations into the topic have hinted at both instrumental and software issues that must be resolved in order to accurately exploit the data. We present our discoveries of issues and subsequent work performed to improve the reduction of NeoNarval data. We aim to provide comparisons between the DRS and a pipeline utilised for similar instruments, as well as initial attempts to implement new methods. PyReduce, an open-source reduction pipeline for echelle spectrographs, has modules already designed for a variety of currently-used instruments as well as initialisation of a number of options allowing for the evolution and expansion of its functions, which is of great benefit for integrating the specifics of the NeoNarval instrument.

Work based on Thomson-Paressant et al., SF2A 2023 Proceedings [54] ; and Gutteridge et al. (in prep.).

1 Introduction

As mentioned briefly in Sec. 1.3, I have been working on developing a spectropolarimetric version of PyReduce [203], constituting a new dedicated data reduction pipeline for the NeoNarval instrument, as a complimentary project to my main thesis work. The eventual success of this project has positive impacts on both the scientific community, by providing a reliable alternative to the *Data Reduction Software* (DRS) currently used at TBL, and my own interests, being able to properly exploit the numerous datasets that have been taken with this sub-optimal instrument.

While PyReduce already existed in some form before C. Gutteridge and myself discovered it, it has not been under active development by the original authors in some time and has been made open access to anyone who might benefit from its functionality. The initial goal of this code was to be a direct port to Python of the IDL code of the same name, Reduce, and had been developed such that it could be applied to spectroscopic data coming from a wide range of echelle spectrographs already in operation (e.g. UVES, HARPS, XSHOOTER, etc.). Additionally, it had been designed in such a way that polarimetric methods could eventually be implemented, though no such progress had been achieved by the time we began with this project.

As a result, our current goal is to implement these polarimetric methods, while trying to maintain as much of the underlying code and function already in existence, so that we can expand the list of instrument configurations to include NeoNarval first and foremost, but eventually all spectropolarimetric instruments currently in operation.

Over the next couple of sections, I will describe my own personal contributions to this project. The full extent of this work can be viewed in Thomson-Paressant et al. [54] and Gutteridge et al. (in prep.).

2 New and updated algorithms for PyReduce

2.1 Background scatter subtraction

When looking at the raw NeoNarval data files, it becomes quickly apparent that there is flux that appears between the spectral orders. This is a result of scattered light inside the instrument, and causes issues when attempting to determine the flux ratio in each order as it contributes unevenly across the beams. This feature is particularly visible when looking at the flat-field calibration files, as the overall flux in the image is larger, and so too is the amount of scattered light, but it is also present in all illuminated exposures.

To resolve this issue, we utilise a window function that runs perpendicular to the orders to search for local minima. These minima correspond to the zero-points between orders, from which we can perform a 2D fit over the entire image to determine the overall contribution of background scatter to the image. We utilise a linear combination of four Gaussian profiles, as this was the most consistently performing shape. A least-squares algorithm determines the best fit parameters, which we then use to subtract the fit from the image.

We first perform this fit to the flat-fields, then apply the given parameters as a first guess for the fit on the science files. While the amplitude will differ, the overall shape of the function should remain roughly constant. As an example, a 2D slice of this fit is shown in Fig. A.1. One should note that the NeoNarval DRS currently only performs this step on science files and not on the calibration files, which demonstrably has detrimental effects on the calibration process.

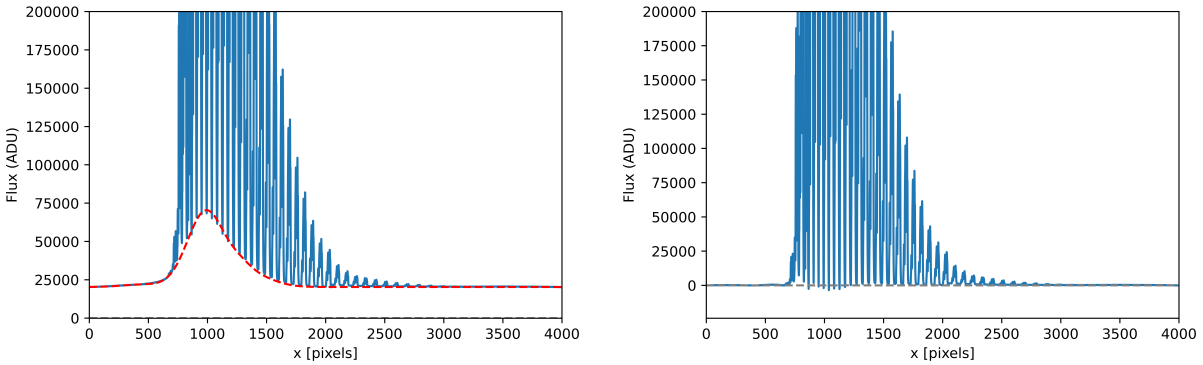

(a) (b)

FIGURE A.1 – Slice of a CCD image perpendicular to the orders (blue), before (a) and after (b) subtraction of the fit to the background scatter (red).

2.2 Order extraction

Illuminated images taken by NeoNarval exhibit curved spectral orders consisting of two beams, one for each perpendicular polarisation state. Unfortunately, there is a slight overlap in the areas illuminated by each beam. While this is not an issue for spectroscopy, it is problematic in polarimetry, as one polarisation state pollutes the other. We therefore opted to design a new extraction algorithm to minimise the contribution of each beam to the other.

Each beam is split into three separate peaks due to the slicer it passes through. The central peak of each beam is the brightest, and one (and always the same one) of the side lobes is brighter than the other. Looking at Fig. A.2a, we can see that a simple double-Gaussian profile does a poor job of fitting these peaks, and that rather two sets of three Gaussians (labelled 'Hex Gaussian') is a much more accurate representation. This can be extrapolated quite easily to two-dimensions to fit the two beams of an entire order at once, as seen in Fig. A.2b. There is still some flux visible in the residuals, primarily due to the column-by-column way that the orders are straightened. There are efforts currently ongoing to move to a sub-pixel grid to increase the smoothness of the order straightening, which will further improve the precision of the fit.

Once the fit to the flat-corrected science files has been determined, we can then exclude all pixels between the two beams with $\geq$5% contribution from both beams. Typically, this corresponds to an exclusion region of up to three columns (out of $\sim$ 40 columns per order). We have made a point to conserve the flux information contained in this exclusion region, as although it has detrimental effects for polarimetry it is beneficial for those looking to study spectroscopy and in particular velocimetry, where maximising the amount of flux is important.

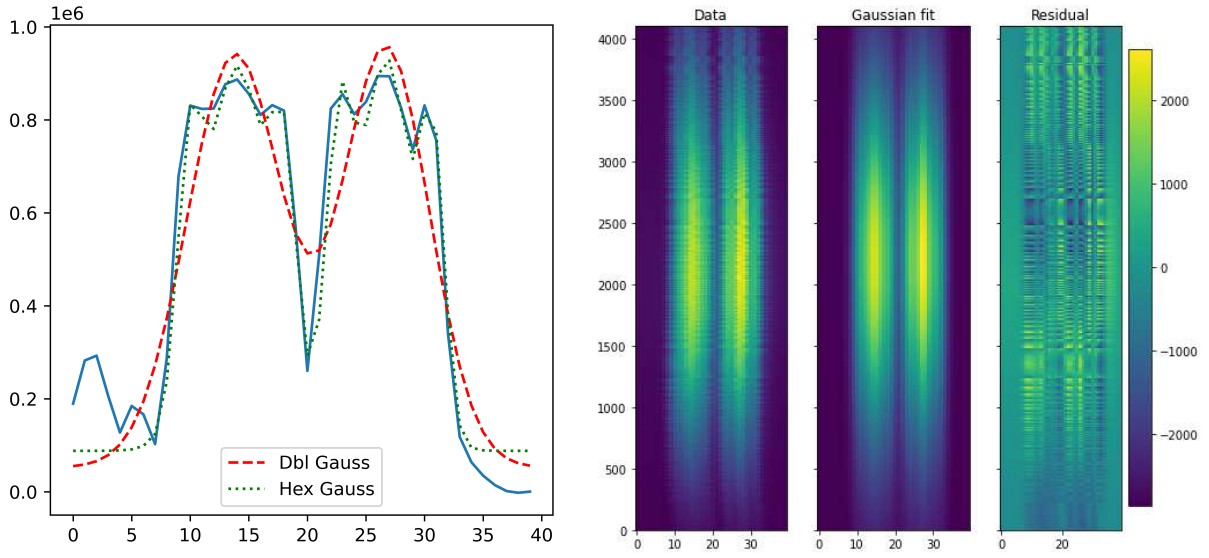

(a) (b)

FIGURE A.2 – Gaussian fits to the two beams of a given order, **a)** in one dimension and **b)** in two dimensions. The latter also provides the residuals of the fit to the data, with corresponding value range.

2.3 Normalised flat field

Once the master flats have been generated, one for each distinct exposure time generated, we need to define the blaze function which operates as a set of normalising weights for 'smoothing' the overall shape of each spectral order across the CCD. Since the shape of each of the two beams for a given order can vary slightly, an individual blaze function for each beam of each order must be generated.

It has been established that the gain of the instrument is not constant, as subtracting one bias-subtracted flat from another from consecutive nights for the same exposure time results in a non-null image. Additionally, due to the instrument operating in a four-amplifier mode for reading out the detector, we observe a variation in gain for each quadrant that is not constant. Even by subtracting the bias from the flats and science files, an offset remains at the juncture between quadrants. Only a single gain value is provided in the header of the files, so this offset cannot be easily resolved, and would require calculations of the gain on a quadrant-by-quadrant as well as file-by-file basis.

As a result, in order to calculate the best fitting blaze function, the spectrum extracted from the orders of the master flat needs to be fit in two sections : one for each quadrant the spectral order passes through. There are a couple of orders at the centre of the CCD that can pass through all four quadrants, but due to the curvature of the orders and the flux levels at those points the effect is negligible.

The fit to each 'half' of the beam is done using a third order polynomial, which we found to be the most reliable method to trace the shape without being overly sensitive to small scale variability. The two halves of our blaze function is then normalised, by dividing it by the maximum,

to end up with a set of weights between 0 and 1, which can then be applied to the extracted spectra for the science files.

Since this reduction step occurs after the tracing and straightening of the orders, we can select which master flat we extract each order from, allowing us to maximise the expression of the typically weaker red orders without saturating the blue ones.

3 Conclusion

We are implementing polarimetry into PyReduce, with new and improved methods for e.g. order tracing, blending removal, background scatter subtraction, wavelength calibration, and Stokes profiles generation. Here, we present preliminary results of our efforts to integrate some of these into the software, taking into account the specific configuration of the NeoNarval instrument. While these newly introduced algorithms are designed specifically to mitigate the instrumental effects of NeoNarval, they can also be applied to any other spectropolarimeter, and we hope to fully integrate this aspect into PyReduce's functionality eventually.

PyReduce produces encouraging results, though there is still work to be done in order to accurately and precisely exploit the spectropolarimetric data coming from NeoNarval. The next steps in this process are :

— Consider vignetting at the extremities of each order to prevent error being introduced into the order tracing and background scatter steps.

— Transition from the rigid pixel grid currently in operation to a non-linear grid to improve precision of order tracing.

— Integrate 2D wavelength calibration, to be performed on each polarisation state separately.

— Implement multi-threading/parallelisation for the most computationally expensive steps, particularly the various fitting steps such as background scatter and inter-beam exclusion.

— Ensure universality/portability of packages for Python 3.X, so that the code operates on a maximum of devices.

We emphasise that the implementation of these methods into PyReduce will not solve the instrumental problems, but rather will help to diagnose such issues and improve the operation of the instrument as a whole, while maximising the quality of both past and future reduced data. Further investigations into how to improve the instrument must continue, as post-production solutions almost always result in a loss of signal which is not an efficient use of the instrument. It also results in a longer computation time for producing the reduced data.

The branch of PyReduce that we are currently working on is not yet openly available, but will be open access in the near future, with the hopes that other members of the community can contribute to its operation and improve its function.

Appendix B

LSD profiles for mCP stars

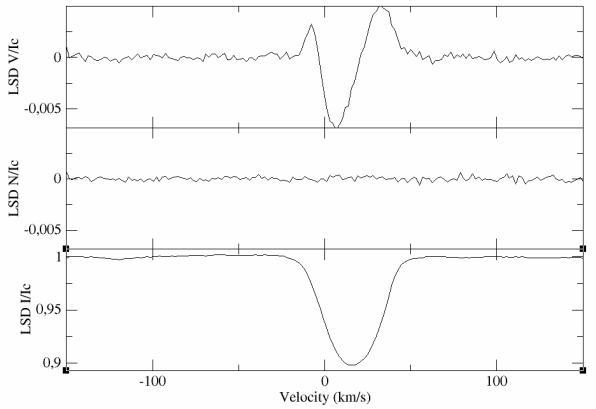

(a) BD+00 2099 – TIC 271310339

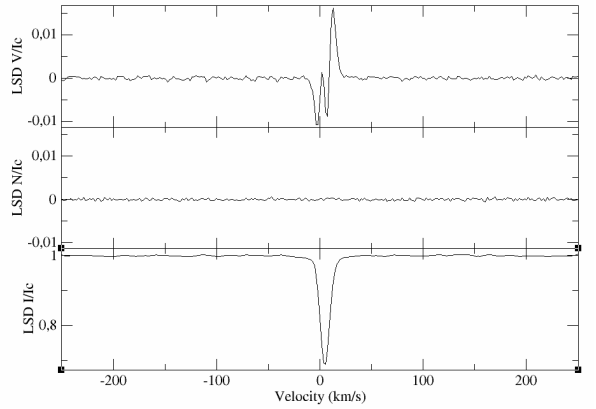

(b) BD+01 1920 – TIC 271375640

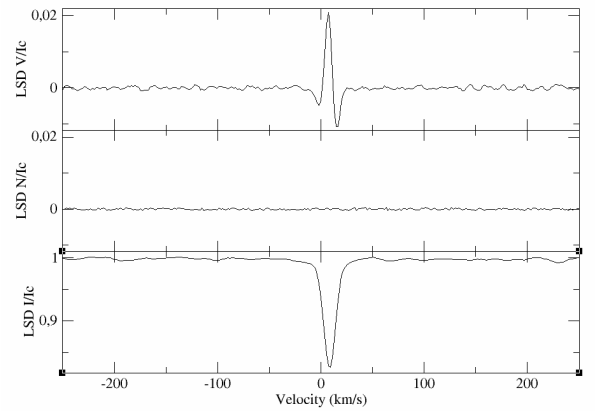

(c) BD+08 2211 – TIC 312111544

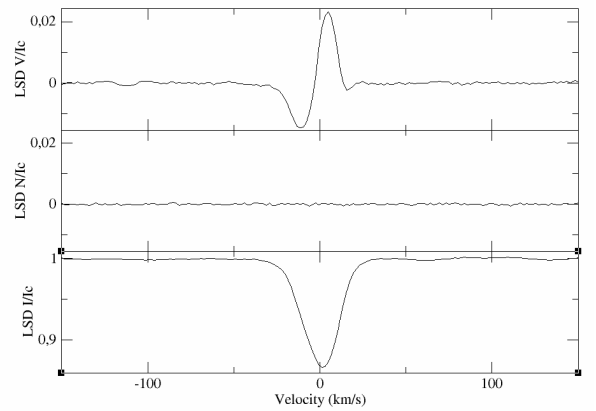

(d) BD+10 2572 – TIC 404536886

FIGURE B.1 – LSD Stokes V (upper panel), N (middle panel), and Stokes I (bottom panel) profiles for the various stars in our sample, arranged by stellar identifier.

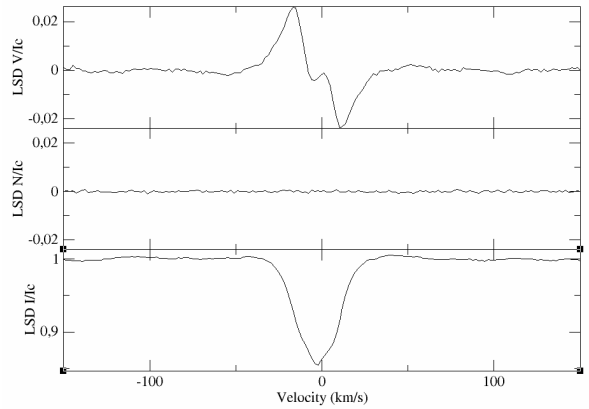

(a) BD+40 4697 – TIC 305482510

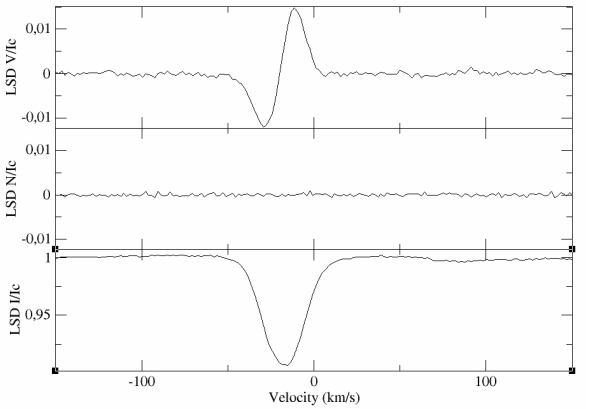

(b) BD+43 3648 – TIC 188301298

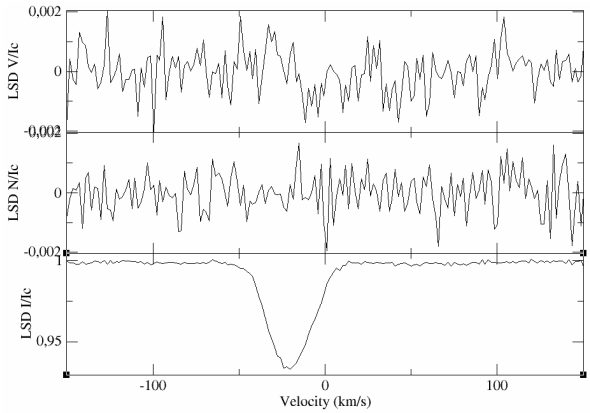

(c) BD+44 767 – TIC 65643991

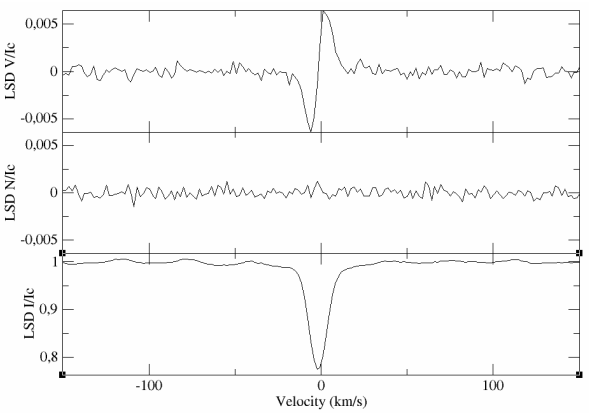

(d) BD+49 1011 – TIC 428515156

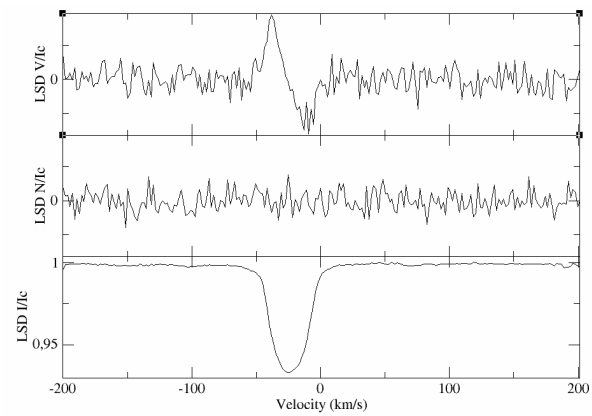

(e) HD 11140 – TIC 72150546

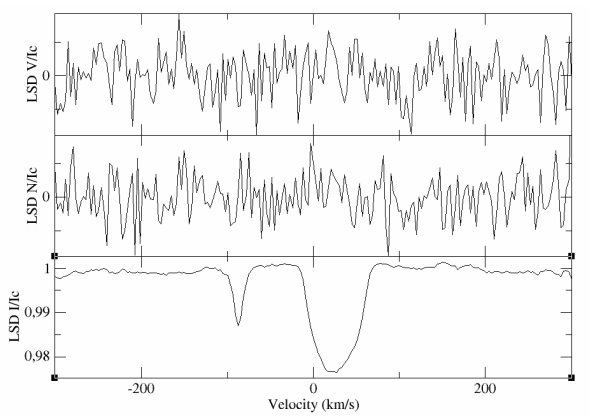

(f) HD 14251 – TIC 292977419

FIGURE B.2 – LSD Stokes V (upper panel), N (middle panel), and Stokes I (bottom panel) profiles for the various stars in our sample, arranged by stellar identifier (cont.).

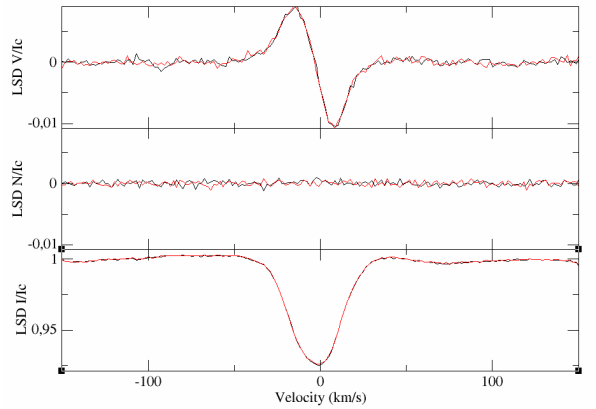

(a) HD 18410 – TIC 251412475

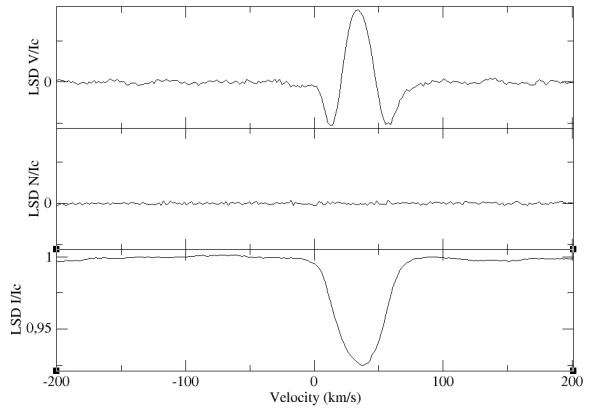

(b) HD 19846 – TIC 445923870

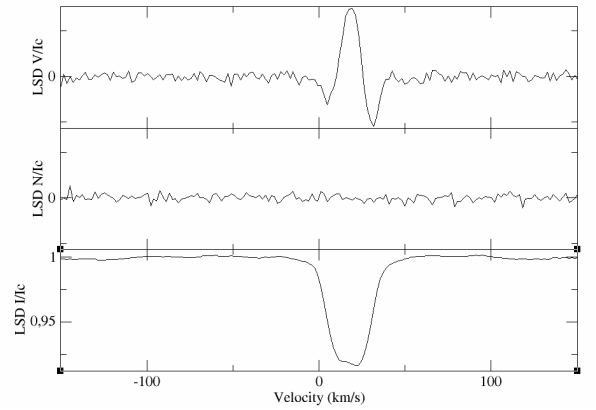

(c) HD 22961 – TIC 284084463

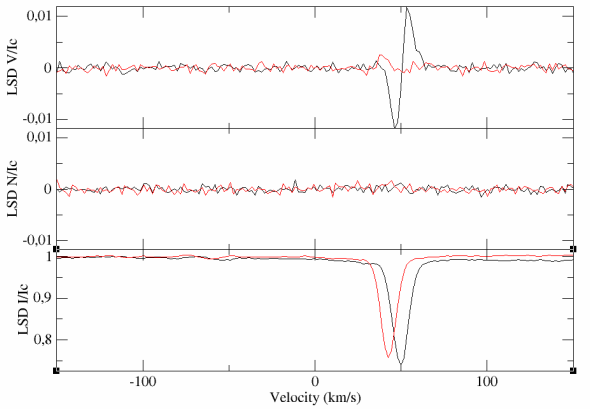

(d) HD 28238 – TIC 373024953

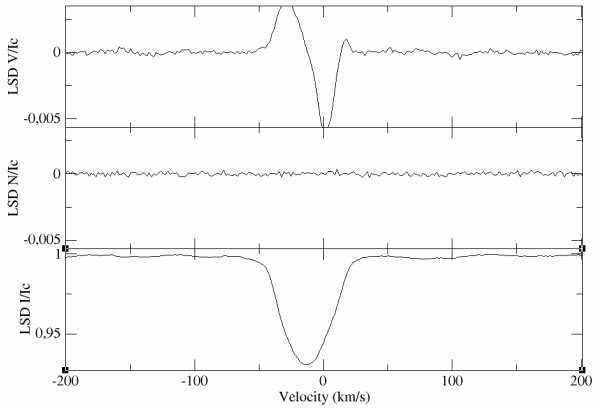

(e) HD 36259 – TIC 268068786

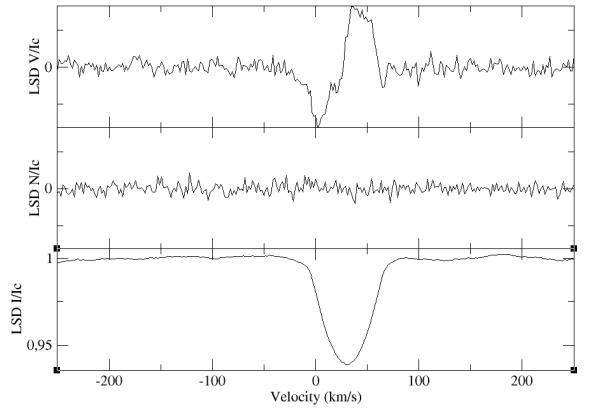

(f) HD 36955 – TIC 427377135

FIGURE B.3 – LSD Stokes V (upper panel), N (middle panel), and Stokes I (bottom panel) profiles for the various stars in our sample, arranged by stellar identifier (cont.).

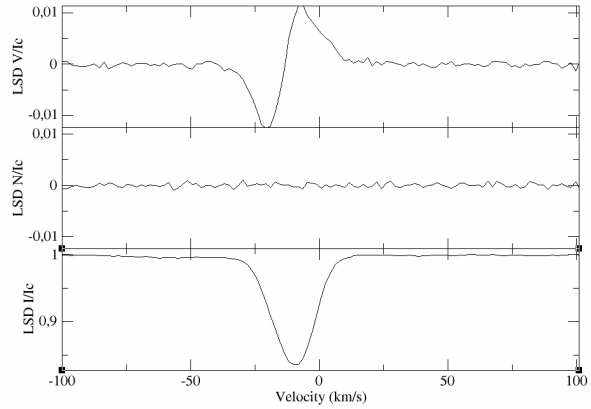

(a) HD 48560 – TIC 11767386

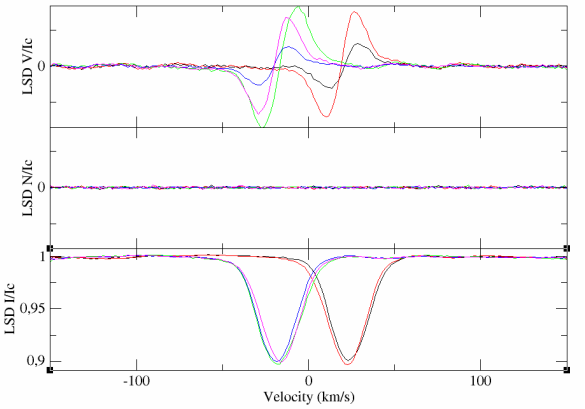

(b) HD 49198 – TIC 16485771

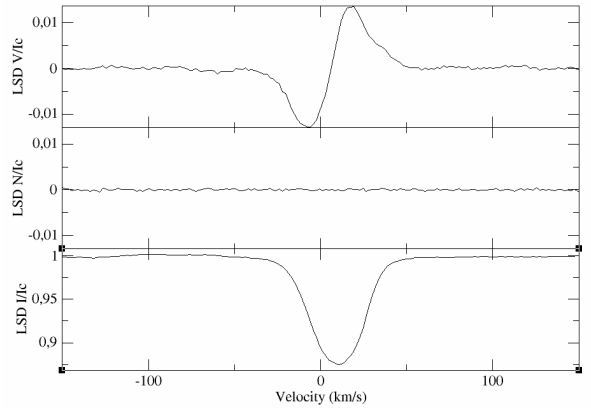

(c) HD 49522 – TIC 91136550

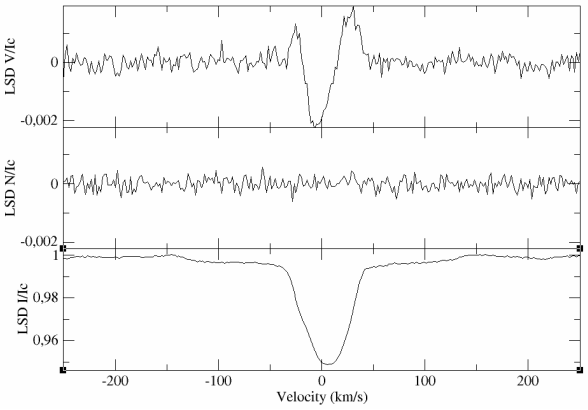

(d) HD 56514 – TIC 440829763

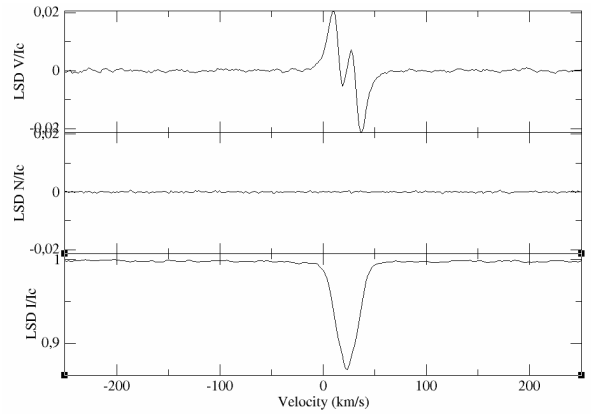

(e) HD 63843 – TIC 35884762

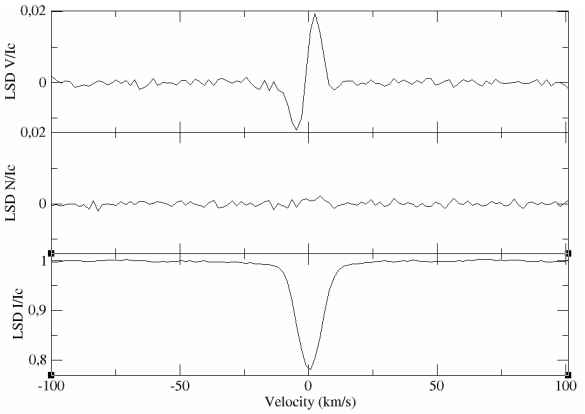

(f) HD 66533 – TIC 169971995

FIGURE B.4 – LSD Stokes V (upper panel), N (middle panel), and Stokes I (bottom panel) profiles for the various stars in our sample, arranged by stellar identifier (cont.).

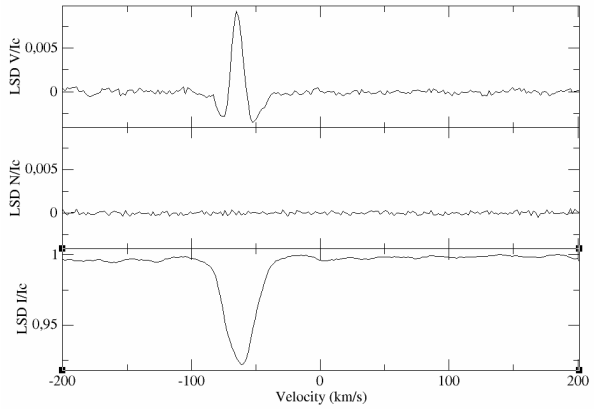

(a) HD 71047 – TIC 27256691

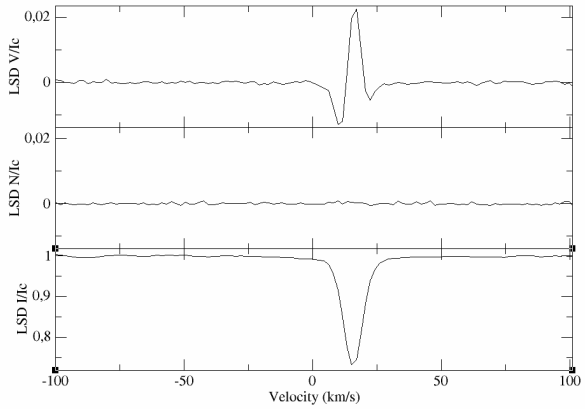

(b) HD 86170 – TIC 62815493

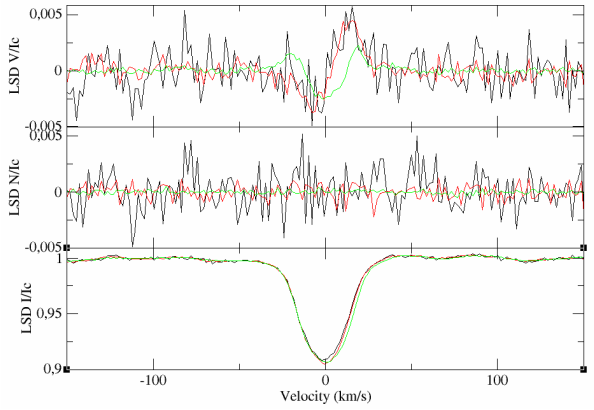

(c) HD 108662 – TIC 393808105

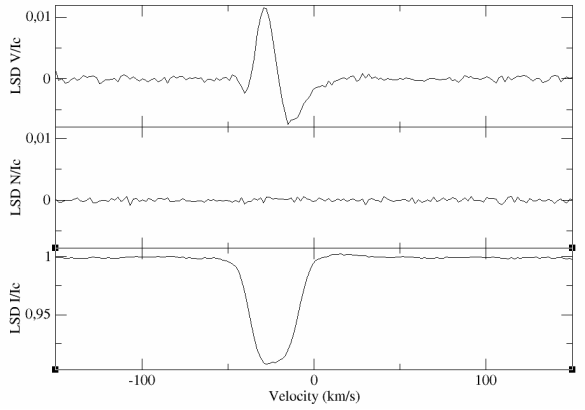

(d) HD 177128 – TIC 120495323

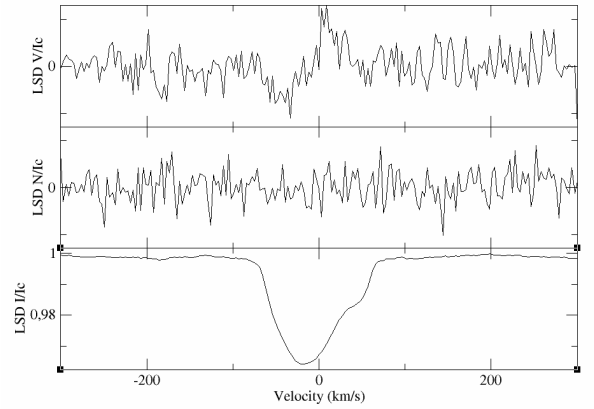

(e) HD 212714 – TIC 164282311

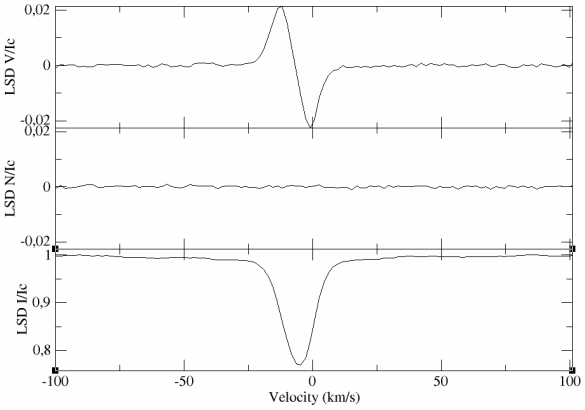

(f) HD 232285 – TIC 240808702

FIGURE B.5 – LSD Stokes V (upper panel), N (middle panel), and Stokes I (bottom panel) profiles for the various stars in our sample, arranged by stellar identifier (cont.).

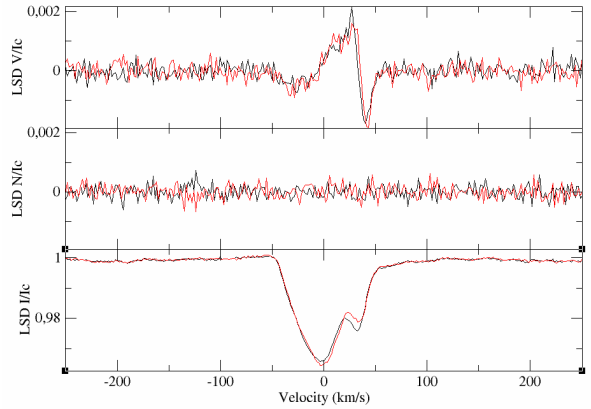

(a) HD 256582 – TIC 319616512

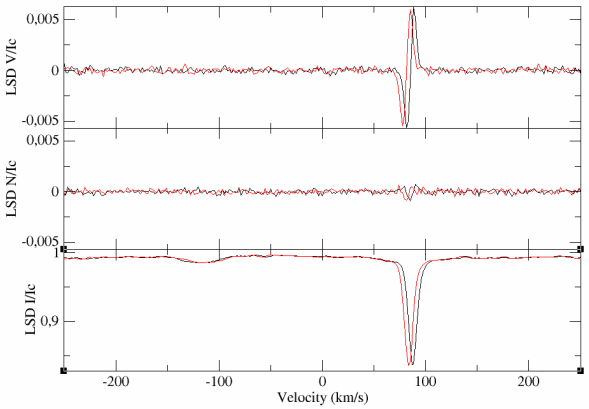

(b) HD 259273 – TIC 234878810

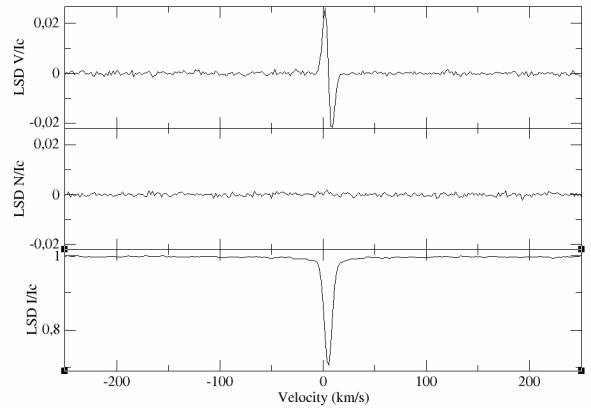

(c) HD 266267 – TIC 235391838

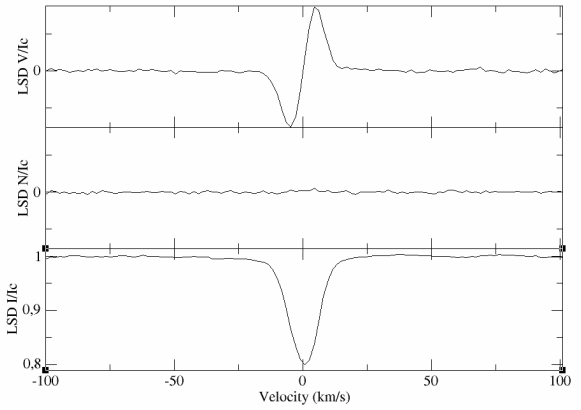

(d) HD 266311 – TIC 237662091

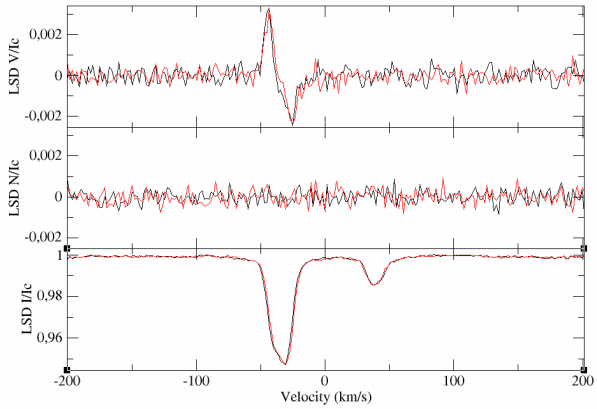

(e) HD 277595 – TIC 122563793

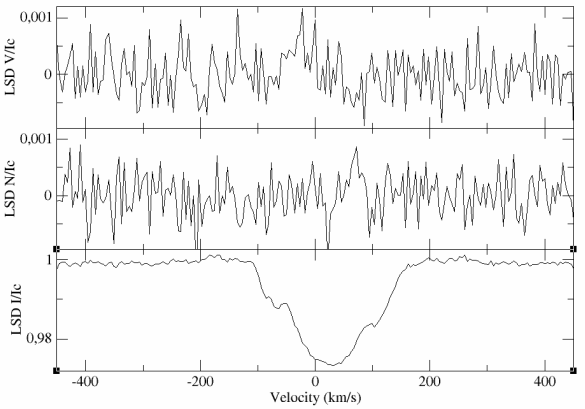

(f) HD 281193 – TIC 385555521

FIGURE B.6 – LSD Stokes V (upper panel), N (middle panel), and Stokes I (bottom panel) profiles for the various stars in our sample, arranged by stellar identifier (cont.).

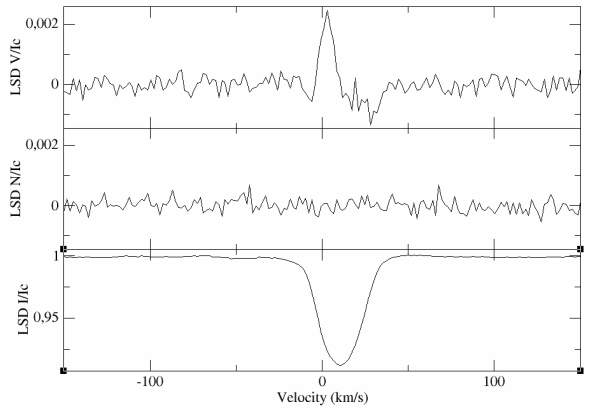

(a) TYC 2873-3205-1 – TIC 384988765

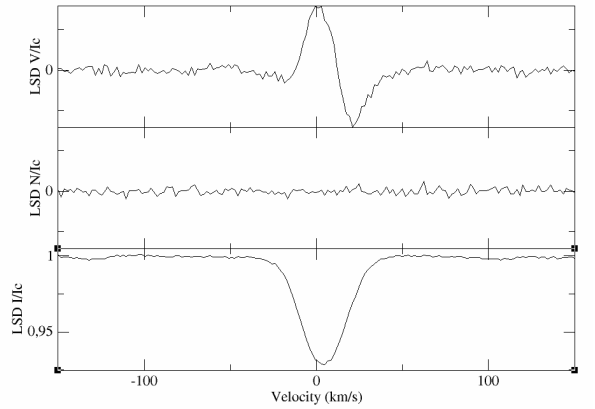

(b) TYC 3316-892-1 – TIC 458780077

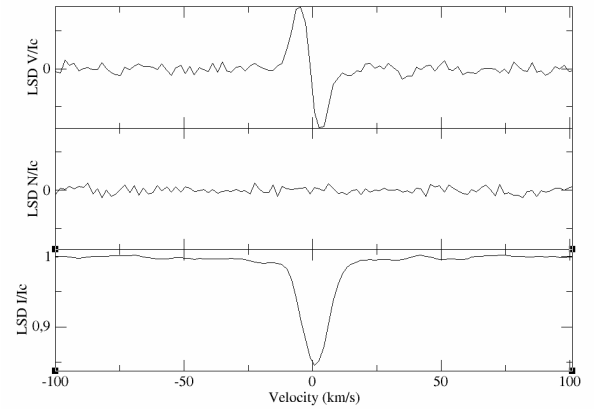

(c) TYC 3319-464-1 – TIC 117663254

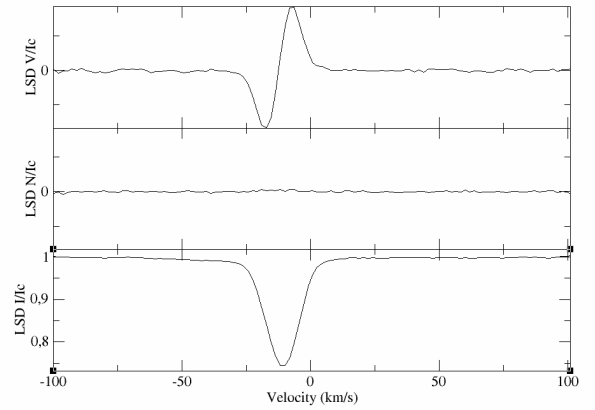

(d) TYC 3733-133-1 – TIC 252212077

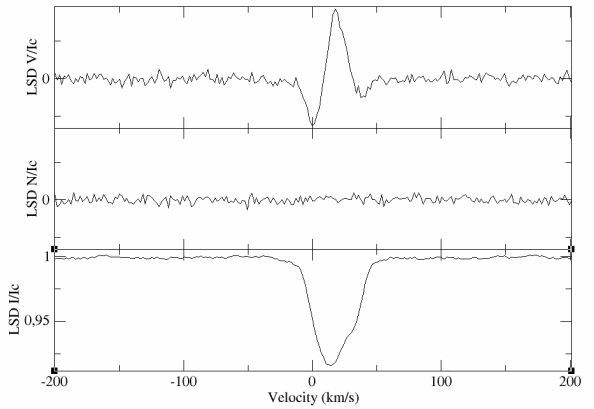

(e) TYC 3749-888-1 – TIC 321832920

FIGURE B.7 – LSD Stokes V (upper panel), N (middle panel), and Stokes I (bottom panel) profiles for the various stars in our sample, arranged by stellar identifier (cont.).

Publication List

Peer-reviewed Articles

K. Thomson-Paressant, C. Neiner, K. Zwintz, A. Escorza. "*The complex fossil magnetic field of the δ Scuti star HD 41641*". MNRAS.
DOI: 10.1093/mnras/staa3442

J. Labadie-Bartz, A.C. Carciofi, T. Henrique de Amorim, A. Rubio, A. Luiz Figueiredo, P. Ticiani dos Santos, **K. Thomson-Paressant**. "*Classifying Be Star Variability With TESS. I. The Southern Ecliptic*". ApJ.
DOI: 10.3847/1538-3881/ac5abd

K. Thomson-Paressant, C. Neiner, P. Lampens, J. Labadie-Bartz, R. Monier, P. Mathias, A. Tkachenko. "*A search for magnetic δ Scuti stars in Kepler hybrid candidates*". MNRAS.
DOI: 10.1093/mnras/stad2798

K. Thomson-Paressant, C. Neiner, J. Labadie-Bartz. "*Magnetism in LAMOST CP stars observed by TESS*". A&A.
DOI: 10.1051/0004-6361/202450651

Articles in preparation

K. Thomson-Paressant, C. Neiner, J. Labadie-Bartz. "*Discovery of new magnetic δ Scuti pulsators and current state-of-the-art in δ Scuti magnetism*". A&A.

C. Gutteridge, **K. Thomson-Paressant**, C. Neiner, C. Catala. "*A new NeoNarval data reduction pipeline with PyReduce*". A&A.

C. Neiner, **K. Thomson-Paressant**, C. Folsom, M. Deal, S. Kasprzack. "*Magnetic configuration of the δ Scuti star HD 188774*". A&A.

Contributions to conferences with proceedings

K. Thomson-Paressant & C. Neiner. "*Magnetic δ Scuti Stars*". MOBSTER-1 Virtual Conference, 2020.

K. Thomson-Paressant, C. Gutteridge, C. Neiner, C. Catala. "*A new NeoNarval pipeline with PyReduce*". SF2A, Strasbourg, 2023.

K. Thomson-Paressant, C. Neiner, J. Labadie-Bartz. "*State-of-the-art of magnetism in δ Scuti stars*". SF2A, Marseille, 2024.

K. Thomson-Paressant, C. Neiner, J. Labadie-Bartz. "*A first statistical picture of magnetism in δ Scuti stars*". BRITE Conference, Vienna, 2024.

Other contributions

K. Thomson-Paressant, C. Neiner, J. Labadie-Bartz. "*Probing magnetism in δ Scuti stars*". Elbereth Conference, Paris, 2023.

K. Thomson-Paressant, C. Neiner, J. Labadie-Bartz. "*Magneto-asteroseismology in δ Scuti stars*". LESIA Journée des Thèses, Paris, 2023.

K. Thomson-Paressant, C. Neiner, J. Labadie-Bartz. "*Magnetism in CP stars observed by TESS*". EAS, Krakow, 2023.

Bibliography

[1] G. Handler. *Asteroseismology. Planets, Stars and Stellar Systems. Volume 4 : Stellar Structure and Evolution, Eds. : T.D. Oswalt & M.A. Barstow*. T. 4. 2013, 207.

[2] O. Struve. *Some Unusual Short-period Variables*. Sky & Telesc. 14 (1955), 461.

[3] H. Lehmann et al. *Variability investigations of possible Maia stars*. A&A 300 (1995), 783.

[4] L. A. Balona. *Pulsation in hot main sequence stars : comparison of observations with models*. arXiv e-prints, arXiv :2310.09805 (2023).

[5] D. M. Bowman & D. W. Kurtz. *Characterizing the observational properties of δ Sct stars in the era of space photometry from the Kepler mission*. MNRAS 476.3 (2018), 3169-3184.

[6] T. Jayasinghe et al. *The ASAS-SN catalogue of variable stars VI : an all-sky sample of δ Scuti stars*. MNRAS 493.3 (2020), 4186-4208.

[7] F. Kahraman Aliçavuş et al. *On the Existence of "Maia variables"*. arXiv e-prints, arXiv :2404.16988 (2024), arXiv :2404.16988.

[8] G. A. Wade et al. *The MiMeS project : magnetism in massive stars. Cosmic Magnetic Fields : From Planets, to Stars and Galaxies. Eds. : K.G. Strassmeier et al.* T. 259. 2009, 333-338.

[9] L. Fossati et al. *B fields in OB stars (BOB) : on the detection of weak magnetic fields in the two early B-type stars β CMa and ϵ CMa. Possible lack of a "magnetic desert" in massive stars*. A&A 574, A20 (2015), A20.

[10] A. J. Martin et al. *First results from the LIFE project : discovery of two magnetic hot evolved stars*. MNRAS 475.2 (2017), 1521-1536.

[11] M. E. Shultz et al. *The magnetic early B-type stars - III. A main-sequence magnetic, rotational, and magnetospheric biography*. MNRAS 490.1 (2019), 274-295.

[12] S. Bagnulo et al. *Searching for links between magnetic fields and stellar evolution. I. A survey of magnetic fields in open cluster A- and B-type stars with FORS1*. A&A 450.2 (2006), 777-791.

[13] J. D. Landstreet et al. *Searching for links between magnetic fields and stellar evolution : II. The evolution of magnetic fields as revealed by observations of Ap stars in open clusters and associations*. A&A 470.2 (2007), 685-698.

[14] J. D. Landstreet et al. *Searching for links between magnetic fields and stellar evolution. III. Measurement of magnetic fields in open cluster Ap stars with ESPaDOnS*. A&A 481.2 (2008), 465-480.

[15] E. F. Borra, J. D. Landstreet & L. Mestel. *Magnetic stars*. ARA&A 20 (1982), 191-220.

[16] A. ud-Doula & S. P. Owocki. *Dynamical Simulations of Magnetically Channeled Line-driven Stellar Winds. I. Isothermal, Nonrotating, Radially Driven Flow*. ApJ 576.1 (2002), 413-428.

[17] A. Ud-Doula, S. P. Owocki & R. H. D. Townsend. *Dynamical simulations of magnetically channelled line-driven stellar winds - III. Angular momentum loss and rotational spin-down*. MNRAS 392.3 (2009), 1022-1033.

[18] V. Petit et al. *Magnetic massive stars as progenitors of 'heavy' stellar-mass black holes*. MNRAS 466.1 (2017), 1052-1060.

[19] F. Lignières et al. *The dichotomy between strong and ultra-weak magnetic fields among intermediate-mass stars. Eds. : P. Pascal et al. Magnetic Fields throughout Stellar Evolution*. T. 302. 2014, 338-347.

[20] L. Jouve, T. Gastine & F. Lignières. *Three-dimensional evolution of magnetic fields in a differentially rotating stellar radiative zone*. A&A 575, A106 (2015), A106.

[21] P. Petit et al. *Detection of a weak surface magnetic field on Sirius A : are all tepid stars magnetic ?* A&A 532, L13 (2011), L13.

[22] A. Blazère et al. *Detection of ultra-weak magnetic fields in Am stars : β Ursae Majoris and θ Orionis.* A&A 586 (2016), A97.

[23] A. Blazère et al. *Magnetic geometry and surface differential rotation of the bright Am star Alhena A.* MNRAS 492.4 (2020), 5794-5810.

[24] K. C. Augustson, A. S. Brun & J. Toomre. *The Magnetic Furnace : Intense Core Dynamos in B Stars.* ApJ 829.2, 92 (2016), 92.

[25] N. A. Featherstone et al. *Effects of Fossil Magnetic Fields on Convective Core Dynamos in A-type Stars.* ApJ 705.1 (2009), 1000-1018.

[26] J. Fuller, A. L. Piro & A. S. Jermyn. *Slowing the spins of stellar cores.* MNRAS 485.3 (2019), 3661-3680.

[27] K. Takahashi & N. Langer. *Modeling of magneto-rotational stellar evolution. I. Method and first applications.* A&A 646, A19 (2021), A19.

[28] A. S. Brun, M. K. Browning & J. Toomre. *Simulations of Core Convection in Rotating A-Type Stars : Magnetic Dynamo Action.* ApJ 629.1 (2005), 461-481.

[29] Z. Keszthelyi et al. *The effects of surface fossil magnetic fields on massive star evolution : I. Magnetic field evolution, mass-loss quenching, and magnetic braking.* MNRAS 485.4 (2019), 5843-5860.

[30] Z. Keszthelyi et al. *The effects of surface fossil magnetic fields on massive star evolution - II. Implementation of magnetic braking in MESA and implications for the evolution of surface rotation in OB stars.* MNRAS 493.1 (2020), 518-535.

[31] M. Oksala et al. *Discovery of a strong magnetic field in the rapidly rotating B2Vn star HR 7355.* MNRAS 405.1 (2010), L51-L55.

[32] J. Grunhut et al. *HR 5907 : Discovery of the most rapidly rotating magnetic early B-type star by the MiMeS Collaboration.* MNRAS 419.2 (2012), 1610-1627.

[33] A. Maeder & G. Meynet. *Stellar evolution with rotation and magnetic fields. III. The interplay of circulation and dynamo.* A&A 440.3 (2005), 1041-1049.

[34] A. A. Pamyatnykh. *Pulsation Instability Domain of δ Scuti Variables. Eds. : Breger M. & Montgomery M., ASPCS Vol. 210, Delta Scuti and Related Stars.* T. Vol. 210. 2000, 215.

[35] V. Antoci et al. *The Role of Turbulent Pressure as a Coherent Pulsational Driving Mechanism : The Case of the δ Scuti Star HD 187547.* ApJ 796.2, 118 (2014).

[36] D. R. Xiong et al. *Turbulent convection and pulsation stability of stars - II. Theoretical instability strip for δ Scuti and γ Doradus stars.* MNRAS 457.3 (2016).

[37] C. Aerts, J. Christensen-Dalsgaard & D. W. Kurtz. *Asteroseismology.* Astronomy et Astrophysics Library, Springer, Berlin, 2010.

[38] M. Breger. *The multiperiodic δ Scuti star 4 Canum Venaticorum : amplitude variability.* MNRAS 313.1 (2000), 129-135.

[39] D. M. Bowman et al. *Amplitude modulation in δ Sct stars : statistics from an ensemble study of Kepler targets.* MNRAS 460.2 (2016), 1970-1989.

[40] V. Khalack et al. *Rotational and pulsational variability in the TESS light curve of HD 27463.* MNRAS 490.2 (2019), 2102-2111.

[41] C. Neiner & P. Lampens. *First discovery of a magnetic field in a main-sequence δ Scuti star : The Kepler star HD 188774.* MNRAS 454 (2015).

[42] C. Neiner, G. Wade & J. Sikora. *Discovery of a magnetic field in the δ Scuti F2m star ρ Pup.* MNRAS 468 (2017).

[43] K. Zwintz et al. *The Magnetic δ Scuti Star β Cas. Physics of Magnetic Stars. ASP Conference Series, Vol. 518, Proceedings of a conference held 1-5 October, 2018 at Special Astrophysical Observatory, Nizhny Arkhyz, Russia. Eds. : D.O. Kudryavtsev et al. San Francisco : Astronomical Society of the Pacific.* T. 518. Astronomical Society of the Pacific Conference Series. 2019, 59.

[44] K. Zwintz et al. *β Cas : The first δ Scuti star with a dynamo magnetic field.* A&A 643 (2020), A110.

[45] D. W. Kurtz et al. *δSct pulsation in magnetic Ap stars : the discovery of δSct pulsations in HD218994AB and measurement of the magnetic fields of HD218994A and HD21190.* MNRAS 386.3 (2008).

[46] S. Hubrig & M. Scholler. *Confirmation of the magnetic nature of the delta Scuti star HD 21190.* Information Bulletin on Variable Stars 6174 (2016), 1.

[47] E. Alecian et al. *A high-resolution spectropolarimetric survey of Herbig Ae/Be stars – I. Observations and measurements.* MNRAS 429.2 (2013), 1001-1026.

[48] J. D. Landstreet & G. Mathys. *Magnetic models of slowly rotating magnetic Ap stars : aligned magnetic and rotation axes.* A&A 359 (2000), 213-226.

[49] J.-F. Donati et al. *ESPaDOnS : The New Generation Stellar Spectro-Polarimeter. Performances and First Results. Solar Polarization 4, ASP Conference Series, Vol. 358, Proceedings of the conference held 19-23 September, 2005, in Boulder, Colorado, USA. Eds. : R. Casini & B. W. Lites, p.362.* T. 358. Astronomical Society of the Pacific Conference Series. 2006, 362.

[50] M. Aurière. *Stellar Polarimetry with NARVAL.* EAS Publications Series 9 (2003).

[51] T. Böhm, R. Cabanac & A. Lopez Ariste. *Neo-Narval Technical Specifications.* Rapp. tech. Obs. Midi-Pyrénées, 2016.

[52] A. López Ariste et al. *Three-dimensional imaging of convective cells in the photosphere of Betelgeuse.* A&A 661 (2022), A91.

[53] N. Piskunov et al. *HARPSpol — The New Polarimetric Mode for HARPS.* The Messenger 143 (2011), 7-10.

[54] K. Thomson-Paressant et al. *A new NeoNarval pipeline with PyReduce. SF2A-2023 : Proceedings of the Annual meeting of the French Society of Astronomy and Astrophysics. Eds. : M. N'Diaye et al.* 2023, 507-510.

[55] I. Sahoo, J. Guinness & B. J. Reich. *A Test for Isotropy on a Sphere using Spherical Harmonic Functions.* arXiv e-prints, arXiv :1711.04092 (2017).

[56] M. Briquet et al. *Multisite spectroscopic seismic study of the β Cep star V2052 Ophiuchi : inhibition of mixing by its magnetic field.* MNRAS 427.1 (2012), 483-493.

[57] B. Buysschaert et al. *Forward seismic modeling of the pulsating magnetic B-type star HD 43317.* A&A 616, A148 (2018), A148.

[58] D. Lecoanet, D. M. Bowman & T. Van Reeth. *Asteroseismic inference of the near-core magnetic field strength in the main-sequence B star HD 43317.* MNRAS 512.1 (2022), L16-L20.

[59] B. Buysschaert et al. *Detection of magnetic fields in chemically peculiar stars observed with the K2 space mission.* MNRAS 478.2 (2018), 2777-2793.

[60] V. Prat et al. *Period spacings of gravity modes in rapidly rotating magnetic stars. I. Axisymmetric fossil field with poloidal and toroidal components.* A&A 627, A64 (2019).

[61] V. Prat et al. *Period spacings of gravity modes in rapidly rotating magnetic stars II. The case of an oblique dipolar fossil magnetic field.* A&A 636, A100 (2020).

[62] M. Briquet et al. *An asteroseismic study of the β Cephei star θ Ophiuchi : constraints on global stellar parameters and core overshooting.* MNRAS 381.4 (2007), 1482-1488.

[63] M. G. Pedersen et al. *Internal mixing of rotating stars inferred from dipole gravity modes.* Nature Astronomy 5 (2021), 715-722.

[64] C. Neiner et al. *Detecting and modelling the magnetic field of the β Cephei star V 2052 Ophiuchi.* A&A 537, A148 (2012), A148.

[65] J.-P. Zahn. *Rapid rotation and mixing in active OB stars - Physical processes. Active OB Stars : Structure, Evolution, Mass Loss, and Critical Limits. Eds. : C. Neiner et al.* T. 272. 2011, 14-25.

[66] J.-F. Donati et al. *Spectropolarimetric observations of active stars.* MNRAS 291.4 (1997), 658-682.

[67] N. E. Piskunov et al. *VALD : The Vienna Atomic Line Data Base.* A&AS 112 (1995).

[68] F. Kupka et al. *VALD-2 : Progress of the Vienna Atomic Line Data Base.* A&AS 138 (1999).

[69] T. Ryabchikova et al. *A major upgrade of the VALD database.* Phys. Scr. 90.5, 054005 (2015), 054005.

[70] J. H. Grunhut et al. *The MiMeS survey of Magnetism in Massive Stars : magnetic analysis of the O-type stars.* MNRAS 465.2 (2017), 2432-2470.

[71] D. E. Rees & M. D. Semel. *Line formation in an unresolved magnetic element : a test of the centre of gravity method.* A&A 74.1 (1979), 1-5.

[72] G. A. Wade et al. *High-precision magnetic field measurements of Ap and Bp stars*. MNRAS 313.4 (2000), 851-867.

[73] J.-F. Donati et al. *Photospheric imaging of the RS CVn system HR 1099*. A&A 265 (1992), 682-700.

[74] F. Royer et al. *Rotational velocities of A-type stars. I. Measurement of v sin i in the southern hemisphere*. A&A 381 (2002), 105-121.

[75] R. Glebocki & P. Gnaciński. *Systematic errors in the determination of stellar rotational velocities. 13th Cambridge Workshop on Cool Stars, Stellar Systems and the Sun. Eds. : F. Favata et al.* T. 560. ESA Special Publication. 2005, 571.

[76] Gaia Collaboration et al. *Gaia Data Release 3. Summary of the content and survey properties*. A&A 674, A1 (2023), A1.

[77] D. W. N. Stibbs. *A Study of the Spectrum and Magnetic Variable Star HD 125248*. MNRAS 110.4 (1950), 395-404.

[78] G. W. Preston. *A Statistical Investigation of the Orientation of Magnetic Axes in the Periodic Magnetic Variables*. ApJ 150 (1967), 547.

[79] M. Schwarzschild. *Zeeman Shifts for Stellar Dipoles and Quadrupoles with Inclined Axes*. ApJ 112 (1950), 222-223.

[80] A. Claret. *VizieR Online Data Catalog : Limb-darkening for Space Mission GAIA (Claret, 2019)*. VizieR Online Data Catalog, VI/154 (2019), VI/154.

[81] C. Neiner et al. *Search for magnetic fields in particle-accelerating colliding-wind binaries*. A&A 575 (2015), A66.

[82] C. P. Folsom et al. *The evolution of surface magnetic fields in young solar-type stars - I. The first 250 Myr*. MNRAS 457.1 (2016), 580-607.

[83] C. P. Folsom et al. *The evolution of surface magnetic fields in young solar-type stars II : the early main sequence (250–650 Myr)*. MNRAS 474.4 (2017), 4956-4987.

[84] J. Skilling & R. K. Bryan. *Maximum Entropy Image Reconstruction - General Algorithm*. MNRAS 211 (1984), 111.

[85] O. Kochukhov & G. A. Wade. *Magnetic field topology of τ Scorpii. The uniqueness problem of Stokes V ZDI inversions*. A&A 586, A30 (2016), A30.

[86] K. Thomson-Paressant et al. *A search for magnetic δ Scuti stars in Kepler hybrid candidates*. MNRAS 526.2 (2023), 1728-1741.

[87] M. Auvergne et al. *The CoRoT satellite in flight : description and performance*. A&A 506 (1 2009), 411-424.

[88] W. J. Borucki et al. *Kepler Planet-Detection Mission : Introduction and First Results*. Science 327.5968 (2010), 977.

[89] G. R. Ricker et al. *Transiting Exoplanet Survey Satellite (TESS)*. J. Astron. Telesc. Instrum. Syst. 1, 014003 (2015), 014003.

[90] G. Henry & F. Fekel. *HD 8801 : A Unique Single Am Star with γ Doradus and δ Scuti Pulsations*. AJ 129 (2005), 2026-2033.

[91] A. Grigahcéne et al. *Kepler observations : Light shed on the hybrid γ Doradus – δ Scuti pulsation phenomenon*. Astronomische Nachrichten 331.9-10 (2010), 989-992.

[92] K. Uytterhoeven et al. *The Kepler characterization of the variability among A- and F-type stars. I. General overview*. A&A 534, A125 (2011), A125.

[93] L. A. Balona et al. *Analysis of Kepler B stars : rotational modulation and Maia variables*. MNRAS 451.2 (2015), 1445-1459.

[94] P. Lampens et al. *Low-frequency variations of unknown origin in the Kepler δ Scuti star KIC5988140 =HD188774*. A&A 549 (2013), A104.

[95] K. Thomson-Paressant et al. *The complex fossil magnetic field of the δ Scuti star HD 41641*. MNRAS 500 (2020), 1992-1999.

[96] A. David-Uraz et al. *Magnetic OB[A] Stars with TESS : probing their Evolutionary and Rotational properties (MOBSTER) - I. First-light observations of known magnetic B and A stars*. MNRAS 487.1 (2019), 304-317.

[97] K. C. Augustson, A. S. Brun & J. Toomre. *Dynamo Action and Magnetic Cycles in F-type Stars*. ApJ 777.2, 153 (2013), 153.

[98] A. R. G. Santos et al. *Surface Rotation and Photometric Activity for Kepler Targets. II. G and F Main-sequence Stars and Cool Subgiant Stars*. ApJS 255.1, 17 (2021), 17.

[99] P. Lampens et al. *Do we see the simultaneous occurrence of stellar rotational effects and short-period pulsations in some A-type Kepler stars ?* Astron. Nachr. 333.10 (2012), 975-977.

[100] S. Hubrig & M. Scholler. *Confirmation of the magnetic nature of the delta Scuti star HD 21190*. Information Bulletin on Variable Stars 6174 (2016), 1.

[101] N. Barac et al. *Revisiting bright δ Scuti stars and their period-luminosity relation with TESS and Gaia DR3*. MNRAS 516.2 (2022), 2080-2094.

[102] S. Bagnulo et al. *Magnetic field measurements and their uncertainties : the FORS1 legacy*. A&A 538 (2012), A129.

[103] S. J. Murphy et al. *On the first δ Sct-roAp hybrid pulsator and the stability of p and g modes in chemically peculiar A/F stars*. MNRAS 498.3 (2020), 4272-4286.

[104] S. Hubrig et al. *Searching for magnetic fields in pulsating A-type stars : the discovery of a strong field in the probable δ Sct star HD 340577 and a null result for the γ Dor star HR 8799*. MNRAS (2023).

[105] K. Zwintz et al. *Revisiting the pulsational characteristics of the exoplanet host star β Pictoris*. A&A 627 (2019), A28.

[106] G. Raskin et al. *HERMES : a high-resolution fibre-fed spectrograph for the Mercator telescope*. A&A 526 (2011), A69.

[107] P. Lampens et al. *Multi-technique investigation of the binary fraction of A-F type candidate hybrid variable stars discovered by Kepler*. A&A 610 (2018), A17.

[108] M.-A. Dupret et al. *Convection-pulsation coupling. II. Excitation and stabilization mechanisms in δ Sct and γ Dor stars*. A&A 435.3 (2005), 927-939.

[109] P. Lampens et al. *Orbital solutions derived from radial velocities and time delays for four Kepler systems with A/F-type (candidate) hybrid pulsators*. A&A 647 (2021), A139.

[110] P. Lenz & M. Breger. *Period04 User Guide*. Communications in Asteroseismology 146 (2005), 53-136.

[111] L. A. Balona, J. Daszyńska-Daszkiewicz & A. A. Pamyatnykh. *Pulsation frequency distribution in δ Scuti stars*. MNRAS 452.3 (2015), 3073-3084.

[112] L. A. Balona et al. *The Kepler view of γ Doradus stars*. MNRAS 415.4 (2011), 3531-3538.

[113] V. Antoci et al. *The first view of δ Scuti and γ Doradus stars with the TESS mission*. MNRAS 490.3 (2019), 4040-4059.

[114] L. A. Balona & W. A. Dziembowski. *Kepler observations of δ Scuti stars*. MNRAS 417.1 (2011), 591-601.

[115] S. J. Murphy. *An examination of some characteristics of Kepler short- and long-cadence data*. MNRAS 422.1 (2012), 665-671.

[116] H. Saio et al. *An astrophysical interpretation of the remarkable g-mode frequency groups of the rapidly rotating γ Dor star, KIC 5608334*. MNRAS 477.2 (2018), 2183-2195.

[117] M. Breger et al. *Relationship between Low and High Frequencies in δ Scuti Stars : Photometric Kepler and Spectroscopic Analyses of the Rapid Rotator KIC 8054146*. ApJ 759.1, 62 (2012), 62.

[118] A. Samadi-Ghadim, P. Lampens & L. Gizon. *KIC 6951642 : A confirmed Kepler γ Doradus – δ Scuti star with intermediate to fast rotation in a possible single-lined binary system*. A&A 667 (2022), A60.

[119] A. Escorza et al. *HD 41641 : A classical δ Sct-type pulsator with chemical signatures of an Ap star*. A&A 588, A71 (2016), A71.

[120] M. Ammler-von Eiff & A. Reiners. *New measurements of rotation and differential rotation in A-F stars : are there two populations of differentially rotating stars ?* A&A 542, A116 (2012).

[121] I. Hubeny & T. Lanz. *Accelerated complete-linearization method for calculating NLTE model stellar atmospheres*. A&A 262.2 (1992), 501-514.

[122] R. L. Kurucz. *Atomic and Molecular Data for Opacity Calculations*. Rev. Mex. Astron. Astrofis. 23 (1992), 45.

[123] R. L. Kurucz. *ATLAS12, SYNTHE, ATLAS9, WIDTH9, et cetera*. Mem. Soc. Astron. Ital. Supplementi 8 (2005), 14.

[124] R. L. Kurucz. *ATLAS12 : Opacity sampling model atmosphere program.* Astrophysics Source Code Library, record ascl :1303.024. 2013.

[125] A. Tkachenko et al. *Spectrum analysis of bright Kepler γ Doradus candidate starsc.* MNRAS 422.4 (2012), 2960-2968.

[126] A. Tkachenko et al. *Spectrum analysis of bright Kepler late B- to early F-stars.* MNRAS 431.4 (2013), 3685-3696.

[127] G. Catanzaro et al. *Atmospheric parameters and pulsational properties for a sample of δ Sct, γ Dor and hybrid Kepler targets.* MNRAS 411.2 (2011), 1167-1176.

[128] G. Catanzaro & V. Ripepi. *Fundamental parameters of eight Am stars : comparing observations with theory.* MNRAS 441.2 (2014), 1669-1680.

[129] J. H. Grunhut & C. Neiner. *Magnetic fields in early-type stars.* Proc. Int. Astron. Union 305 (2015), 53-60.

[130] G. A. Wade et al. *The magnetic characteristics of Galactic OB stars from the MiMeS survey of magnetism in massive stars.* Proc. Int. Astron. Union 9.S302 (2013), 265-269.

[131] L. Fossati et al. *Evidence of magnetic field decay in massive main-sequence stars.* A&A 592, A84 (2016), A84.

[132] A. A. Vidotto et al. *Stellar magnetism : empirical trends with age and rotation.* MNRAS 441.3 (2014), 2361-2374.

[133] S. Ekström et al. *Grids of stellar models with rotation. I. Models from 0.8 to 120 $M_\odot$ at solar metallicity ($Z = 0.014$).* A&A 537, A146 (2012), A146.

[134] D. W. Latham et al. *The Kepler Input Catalog. American Astronomical Society Meeting Abstracts.* T. 207. American Astronomical Society Meeting Abstracts. 2005, 110.13, 110.13.

[135] C. Bertaud. *Catalogue et bibliographie des étoiles A à spectre particulier Premier supplément.* Journal des Observateurs 43 (1960), 129.

[136] M. G. Pedersen et al. *Do A-type stars flare ?* MNRAS 466.3 (2017), 3060-3076.

[137] L. A. Balona et al. *Spots on Am stars.* MNRAS 448.2 (2015), 1378-1388.

[138] T. Van Reeth, Tkachenko, A. & Aerts, C. *Interior rotation of a sample of adus stars from ensemble modelling of their gravity-mode period spacings.* A&A 593 (2016), A120.

[139] M. Takata et al. *A diagnostic diagram for gamma Doradus variables and slowly pulsating B-type stars.* A&A 635 (2020).

[140] H. Saio et al. *Rotation of the convective core in γ Dor stars measured by dips in period spacings of g modes coupled with inertial modes.* MNRAS 502.4 (2021), 5856-5874.

[141] C. Neiner et al. *MOBSTER : Magneto-asteroseismology of hot stars with TESS. SF2A-2021 : Proceedings of the Annual meeting of the French Society of Astronomy and Astrophysics. Eds. : A. Siebert et al.* 2021, 161-164.

[142] J. Silvester et al. *On the incidence of magnetic fields in slowly pulsating B, β Cephei and B-type emission-line stars.* MNRAS 398.3 (2009), 1505-1511.

[143] K. Thomson-Paressant, C. Neiner & J. Labadie-Bartz. *Magnetism in LAMOST CP stars observed by TESS.* A&A 689, A208 (2024), A208.

[144] G. W. Preston. *The chemically peculiar stars of the upper main sequence.* ARA&A 12 (1974), 257-277.

[145] G. Michaud. *Diffusion Processes in Peculiar a Stars.* ApJ 160 (1970), 641.

[146] G. Alecian. *Diffusion Processes and Chemical Peculiarities in Magnetic Stars. Upper Main Sequence Stars with Anomalous Abundances, Eds. : C.R. Cowley et al.,* Dordrecht : Springer Netherlands, 1986, 381-393.

[147] S. C. Wolff. *The Incidence of Ap Stars.* PASP 80.474 (1968), 281.

[148] M. Aurière et al. *Weak magnetic fields in Ap/Bp stars - Evidence for a dipole field lower limit and a tentative interpretation of the magnetic dichotomy.* A&A 475.3 (2007), 1053-1065.

[149] O. Kochukhov. *Asteroseismology of chemically peculiar stars.* CoAst 159 (2009), 61-70.

[150] J. Sikora et al. *A volume-limited survey of mCP stars within 100 pc II : rotational and magnetic properties.* MNRAS 483.3 (2019), 3127-3145.

[151] J.-F. Donati & J. Landstreet. *Magnetic Fields of Nondegenerate Stars*. Annu. Rev. Astron. 47.1 (2009), 333-370.

[152] L. Ferrario, A. Melatos & J. Zrake. *Magnetic Field Generation in Stars*. Space Sci. Rev. 191.1-4 (2015), 77-109.

[153] L. Fossati et al. *B fields in OB stars (BOB) : Low-resolution FORS2 spectropolarimetry of the first sample of 50 massive stars*. A&A 582 (2015), A45.

[154] H. W. Babcock. *The 34-KILOGAUSS Magnetic Field of HD 215441*. ApJ 132 (1960), 521.

[155] J. D. Landstreet. *A search for magnetic fields in normal upper-main-sequence stars*. ApJ 258 (1982), 639-650.

[156] S. Hümmerich et al. *The Kepler view of magnetic chemically peculiar stars*. A&A 619 (2018), A98.

[157] D. W. Kurtz. *Asteroseismology Across the Hertzsprung–Russell Diagram*. ARA&A 60.1 (2022), 31-71.

[158] G. Zhao et al. *LAMOST spectral survey — An overview*. RAA 12.7 (2012), 723-734.

[159] X.-Q. Cui et al. *The Large Sky Area Multi-Object Fiber Spectroscopic Telescope (LAMOST)*. RAA 12.9 (2012), 1197-1242.

[160] S. Hümmerich, E. Paunzen & K. Bernhard. *A plethora of new, magnetic chemically peculiar stars from LAMOST DR4*. A&A 640 (2020), A40.

[161] H. M. Maitzen. *Photoelectric filter photometry of the lambda 5200 Å flux depression in Ap-stars*. A&A 51 (1976), 223-233.

[162] F. Kupka, E. Paunzen & H. M. Maitzen. *The 5200-Å flux depression of chemically peculiar stars - I. Synthetic Δa photometry : the normality line*. MNRAS 341.3 (2003), 849-854.

[163] F. Kupka et al. *The 5200-Åflux depression of chemically peculiar stars - II. The cool chemically peculiar and λ Bootis stars*. MNRAS 352.3 (2004), 863-876.

[164] S. A. Khan & D. V. Shulyak. *Theoretical analysis of the atmospheres of CP stars. Effects of the individual abundance patterns*. A&A 469.3 (2007), 1083-1100.

[165] C. Stigler et al. *Spectrophotometric analysis of the 5200 Å region for peculiar and normal stars*. A&A 562, A65 (2014), A65.

[166] J. Labadie-Bartz et al. *Photometric variability of the LAMOST sample of magnetic chemically peculiar stars as seen by TESS*. A&A 676 (2023), A55.

[167] E. Martioli, D. Teeple & N. Manset. *CFHT data processing and calibration ESPaDOnS pipeline : Upena and OPERA (optical spectropolarimetry). Telescopes from Afar. Eds. : Gajadhar, S. et al.* 2011, 63, 63.

[168] S. Simón-Díaz & A. Herrero. *Fourier method of determining the rotational velocities in OB stars*. A&A 468.3 (2007), 1063-1073.

[169] G. A. Wade. *Evolutionary estimates for 10 magnetic AP stars calculated from their rigid rotator geometries*. A&A 325 (1997), 1063-1069.

[170] L. Fréour et al. *The magnetic field of the chemically peculiar star V352 Peg*. MNRAS 520.3 (2022), 3201-3217.

[171] B. Zhang et al. *The Spectroscopic Binaries from the LAMOST Medium-resolution Survey. I. Searching for Double-lined Spectroscopic Binaries with a Convolutional Neural Network*. ApJS 258.2, 26 (2022), 26.

[172] M. Aurière. *Stellar Polarimetry with NARVAL*. EAS Publications Series 9 (2003).

[173] A. Escorza et al. *HD 41641 : A classical δ Sct-type pulsator with chemical signatures of an Ap star*. A&A 588, A71 (2016), A71.

[174] E. Poretti et al. *Preparing the COROT Space Mission : New Variable Stars in the Galactic Anticenter Direction*. AJ 129.5 (2005).

[175] J. D. Landstreet. *The Orientation of Magnetic Axes in the Magnetic Variables*. ApJ 159 (1970), 1001.

[176] E. Alecian et al. *Characterization of the magnetic field of the Herbig Be star HD200775*. MNRAS 385.1 (2008), 391-403.

[177] O. Kochukhov et al. *The Extraordinary Complex Magnetic Field of the Helium-strong Star HD 37776*. ApJ 726.1, 24 (2011), 24.

[178] H. W. Babcock. *A Catalog of Magnetic Stars*. ApJS 3 (1958), 141.

[179] G. W. Preston & K. Stepien. *The light, magnetic and radial-velocity variations of HD 10783.* ApJ 154 (1968), 971.

[180] G. W. Preston. *The Mean Surface Fields of Magnetic Stars.* ApJ 164 (1971), 309.

[181] N. Cramer & A. Maeder. *Catalogue of photometric data related to surface magnetic fields for B-type stars.* A&AS 41 (1980), 111-115.

[182] M. S. Bessell. *An Investigation of Short-Period Variable Stars. II. The AI Velorum Stars.* ApJS 18 (1969), 195.

[183] Lightkurve Collaboration et al. *Lightkurve : Kepler and TESS time series analysis in Python.* Astrophysics Source Code Library, record ascl :1812.013. 2018.

[184] C. E. Brasseur et al. *Astrocut : Tools for creating cutouts of TESS images.* Astrophysics Source Code Library, record ascl :1905.007. 2019.

[185] Astropy Collaboration et al. *Astropy : A community Python package for astronomy.* A&A 558, A33 (2013), A33.

[186] Astropy Collaboration et al. *The Astropy Project : Building an Open-science Project and Status of the v2.0 Core Package.* AJ 156.3, 123 (2018), 123.

[187] D. H. McNamara. *The High-Amplitude δ Scuti Stars. Delta Scuti and Related Stars.* Sous la dir. de M. Breger & M. Montgomery. T. 210. Astronomical Society of the Pacific Conference Series. 2000, 373.

[188] E. Paunzen et al. *TYC 3637-1152-1 - A high amplitude δ Scuti star with peculiar pulsational properties.* New Astron. 68 (2019), 39-44.

[189] A. Claret, E. Rodriguez & J. M. Garcia. *Comparison between standard evolution models for high amplitude δ Sct stars.* Rev. Mex. Astron. Astrofis. 21 (1990), 389.

[190] A. Arellano Ferro, N. S. Nunez & J. J. Avila. *On the Period Variation of the Delta Scuti Star VZ CANCRI.* PASP 106 (1994), 696.

[191] C. Boonyarak et al. *On the period variations of several low declination high amplitude delta Scuti variables.* Ap&SS 333.1 (2011), 125-131.

[192] J.-F. Donati et al. *A dedicated polarimeter for the MuSiCoS échelle spectrograph.* A&AS 134 (1999), 149-159.

[193] Gaia Collaboration et al. *Gaia Data Release 3. A golden sample of astrophysical parameters.* A&A 674, A39 (2023), A39.

[194] C. A. L. Bailer-Jones et al. *Estimating Distances from Parallaxes. V. Geometric and Photogeometric Distances to 1.47 Billion Stars in Gaia Early Data Release 3.* AJ 161.3, 147 (2021), 147.

[195] S. L. Hidalgo et al. *The Updated BaSTI Stellar Evolution Models and Isochrones. I. Solar-scaled Calculations.* ApJ 856.2, 125 (2018), 125.

[196] S. J. Murphy et al. *Gaia-derived luminosities of Kepler A/F stars and the pulsator fraction across the δ Scuti instability strip.* MNRAS 485.2 (2019), 2380-2400.

[197] P. North et al. *Multiplicity among peculiar A stars. I. The AP stars HD 8441 and HD 137909, and the AM stars HD 43478 and HD 96391.* A&AS 130 (1998), 223-232.

[198] M. Netopil et al. *An investigation of the rotational properties of magnetic chemically peculiar stars.* MNRAS 468.3 (2017), 2745-2756.

[199] K. T. Wraight et al. *A photometric study of chemically peculiar stars with the STEREO satellites - I. Magnetic chemically peculiar stars.* MNRAS 420.1 (2012), 757-772.

[200] L. Casagrande et al. *New constraints on the chemical evolution of the solar neighbourhood and Galactic disc(s). Improved astrophysical parameters for the Geneva-Copenhagen Survey.* A&A 530, A138 (2011), A138.

[201] G. Meynet, P. Eggenberger & A. Maeder. *Massive star models with magnetic braking.* A&A 525, L11 (2011), L11.

[202] R. H. D. Townsend. *Influence of the Coriolis force on the instability of slowly pulsating B stars.* MNRAS 360.2 (2005), 465-476.

[203] N. Piskunov, A. Wehrhahn & T. Marquart. *Optimal extraction of echelle spectra : Getting the most out of observations.* A&A 646, A32 (2021), A32.

RÉSUMÉ

Les variables δ Scuti (δ Sct) sont des étoiles présentant des variations de luminosité entre les modes de pression d'ordre radial faible et les modes mixtes, et ces pulsations durent généralement de quelques minutes à plusieurs heures. Ces étoiles couvrent la gamme spectrale A à F et sont des étoiles de masse intermédiaire, affichant des masses comprises entre 1,5 et 2,5 $M_{\odot}$. En conséquence, elles se situent dans un régime où la structure interne peut varier considérablement entre les étoiles, et par conséquent leur champ magnétique aussi, si elles en ont un. Les étoiles de petite masse (type FGK) ont des champs magnétiques dynamo produits dans leur enveloppe convective et souvent de structure complexe, tandis que les étoiles de grande masse (de type OBA) ont des champs fossiles et stables, issus du nuage moléculaire à partir duquel l'étoile s'est formée, et typiquement dipolaire.
Jusqu'à présent, l'analyse générale du magnétisme des étoiles suggère qu'environ 10% des étoiles de grande masse affichent des champs magnétiques fossiles et cette fréquence augmente pour les champs dynamos des étoiles de plus petites masses. Cependant, à ce jour, seules 3 étoiles δ Sct présentant des signatures de champ magnétique ont été découvertes : HD 188774, HD 67523, et β Cas. De plus, il existe des preuves suggérant que les modes de pulsation à l'intérieur de l'étoile interagissent avec le champ magnétique, ce dernier supprimant et déformant les pulsations.
Au cours de cette thèse, j'ai développé ce domaine dans 2 directions clés. Tout d'abord, j'ai effectué des travaux statistiques sur des candidats magnétiques δ Sct sélectionnés comme cibles idéales à partir d'un sondage plus large d'étoiles Kepler et TESS, affichant des indices spécifiques suggérant l'existence d'un champ magnétique. Ceci m'a permis d'obtenir une meilleure image de la prévalence, de la structure et de l'origine des champs magnétiques pour ce type d'étoiles. Deuxièmement, j'ai effectué une analyse plus approfondie sur quelques étoiles magnétiques δ Sct confirmées, notamment HD 41641. Cette analyse comprend des observations spectropolarimétriques réparties sur toute la rotation de l'étoile, afin de visualiser la structure du champ magnétique à la surface de l'étoile, ainsi que l'analyse des modes de pulsations en anticipation d'études astérosismiques, qui apporteront des nouvelles perspectives sur la structure interne de l'étoile.
Suite à ces travaux, je fournis la liste de 13 étoiles magnétiques δ Sct confirmées à ce jour, multipliant ainsi par 4 l'échantillon connu de ces étoiles et je propose des premiers éléments statistiques de cet échantillon.

MOTS CLÉS

Spectropolarimétrie, Etoiles delta Scuti, Champs magnétiques, Observations

ABSTRACT

δ Scuti (δ Sct) variables are stars exhibiting variations in their luminosity from low radial order pressure modes and mixed modes, and these pulsations typically last anywhere from a few minutes to several hours. These stars span the spectral range A through to F and are typically intermediate mass stars, displaying masses between 1.5-2.5 $M_{\odot}$. Due to the latter, they fall in a regime where the internal structure can vary significantly between stars, and as a result so too can their magnetic field, should they have one. Typically, small mass stars (FGK) have dynamo magnetic fields produced in their convective envelope and often complex in structure, whereas large mass stars (OBA) have fossil fields, i.e. remnants from the molecular cloud from which the star formed, and typically dipolar.
So far, general analysis in the magnetism of hot (OBA) stars suggests that about 10% of intermediate mass (non-variable) stars display magnetic fields, and the field occurrence increases for dynamo fields in lower mass stars. However, at the start of this thesis work, only 3 δ Sct stars had been found to exhibit magnetic field signatures: HD 188774, HD 67523, and β Cas. Additionally, there is evidence to suggest that the pulsation modes within the star interact with the magnetic field, with the latter suppressing and potentially warping the former.
Over the course of this PhD, I expanded on this domain in two key areas. First, I performed a statistical study of magnetic δ Sct candidates, selected as ideal targets from wider surveys of Kepler and TESS targets, displaying specific features that hint at the existence of a magnetic field. This allows us to get a better picture of the occurrence, structure and origin of magnetic fields for this type of star. Second, I performed more in-depth analysis on a couple of established magnetic δ Sct stars, in particular HD 41641. This analysis includes spectropolarimetric observations spread over the full rotation of the star, in order to map the magnetic field structure at the surface, and pulsational analysis to prepare for future asteroseismic modelling, which will provide insight into the internal structure of the star.
Thanks to this work, I can list 13 magnetic δ Sct stars confirmed to date, which increases the sample of such stars by a factor 4, and I suggest first statistical properties of this sample.

KEYWORDS

Spectropolarimetry, delta Scuti stars, Magnetic fields, Observations